3-8-2004

Optical Characterization and Modeling of Compositionally Matched Indium Arsenide-Antimonide Bulk and Multiple Quantum Well Semiconductors

Scott C. Phillips

OPTICAL CHARACTERIZATION AND MODELING OF COMPOSITIONALLY MATCHED INDIUM ARSENIDE-ANTIMONIDE BULK AND MULTIPLE QUANTUM WELL SEMICONDUCTORS

THESIS

Scott C. Phillips

AFIT/GAP/ENP/04-05

DEPARTMENT OF THE AIR FORCE
AIR UNIVERSITY

AIR FORCE INSTITUTE OF TECHNOLOGY

Wright-Patterson Air Force Base, Ohio

AFIT/GAP/ENP/04-05

OPTICAL CHARACTERIZATION AND MODELING OF COMPOSITIONALLY MATCHED INDIUM ARSENIDE-ANTIMONIDE BULK AND MULTIPLE QUANTUM WELL SEMICONDUCTORS

THESIS

Presented to the Faculty

Department of Engineering Physics

Graduate School of Engineering and Management

Air Force Institute of Technology

Air University

Air Education and Training Command

In Partial Fulfillment of the Requirements for the

Degree of Master of Science (Applied Physics)

Scott C. Phillips, BS

March 2004

AFIT/GAP/ENP/04-05

OPTICAL CHARACTERIZATION AND MODELING OF COMPOSITIONALLY MATCHED INDIUM ARSENIDE-ANTIMONIDE BULK AND MULTIPLE QUANTUM WELL SEMICONDUCTORS

Scott C. Phillips, BS

Approved:

Robert L. Hengehold (Chairman) — 8 Mar '04 date

Michael A. Marciniak (Member) — 8 Mar 04 date

David E. Weeks (Member) — 8 Mar 04 date

Abstract

Indium arsenide-antimonide ($InAs_{1-x}Sb_x$) semiconductors have been determined to emit in the 3-5μm range, the window of interest for countermeasures against infrared electro-optical threats. This experiment set out to cross the bulk to quantum well characterization barrier by optically characterizing two sets of compositionally matched type I quantum well and bulk well material samples. Absorption measurements determined the bandgap energy of the bulk samples and the first allowed subband transition for the quantum wells. By collecting absorption spectra at different temperatures, the trend of the energy transitions was described by fitting a Varshni equation to them. The expected result of the quantum well always having slightly higher energy than its bulk counterpart was observed. An etalon effect was also observed in the quantum wells, caused by the cladding layers in those samples. Photoluminescence spectra were also collected to characterize the change in electron temperature (T_e) as the excitation power was varied. As expected, T_e increased with increasing power and increasing temperature. The start of the longitudinal optical phonon dominated cooling range due to excitation intensity was also determined for the samples from $1/T_e$. It was found that the quantum well required higher excitations intensities to achieve this effect. Lastly, the energy transitions found for the quantum well samples were compared to those found by a finite element method (femb) model. The predicted energies all laid a constant value above what was found experimentally, indicating the program had a translation error within it.

Acknowledgements

I would like to take this opportunity to thank everyone who has made the completion of this paper possible. First off, I would like to express gratitude to the faculty of the Engineering Physics department at AFIT whom helped me to get a first rate education. More specifically, I would like to thank my advisor, Dr. Hengehold, for his support and expertise on matters of all the research I performed. His suggestions and guidance throughout the process were proven to be invaluable. I would also like to express my appreciation to the other members of my thesis committee: Dr. Marciniak was always able to fill in the cracks of knowledge needed to understand the experimental processes while Dr. Weeks provided the necessary background to complete the theoretical aspects of the project. Besides the committee, I would like to thank technicians Greg Smith and Mike Ranft for keeping all the projects I worked on operational. My gratitude also extends to Dr. Guangming Li for helping me get all of the research started, allowing me to start off running instead of dragging my feet.

Last, but not least, I would like to thank my significant other, whom I had the pleasure of being my girlfriend, fiancé, and wife during my time at AFIT. Without her love and support, I don't think I would have finished as sanely as I did. For that, I dedicate this to her.

Scott C. Phillips

Table of Contents

Page

Abstract iv

Acknowledgements v

List of Figures viii

List of Tables xii

List of Abbreviations and Constants xiii

1. Introduction 1

1.1 Motivation 1
1.2 Problem Statement 2
1.3 Organization of Thesis 3

2. Background and Theory 5

2.1 Semiconductor Basics 5
2.2 Carrier Concentrations 11
2.3 Impurities and the Fermi Level 15
2.4 Optical Processes In Semiconductors 19
2.5 Absorption Measurements 24
2.6 Photoluminescence Measurements 27
2.7 Quantum Well Structures 30

3. Experiment 36

3.1 Samples Studied 36
3.2 Absorption Configuration 37
3.3 Absorption Technique 39
3.4 Photoluminescence Configuration 40
3.5 Photoluminescence Technique 42
3.6 Quantum Well Modeling 44

4. Data and Results 46

4.1 Calibration 46
4.2 Absorption 48
4.3 Photoluminescence 65
4.4 Quantum Well Modeling 77

Page

5. Conclusions and Recommendations 84

Appendix A: Absorption Measurements of Two Additional Quantum Wells 90

Appendix B: Quantum Well Input File for FEMB Code 93

Appendix C: Material Parameters Input File for FEMB Code 99

Bibliography 103

Vita 105

List of Figures

Figure Page

1- 1: The atmospheric transmission and the III-V semiconductors that emit correspondingly. (12: 1-3) 2

2- 1: When atoms are brought together, the atomic levels of the electrons interact and intersect creating bands of energy. (13:377) 6

2- 2: Energy band diagrams for: a conductor with a partially filled band, a conductor with overlapping bands, an insulator, and a semiconductor at a finite temperature. (9:174) 7

2- 3: Photon absorption process in a direct and an indirect semiconductor as shown in momentum space. 10

2- 4: The Fermi-Dirac distribution for temperatures of approximately 0K, 300K, and 1000K. 11

2- 5: The density of states function shown for the conduction and valence band. 13

2- 6: The distribution function calculated from the Fermi-Dirac distribution multiplied by the density of states function shown for an intrinsic and extrinsic semiconductor. (13:387) 14

2- 7: A two-dimensional lattice structure of a silicon (IV) semiconductor and how adding elements of different groups (III and V) affect it. (13: 382) 16

2- 8: Dopants and their ionization energies in gallium arsenide. (3:54) 19

2- 9: The two phonon types that occur in a lattice: acoustic and optical. 21

2- 10: Absorption in a simple indirect semiconductor from its valence band maximum to conduction band minimum through the accompiniment of a phonon....22

2- 11: A diagram depicting several different emission transitions in a semiconductor: band-to-band, exciton, bound exciton, donor-to band, band-to-acceptor, and donor-to-acceptor. 23

2- 12: A more accurate depiction of the bandstructure for gallium arsenide at room temperature (300K). (3:64)....24

Figure Page

2- 13: A schematic depicting some possible absorption transitions for a semiconductor (3:150). 26

2- 14: An example of what a typical photoluminescence emission spectrum of a semiconductor looks like. 28

2- 15: The photoluminescence limiting factors from the band-to-band emission is depicted. 30

2- 16: A schematic of a quantum well structure. 31

2- 17: The quantized energy subbands found in a quantum well structure. 32

2- 18: The energy subbands and their corresponding two-dimensional density of states formed in the z-direction of the quantum well. (3:82) 33

2- 19: The two types of quantum well structures. 34

3- 1: Diagrams depicting how the quantum well samples used for experimentation were layered. 37

3- 2: The absorption configuration used for this experiment to get the bandgap energies of the antimony-based samples. 38

3- 3: The table configuration used for this experiment to obtain the photoluminescence from the antimony-based semiconductors. 41

4- 1: The setup used to calibrate the spectrometer to the correct wavelengths. 46

4- 2: The experimental transmission of the W03540-6 OCLI filter. 47

4- 3: The ceramic IR source response output by the detector with nothing obstructing the path (background) and with bulk sample 93-045 in the path. 49

4- 4: The absorption spectra of bulk sample 93-045 ($InAs_{0.911}Sb_{0.089}$) taken by the Bio-Rad system at various temperatures. 51

4- 5: The free carrier absorption fit to bulk sample 93-045 ($InAs_{0.911}Sb_{0.089}$) at various temperatures. 53

Figure Page

4- 6: The bandedge fit to bulk sample 93-045 ($InAs_{0.911}Sb_{0.089}$) at various temperatures. 54

4- 7: The quantum well 94-034 sample compared to a gallium antimonide sample labeled sample #5. 55

4- 8: The absorption curves observed for quantum well sample 94-099 ($InAs_{0.9117}Sb_{0.0883}/In_{0.88}Al_{0.12}As_{0.878}Sb_{0.122}$) at several temperatures. 57

4- 9: A depiction of a Fabry-Perot etalon, and how a quantum well would relate. 57

4- 10: The expected results of the self referencing method for a bulk semiconductor as well as a quantum well using their respective density of states functions. 58

4- 11: The absorption curves of bulk 93-045 using its 50K data for self referencing. 59

4- 12: The absorption curves of quantum well 94-099 using its 50K data for self referencing. 60

4- 13: The results of the absorption experiment fit to a Varshni equation. 63

4- 14: The photoluminescence of all three samples used in the experiment at 5K and using various excitation powers. 66

4- 15: The photoluminescence of quantum well sample 94-034 at 5K. 68

4- 16: A comparison of the absorption and photoluminescence spectra for bulk sample 93-045. 69

4- 17: The electron temperature fit for bulk sample 93-045 for various excitation powers at 25K. 70

4- 18: A diagram depicting how electron temperature is defined. 71

4- 19: The inverse electron temperature given for GaAs at 2K in terms of pump intensity (log scale) and how it relates to the LO phonon energy. (10:137) 74

4- 20: The plots determining the LO phonon cooling domination range for bulk sample 93-045 at various temperature. 76

Figure Page

4- 21: How the energy offsets of the 94-099 quantum well sample are expected to look in real-space at 0K. 80

4- 22: The pictorial equivalence of Table 4-5, drawn to scale.....81

4- 23: A plot showing where the first three predicted energies (starting at the lowest energy: e1-hh1, e1-lh1, and e1-hh3) lie along the self referenced absorption (reference of 50K) and photoluminescence spectra at 5K. 83

A- 1: The two additional quantum wells' results as compared to the 94-099 sample. 91

List of Tables

Table Page

2- 1: The bandstructure energies for a gallium arsenide semiconductor. 18

3- 1: The sample set of the semiconductors used and their compositions. 36

4- 1: The Varshni parameters given to the results of the absorption experiment. 63

4- 2: A comparison of the Varshni parameters found in this experiment to ones previously documented. 64

4- 3: The determined electron temperatures for the three samples given in Kelvin. 72

4- 4: The approximate starting points of the LO phonon cooling range. 77

4- 5: The allowed energy levels found through Ram-Mohan's code for quantum well 94-099. 81

4- 6: The difference between the first allowed transition energy in quantum well sample 94-099 from the absorption experiment and through modeling using the femb code. 81

A- 1: The properties that are known of the two additional quantum wells tested. 90

A- 2: The Varshni parameters found for the two additional quantum wells through the absorption experiment as well as the predicted composition of their well material. 92

List of Abbreviations and Constants

α	absorption coefficient
Å	angstrom = 10^{-10} meters
au	arbitrary units
b	bowing parameter
e	elementary charge = 1.602×10^{-19} Coulumbs
E_0	bandgap energy at absolute zero
E_f	Fermi energy
E_g	band gap energy
eV	electron volt; 1eV = 1.602×10^{-19} joules
F	input light intensity
f(E)	Fermi-Dirac distribution
femb	finite element method program written by Ram-Mohan
g(E)	density of states function
h	Planck's constant = 6.626×10^{-34} joules/second
ħ	Planck's constant = $\frac{h}{2\pi}$
H.E.L.	hot electron luminescence
I	output light intensity
k	momentum vector
K	Kelvin
k_B	Boltzmann's constant = 1.381×10^{-23} joules/Kelvin
LHe	liquid helium

m^*	effective mass
n	number of electrons in an extrinsic semiconductor
n_0	number of electrons in an intrinsic semiconductor
N_a	number of acceptors in a semiconductor
N_d	number of donors in a semiconductor
N(E)	distribution function = f(E)g(E)
n_i	intrinsic carrier concentration = $\sqrt{np}$
p	number of holes in an extrinsic semiconductor
p_0	number of holes in an intrinsic semiconductor
T	temperature
T_e	electron temperature
Ω	phonon

OPTICAL CHARACTERIZATION AND MODELING OF
COMPOSITIONALLY MATCHED INDIUM ARSENIDE-ANTIMONIDE
BULK AND MULTIPLE QUANTUM WELL SEMICONDUCTORS

1. Introduction

1.1 Motivation

Semiconductor laser technology is a fast growing field that has already enveloped many applications. No exception to the rule, the United States Air Force has great interest in incorporating semiconductor lasers into its programs. One program of concern that fits this need is in the deterrence of infrared (IR) missiles and other electro-optical weapons which pose a significant threat on day-to-day operations. Presently using flares sent off the aircraft to confuse the IR-guided weapons, it has been predicted by Bill Taylor of the Air Force Research Laboratory's Electro-Optical Technology Division that this method will become virtually useless against the advancing technology of the heat seeking missiles by 2005 (6:21). Growing advances in IR missile technology require advancement in countermeasures used by aircraft. Due to its small size, efficiency, and reliability, a semiconductor laser is the perfect candidate for this application.

In order for the semiconductor laser to be of use for this application, a laser must be developed which emits in the range of wavelengths that the IR missiles seek. Current IR missile technology exploits the atmospheric transmission window near 3.5μm to seek the jet engines of aircraft which emit radiation primarily on this band. By referencing the atmospheric transmission windows to the bandgaps of the III-V semiconductors that can be created to emit in those ranges (Fig. 1-1), it is determined that antimony (Sb)-based structures meet the necessary demands for an effective countermeasure.

With the correct material determined, the performance of these mid-infrared (MIR) semiconductor lasers (and detectors) has to be optimized. This is done by determining which design and fabrication process enhances the performance of these devices. This requires an accurate knowledge of the quantum well dispersion relations of the material, which is not readily available.

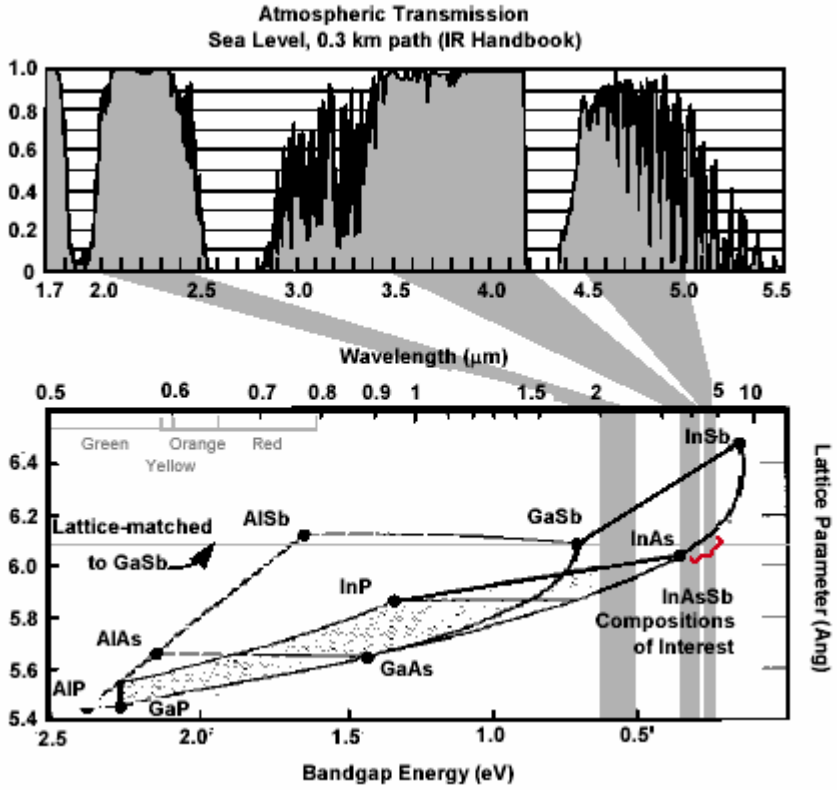

Fig. 1- 1: Following the gray shading down from the atmospheric transmission, the III-V semiconductor that emits correspondingly is found. Since IR missiles exploit the 3.5-4.2mm and 4.5-5.0mm range, it is determined that antimony (Sb)-based semiconductor lasers are desired. (12: 1-3)

1.2 Problem Statement

In order to gain a greater understanding of the antimony-based structures, the current experiment was designed to characterize two indium-arsenide-antimonide

(InAsSb), type-I multiple-quantum-wells. For comparison, two bulk samples that are compositionally matched to the wells are also characterized. Using an absorption study of the samples, bandgap energies (E_g) and how they are affected by temperature (T) are documented. A photoluminescence study is also performed on each sample to support the bandgap energy findings of the absorption spectra, as well as provide electron temperature (T_e) information. Extracting this information from the data gives an understanding of what emission energies various material compositions produce upon external excitation (for both bulk and quantum well) and how these energies vary depending on the device environment. The electron temperatures calculated for these emissions provide insight into how high in the conduction band electrons are sitting given a constant external excitation. This will become useful for finding the range at which the longitudinal optical phonon is the dominant cooling process for the particular material composition. In order to further characterize the quantum well samples, the energy subbands of the well are predicted using the 8-band k·P model implemented into Ram-Mohan's Finite Element Method computer code (femb). These theoretical predictions are then compared to the experimental values to determine the effectiveness of the modeling and its parameters.

1.3 Organization of Thesis

This thesis is organized into five chapters. Following this introduction to the experiment, a background overview of semiconductors and their properties is given; including an overview on absorption and photoluminescence process as well as the nature of quantum well structures. The third chapter describes the samples used in this research,

as well as the experimental approach used to carry out the study. This is followed by a discussion of the experimental results obtained and the thesis ends with suggestions for future work.

2. Background and Theory

This chapter reviews the theory connected with semiconductors and their processes. Beginning with a basic overview of what a semiconductor is and some basic properties, the determination of the concentrations of the carriers that define the semiconductor and a look at how impurities impact the structure are explained. Some optical processes that occur in semiconductors are then addressed followed by an overview of absorption and photoluminescence measurements. To conclude, quantum well structures are discussed.

2.1 Semiconductor Basics

Individual atoms have electrons that occupy bound orbits with discrete atomic levels of energy. When atoms are brought together and start to interact, the individual atom's electron orbits begin to intersect with the introduced atomic orbits, creating a range of allowable energies that the electrons can occupy. This range of energies is referred to as a band. The distribution of the band is related to the inter-atomic spacing of the lattice, as demonstrated by Fig. 2-1. As the electron orbits interact with one another, it is observed that there are ranges of energies that the bands do not occupy; these are called energy band gaps. It is the nature of these forbidden energy gaps that characterize the atomic crystal's ability to allow electrons to flow through the material, referred to as conductivity.

There are three possible classifications describing the conductivity of a substance: conductor, insulator, or semiconductor. To be classified as a conductor, the material has to have a partially filled energy band at absolute zero or have overlapping upper bands.

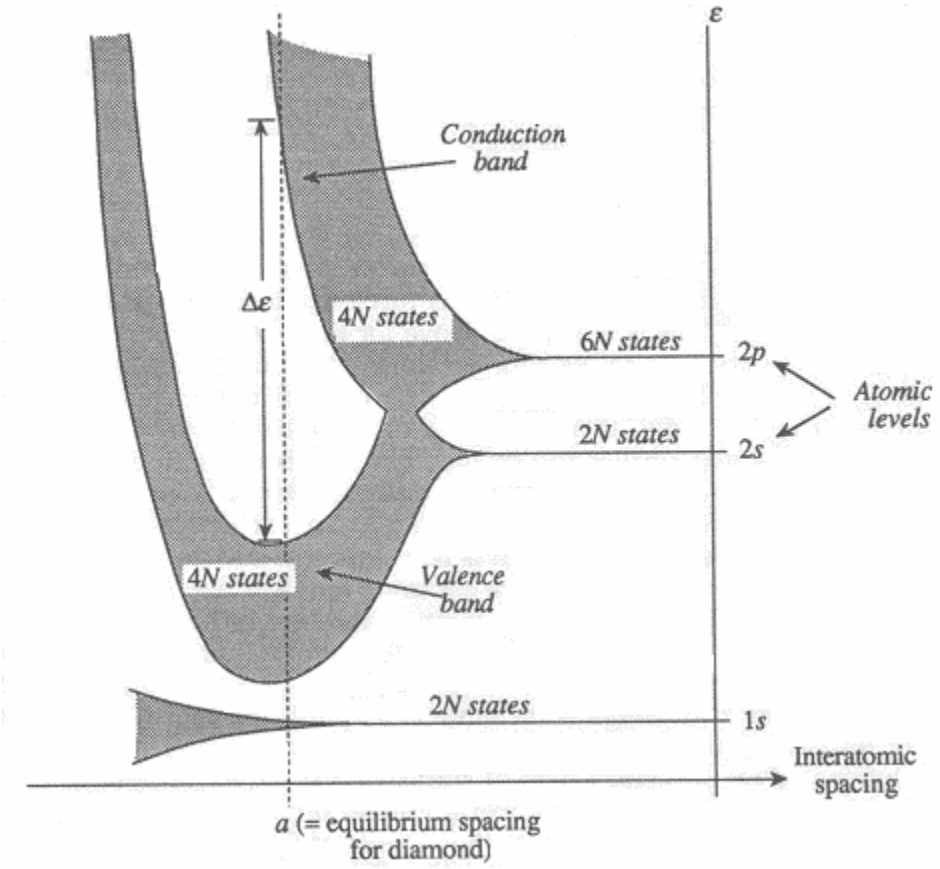

Fig. 2- 1: When atoms are brought together, the atomic levels of the electrons interact and intersect. This intersection creates a range of energy that is called a band, shown for carbon (diamond). At the inter-atomic equilibrium spacing, (a) three bands with two gaps of forbidden energy can be distinguished. (13:377)

This allows the electrons to easily flow through the material, thereby conducting a current. Opposite to the conductor, insulators allow no current to occur through the crystal. Insulators are found to have their highest energy band, known as the valence band, filled with electrons which is followed by a large energy band gap and a band that is empty of electrons, referred to as the conduction band. Since there are no electrons present in the conduction band and there are no empty states for the electrons to move into in the valence band, insulators have poor conductivity. However, intermediate to

conductors and insulators are materials that are found at absolute zero to have a valence band completely full, followed by a narrow band gap and an empty conduction band. These substances are said to be semiconductors. Intrinsically an insulator, the narrower band gap allows for semiconductors to act like a conductor by promoting the electrons from the valence to the conduction band by adding energy. By exciting the electron to the conduction band, an empty state is created in the valence band which is referred to as a hole. The hole too contributes to the conductivity of the semiconductor by allowing space for the electrons to be mobile. However, since fewer holes are present in the valence band, it is more convenient to think of the conductivity created by them as being caused by positive electron flow.

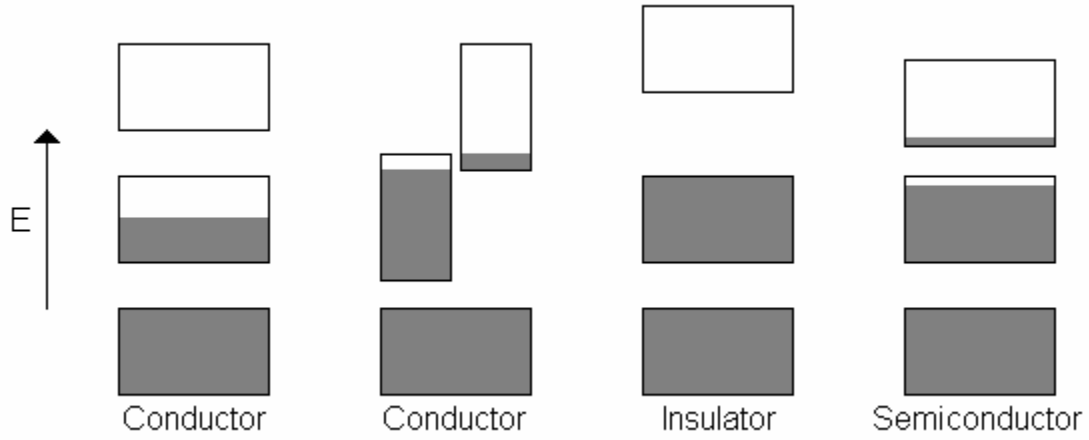

Fig. 2- 2: Energy band diagrams for: a conductor with a partially filled band, a conductor with overlapping bands, an insulator, and a semiconductor at a finite temperature. Shaded regions depict where the electrons lie. Conductors are characterized by a partially full conduction band while insulators and semiconductors have completely empty conduction bands at absolute zero. Above absolute zero, the semiconductor's smaller energy gap allows electrons to be thermally excited into the conduction band. (9:174)

Energy can be added to create a semiconductor in two different ways. First, by introducing photons that possess energy greater than the band gap, E_g, the electrons in the valence band can be excited into the conduction band. The photon energy is given by hν, where h is Planck's constant and ν is the frequency of the incident light. This process is relatively straight forward, but in looking at the semiconductor band structure, momentum of the photon and electron involved must also be accounted for.

The momentum for an electron is given by:

$$p = m_c^* v \qquad [2.1\text{-}1]$$

while its kinetic energy is classically given as:

$$E = \frac{1}{2} m_c^* v^2 \qquad [2.1\text{-}2]$$

where m_c^* is the effective mass of the electron in the material and v is its velocity. In quantum mechanics, the momentum is related to the wave vector k by the equation:

$$p = \hbar k \qquad [2.1\text{-}3]$$

where ħ is a constant equal to h/2π. Combining 2.1-1 and 2.1-3 and substituting into 2.1-2:

$$E = \frac{\hbar^2 k^2}{2m_c^*} \qquad [2.1\text{-}4]$$

i.e., the electron energy is given in terms of the momentum vector k. This can also be written for the hole energies in the valence band by using the hole effective mass, m_v^*. Using this relation, a parabolic approximation to the band structure of a semiconductor can be created in energy-momentum space.

With an understanding of how the material's bandstructure is achieved, a distinction between the two classifications of semiconductors can be made. A direct band

gap material is classified as having the conduction band minimum and valence band maximum found at the same k-value. Gallium arsenide is a common example of this class. Silicon's band structure minimum and maximum, on the other hand, do not lie at the same k-position. This type of semiconductor is classified as indirect.

Regardless of the class of semiconductor, the process of excitation through photons remains the same. To conserve momentum, the masses of the participants involved are observed. Since photons have negligible mass, their momentum is nearly zero. This means that the electron should maintain its momentum during this process (shown with a vertical transition in Fig. 2-3). It is also possible for the photon to transfer some of its momentum into a lattice vibration known as a phonon causing the transition to not be a direct vertical transition. This process will be discussed later in Section 2-4.

Another process by which electrons can be promoted into the conduction band in semiconductors is by raising the temperature of the crystal. At temperatures above absolute zero, kinetic energy is gained by the electrons, which allows for them to be excited to the conduction band. Whether or not an electron is excited thermally is determined through the probability given by the Fermi-Dirac distribution:

$$f_c(E) = \frac{1}{1 + e^{(E-E_F)/k_BT}} \qquad [2.1\text{-}5]$$

where T is the temperature, k_B is Boltzmann's constant, E is the energy whose occupation is of interest, and E_F represents the energy where the probability of finding an electron is ½, known as the Fermi level (3:76). Likewise, the distribution of holes can be described by $1\text{-}f_c(E)$ since each hole was created by the excitation of the electron:

$$f_v(E) = \frac{1}{1 + e^{-(E-E_F)/k_BT}}. \qquad [2.1\text{-}6]$$

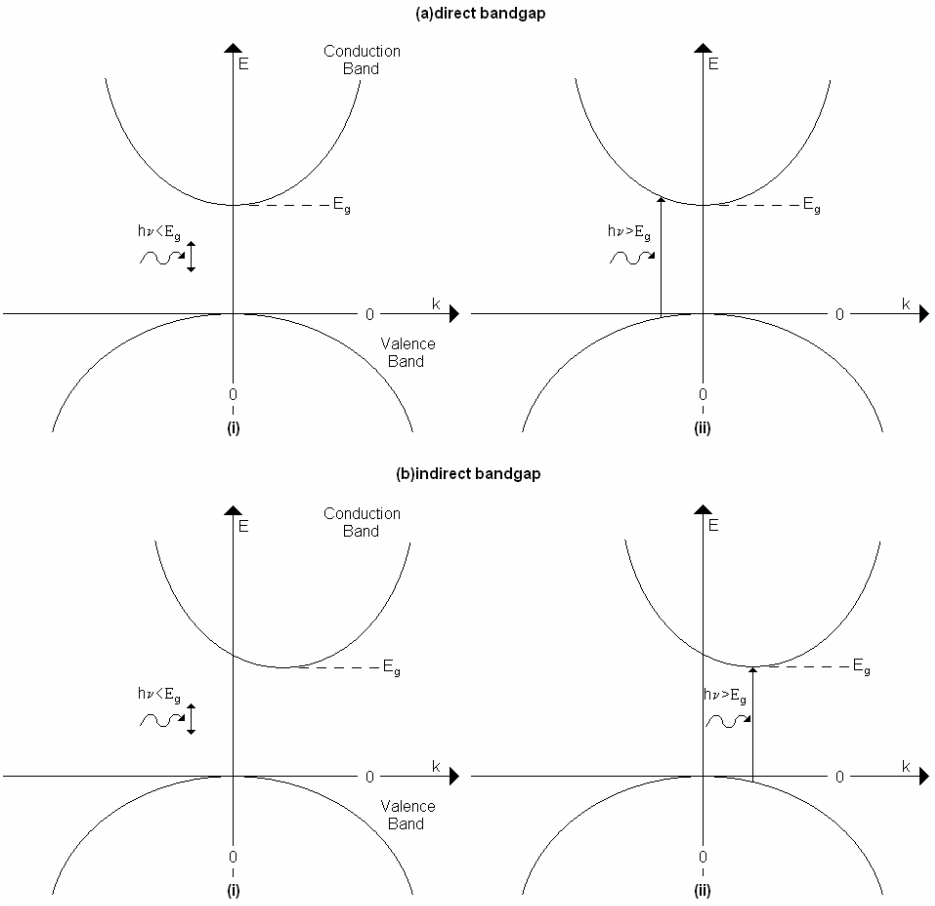

Fig. 2- 3: Photon absorption process in (a) a direct and (b) an indirect semiconductor as shown in momentum space. (i) A photon of energy less than that of the energy gap does not get absorbed, making the material transparent to that wavelength. With an energy greater than the band gap (ii), the photon gets absorbed if an available electron lies in the valence band with a hole directly above in the conduction band.

For the most simplistic model, the Fermi level is found in the middle of the energy gap, as seen in Fig. 2-4. With the Fermi-Dirac distribution, it can be seen that only when the temperature is absolute zero is there no probability of an electron being in the conduction band.

Another process in which the electrons can participate in a semiconductor is emission. In this process, the electron transitions back from the conduction band to the

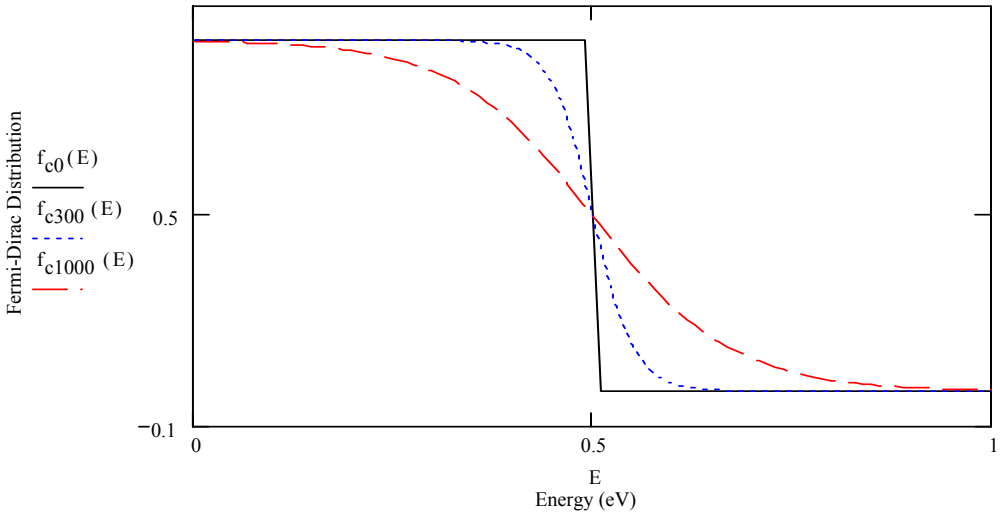

Fig. 2- 4: The Fermi-Dirac distribution for temperatures of approximately 0K (solid line), 300K (dotted line), and 1000K (dashed line). The distribution goes from a step function at absolute zero into a gradually smoother function the higher the temperature gets. This coincides with the number of electrons that can be found in the conduction band; zero for absolute zero and gradually more as temperature increases. For this graph, the Fermi level is found at 0.5eV, which is where all of the graphs cross with a probability of 0.5.

valence band. Any electron along the k-axis can be emitted so long as a hole lies directly beneath it. Through the emission process, a photon with equivalent energy as that from the conduction to valence band transition is given off in order to conserve energy. However, although it is possible for an emission to occur at anywhere along the k-axis, it will be shown that it is less probable for electrons further away from the zone center (k=0) due to the concentrations of electrons and holes found there.

2.2 Carrier Concentrations

Promoting electrons into the conduction band of a semiconductor thermally and through the absorption of light are what gives the material its conductivity. For photon

absorption, there is no limitation as to where along the momentum axis the electron leaves the valence band to be excited into the conduction band as long as momentum and energy is conserved. Since the conduction band is only partially filled, there is almost always a hole for the electron to fill. However, in the opposite process, the valence band is mostly filled with electrons and the excited electron cannot fall to the lower band unless there is a hole directly beneath it. The carrier concentration of both the electrons and holes in the semiconductor becomes very important for the spontaneous emission process.

The first step in finding the carrier concentrations is to determine which energy levels are occupied with electrons and holes. At a thermal equilibrium of temperature T, this is given by the Fermi-Dirac distribution (equation 2.1-1 for electrons and 2.1-2 for holes). Since these distributions also include energies that are found within the forbidden energy gap, another function is needed to describe which energies are allowed for the electrons and holes.

The density of allowed states can be obtained by finding the number of available states in the energy range between E and E+dE. One finds that the number of allowed states in the interval E and E+dE is (3:79):

$$N(E)dE = \frac{4\pi}{h^3}(2m_C^*)^{3/2}E^{1/2}. \qquad [2.2\text{-}1]$$

If the energies are referred to the edge of the energy band corresponding to the carrier in question (conduction band for electron and valence band for hole), the equation can be rewritten into:

$$g_c(E) = \frac{4\pi}{h^3}(2m_C^*)^{3/2}(E - E_C)^{1/2} \qquad [2.2\text{-}2]$$

$$g_v(E) = \frac{4\pi}{h^3}(2m_v^*)^{3/2}(E_v - E)^{1/2} \qquad [2.2\text{-}3]$$

where the sub characters c and v represent conduction and valence bands (electron and hole), respectively. These functions are plotted in Fig. 2-5.

Since the equations for the number of allowed states are not defined for energies that lie within the band gap, the density of states is set to zero. This means there are no allowable energy states within the energy band gap. Now, combining the electron equation of allowed states with its respectable Fermi-Dirac distribution, the distribution of the electrons can be determined by:

$$N_c(E) = f_c(E) \cdot g_c(E) = \frac{4\pi}{h^3}(2m_c^*)^{3/2}(E - E_c)^{1/2}(1 + e^{(E-E_F)/k_BT})^{-1} \quad [2.2\text{-}4]$$

$$N_v(E) = f_v(E) \cdot g_v(E) = \frac{4\pi}{h^3}(2m_v^*)^{3/2}(E_v - E)^{1/2}(1 + e^{-(E-E_F)/k_BT})^{-1} \quad [2.2\text{-}5]$$

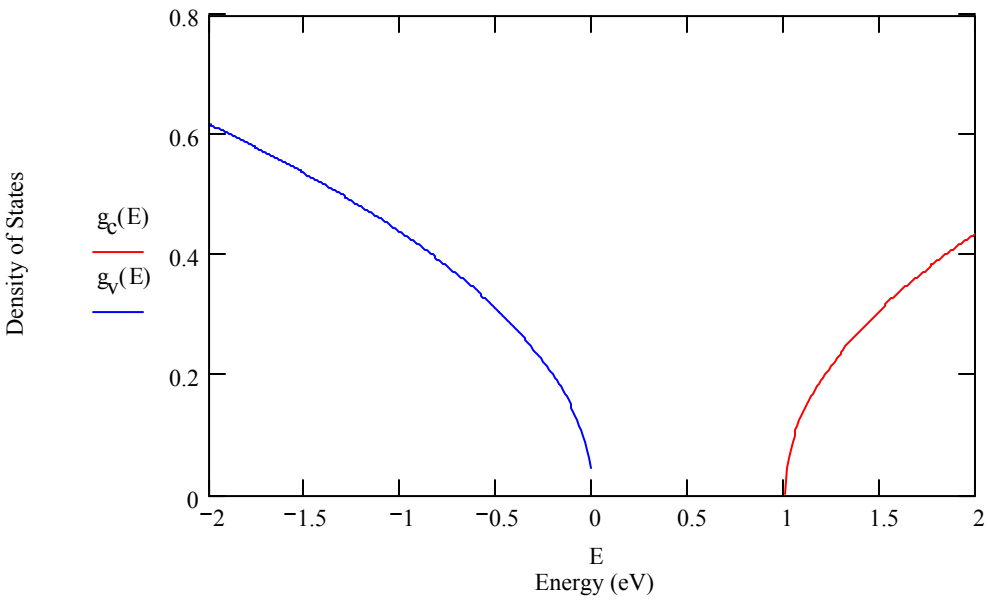

Fig. 2- 5: The density of states function. The conduction band density of states (on the right) describes the number of allowed energies that an electron can occupy. Likewise, the valence band density of states describes the occupation of holes. For this example, the effective masses where set equal (why the bands are equivalent). In actuality, the hole effective mass is usually larger, causing the valence band density of states to be much broader than that of the conduction band.

Both densities of states are diagrammed in Fig. 2-6. As seen on the figures, the concentrations are not found to be highest on the conduction band minimum or valence band maximum. One explanation for this is that with higher equilibrium temperatures, more electrons can be thermally excited and stay excited higher in the conduction band. Another reason for this occurrence is that there are more allowed states for the electron to occupy higher in the conduction band. Since there are more states with higher energy, more electrons should be found beyond the conduction band minima.

Although both encompass the same characteristics, there is a definite difference between the two graphs in Fig. 2-6. Part (a) shows a plot of the carrier concentrations of a semiconductor that contains the same number of electrons as holes. This is the ideal

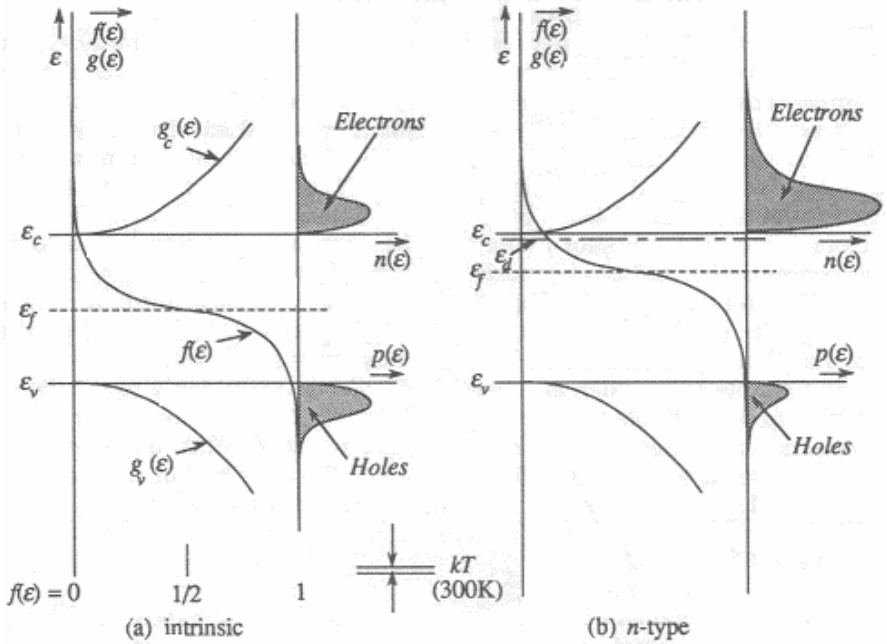

Fig. 2- 6: The distribution function calculated from the Fermi-Dirac distribution multiplied by the density of states function. (a) An intrinsic semiconductor's distribution shows an equal area for both the electrons and holes, symbolizing an equal number of both in the material. An extrinsic semiconductor has an unequal number of carriers (b). (13:387)

case and is referred to an intrinsic semiconductor. Part (b) depicts the carrier concentrations of a semiconductor that have more electrons than holes in it. When this happens, the semiconductor is said to be n-type. This is a result of impurities naturally found or purposefully placed within the crystal. The next section will deal with these impurities and explain how they change some characteristics of the semiconductor.

2.3 Impurities and the Fermi Level

The difference between the carrier concentrations from an intrinsic semiconductor to an impurity semiconductor is caused by the change in the Fermi level within the bandstructure. For the intrinsic semiconductor, the Fermi level is assumed to lie halfway between the conduction and the valence band. However, when an impurity is introduced into the crystal, E_F can be shifted up or down in energy.

Before discussing the shifting of the Fermi level, an understanding of how extra electrons and holes get into the semiconductor should first be understood. Stated in Section 2.1, when electrons are promoted to the conduction band, the empty states that they leave behind in the valence band are holes; this is a one to one correspondence that all intrinsic semiconductors possess. However, introducing an impurity (or dopant if introduced intentionally) allows the electron or hole populations to be varied. When the impurities are present, the substance is referred to as an extrinsic semiconductor. Substituting an atom with one more valence electron than the original semiconductor substance found in the crystal, for example a group V atom into a group IV semiconductor or a group VI atom into the group V atom of a III-V semiconductor, creates an extra electron that is not covalently bound and a positive ion in the lattice.

This is shown in Fig. 2-7, where phosphorus (group V) is introduced into a group IV semiconductor (silicon). This process is called n-doping since extra negative charge carriers (electrons) are being added to the system. The atoms that are added to create the n-type semiconductor are called donor atoms since they are donating an electron to the crystal. In contrast, an atom with one less valence electron is referred to as an acceptor. By adding group III (boron) atoms to a silicon semiconductor, a negative ion in the lattice is created with one less covalent bond. These added atoms create a vacancy in the crystal where an electron can be accepted and allow for more positive charge carriers (holes). This type of doped semiconductor is referred to as p-type.

Knowing the difference between the two types of doping, their effect on the Fermi level can now be discussed. First, the E_F can be numerically determined for an intrinsic semiconductor. To do this, the total number of thermally excited electrons and holes in

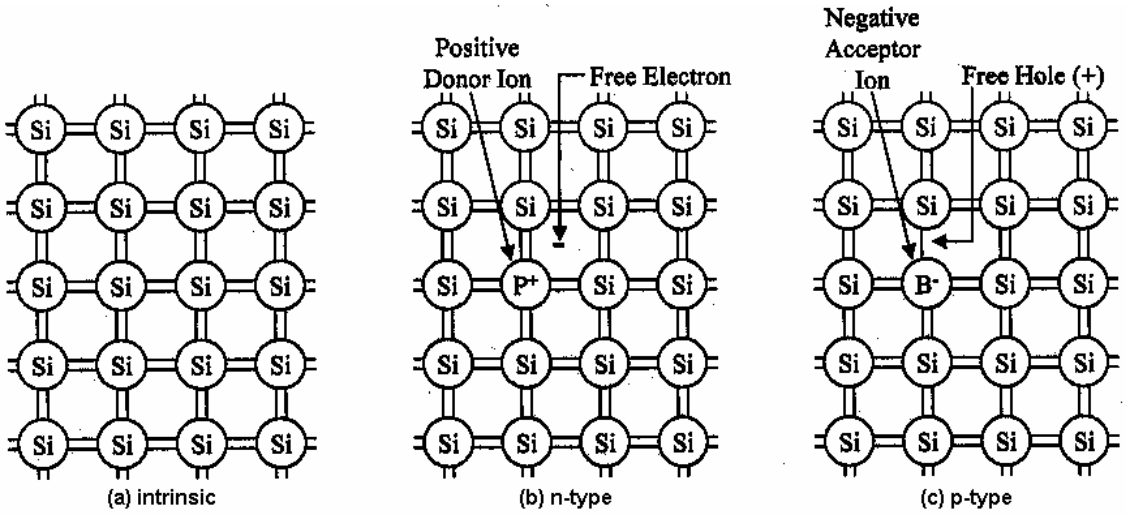

Fig. 2- 7: (a) A two-dimensional lattice structure of a silicon (IV) semiconductor. By adding an atom from group V, phosphorous, an extra electron that is not covalently bonded is introduced into the material (b). This is referred to as an n-type semiconductor. A p-type semiconductor (c) is created by adding atoms of boron, group III, which allows for an extra free hole. (13: 382)

the conduction and valence bands, respectively, are found. This is done by integrating $N_c(E)$ and $N_v(E)$ from 2.2-4 and 2.2-5, giving:

$$n_0 = 2\left(\frac{2\pi m_c^* k_B T}{h^2}\right)^{3/2} e^{-(E_c - E_F)/kT} \qquad [2.3\text{-}1]$$

$$p_0 = 2\left(\frac{2\pi m_v^* k_B T}{h^2}\right)^{3/2} e^{-(E_F - E_v)/kT} \qquad [2.3\text{-}2]$$

where n_0 and p_0 represent the number of negative and positive carriers in the material. Since the number of oppositely charged carriers is equal for an intrinsic semiconductor, E_F can be determined by equating these two equations:

$$E_{Fi} = \frac{E_g}{2} + \frac{3}{4} k_B T \ln\left(\frac{m_v^*}{m_c^*}\right) \qquad [2.3\text{-}3]$$

where $E_g = (E_c - E_v)$ and represents the gap energy between the bands. This equation shows that for an intrinsic semiconductor, the first term will give a Fermi energy halfway between the conduction and valence bands, provided the second term is insignificant in value. For this to occur, the effective mass of the holes and electrons would need to be relatively equivalent.

For an extrinsic semiconductor, the number of electrons does not equal the number of holes. As was seen earlier through Fig. 2-7, the lattice may have more electrons and/or holes than the intrinsic case, but the crystal still stays electrically neutral through the positive and negative impurity ions. This can be written as:

$$e(p_0 - n_0) + e(N_d - N_a) = 0 \qquad [2.3\text{-}4]$$

where N_d is the number of donor ions and N_a is the number of acceptor ions. Using this, and through some substitution and mathematical solving, the resulting Fermi energy for

any semiconductor substance in thermal equilibrium is:

$$E_F = E_{Fi} + k_B T \sinh^{-1}\left(\frac{N_d - N_a}{2n_i}\right) \qquad [2.3\text{-}5]$$

where n_i is the intrinsic carrier concentration of the material defined by $\sqrt{np}$ where n is the total number of electrons in the conduction band and p is the total number of holes in the valence band (13:391). As is seen, by varying the number of impurities in the semiconductor, the Fermi level can be shifted from the center of the energy gap. To see this phenomenon more clearly, Table 2-1 presents the case where $N_a = 5x10^{15}$ cm^{-3} carbon atoms are substituted for arsenic atoms in the III-V type gallium arsenide semiconductor.

Table 2- 1: The bandstructure energies for a gallium arsenide semiconductor.

Description	Energy (eV)
Direct Bandgap, E_g	1.424
Midgap Fermi Level Approximation	0.712
Intrinsic Fermi Level	0.751
Extrinsic Fermi Level	0.191

The intrinsic Fermi level shows the effect effective masses have on a material, where $m_v^*=0.51m_0$ and $m_c^*=0.067m_0$. By adding $5x10^{15}$ cm^{-3} carbon atoms as acceptors into the lattice, the shift in the Fermi level is calculated. All are calculated at room temperature (300K) and are measured from the top of the valence band.

Along with causing a shift in carrier concentrations within a semiconductor by changing its Fermi level, impurities also create allowed energies within the band gap that carriers can occupy. Since the impurity in n-type semiconductors provides extra electrons to be promoted into the conduction band, the most ideal place from which to measure the donor energy band is its energetic distance below the conduction band

minimum. Likewise, acceptor atoms in p-type material provide holes for electrons to be thermally promoted to from the valence band; so, acceptor energy levels are measured by their distance above the valence band maximum. To determine the exact energy above or below the bands the dopant levels fall, the ionization energy of the impurity within the semiconductor material is used (3:52). Fig. 2-8 depicts an example of different dopants and their energy levels found in gallium arsenide. To find out how to depict the donor and acceptor levels in momentum (k-) space, the fact that the locations of the impurity ions can be predicted is used. From the Heisenburg uncertainty principle, both the position and the momentum of a subatomic particle cannot be simultaneously known, thus the momentum of the impurity is not known. This is depicted in the E-k diagram as a straight line at a given energy that extends infinitely into k-space.

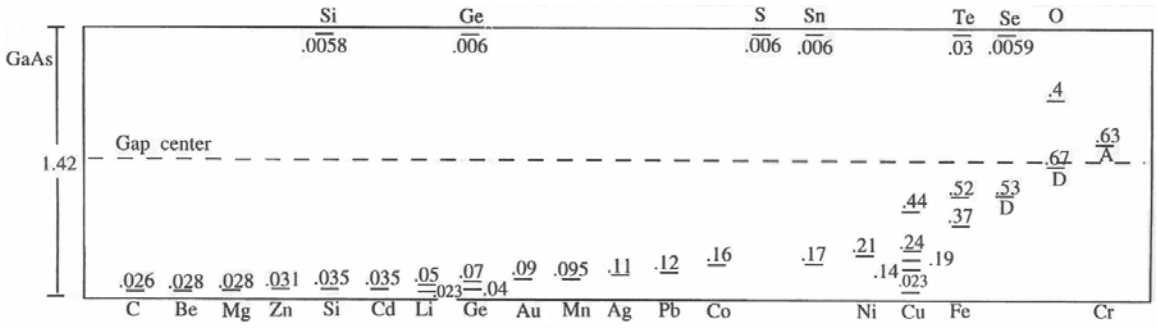

Fig. 2- 8: Dopants and their ionization energies in gallium arsenide given in electron volts. The impurities found in the upper half of the chart serve as donors and their energy is calculated from the conduction band. Calculated from the valence band, the lower levels show the energies of different acceptors. (3:54)

2.4 Optical Processes In Semiconductors

With the addition of energy bands from impurities, it becomes evident that there must be more transitions in a semiconductor than those previously described that an

electron can undergo after absorbing a photon. Energy levels inside the energy gap resulting from the addition of impurities allow carriers to occupy energies that were once forbidden. This in-turn allows for transitions to and from the impurity levels.

For an extrinsic semiconductor, impurity transitions are exactly equivalent to band-band transitions. However, in order for the impurity transitions to occur, the impurity levels must be partly de-ionized. In other words, all the electrons in the donor level must not be thermally promoted to the conduction band, and all the holes in the acceptor level must not be thermally filled by electrons from the valence band. This can be achieved by keeping the material at a sufficiently low temperature. With this criteria met, an electron can be excited from any energy level to one above it. The same holds true for emission, where an electron can be demoted from any level to one that lies directly below, provided a hole is present.

Although the only movement discussed thus far for electrons is vertical only in k- space, it is possible for an electron to change its momentum as well. Since momentum must be conserved, a gain or loss of momentum in the electron must be created through another source within the semiconductor. One way this can occur is through a phonon, or quantized vibration of the atoms within the lattice structure of the semiconductor. The vibration that passes through the crystal changes the periodic nature of the lattice, which in turn changes the path (and thus the momentum) the electrons are taking. There are two types of phonons found in the atom structure. First, two consecutive atoms and their center of mass can move together. Since this is the same case in acoustic vibrations, this is referred to as an acoustic phonon. The other vibration that travels through the lattice is when the atoms move in such a way that the center of mass remains stationary. This kind

of vibration comes about when the neighboring atoms have opposite charge (such as in a III-V semiconductor) and an electric field from an optical wave strikes the material. For this reason, these are referred to as optical phonons (3:552). Both vibrations have their own distinct quantized energy for a given semiconductor (optical phonons possess higher energy than acoustic) and are shown in Fig. 2-9. Through the help of phonons in the lattice, electrons and holes can be transported along the k-axis of the bandstructure. Also, when a phonon coincides with an incoming photon, it is possible for the electron to travel an 'indirect' route to the conduction band during excitation. An example of this occurrence is a transition from the valence band maximum to conduction band minimum in an indirect semiconductor shown in Fig. 2-10. As can be seen, phonons play an important role by themselves and in conjunction with other processes.

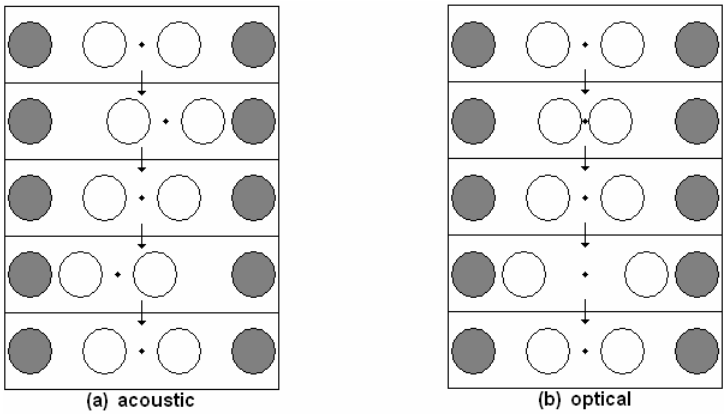

Fig. 2- 9: The two phonon types that occur in a lattice. For this example, the un-shaded circles represent the atoms involved in the vibration while the shaded ones are used for reference. (a) In an acoustic phonon, the atoms vibrate such that the center of mass (dot between the circles) moves with the atoms involved. In an optical phonon (b), the atoms vibrate to make the center of mass remain the same.

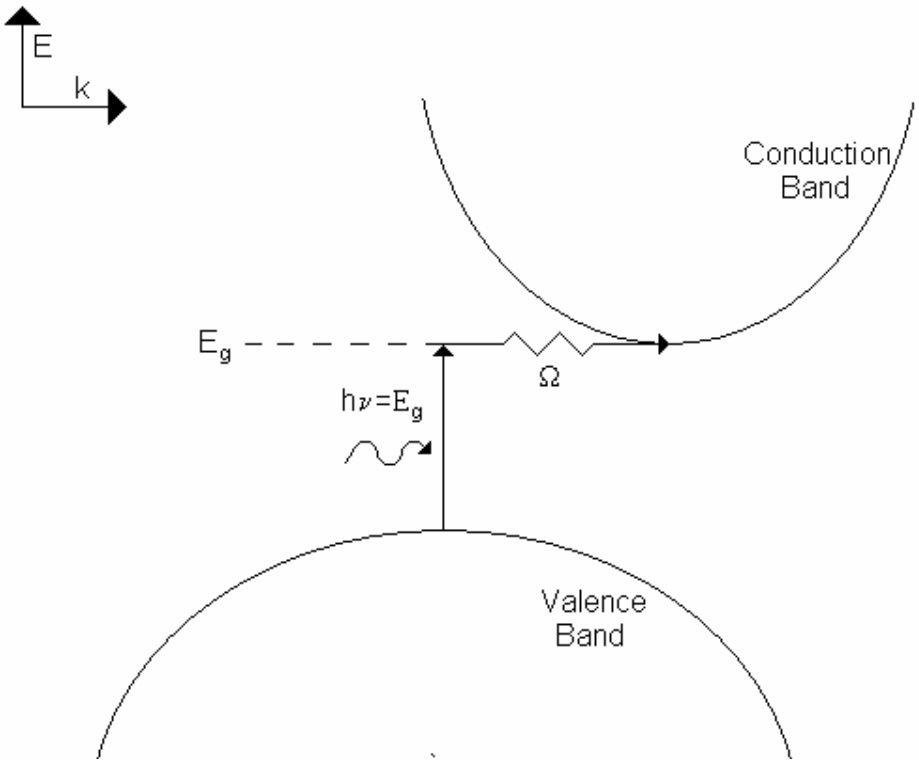

Fig. 2- 10: Absorption in a simple indirect semiconductor from its valence band maximum to conduction band minimum consists of an incoming photon of energy, hν, equal to the energy gap accompanied by a phonon (Ω).

Up until now, every transition discussed has dealt with an electron and hole that have been considered distinct entities. Although this is the case for many excited electron-hole pairs created, it is also possible for the carriers to still hold an attraction to one another due to Coulombic forces after the excitation takes place. When this occurs, the pair is referred to as an exciton (18:317). Without the loss of the attractive forces, some energy is conserved within the pair, and the energy given off by recombination of the exciton is found to be slightly smaller than that of a straight band-to-band transition. A slightly smaller energy than this is also found when the exciton is found to be bound to a neutral donor. When this occurs, it is referred to as a bound exciton. The relative

energies of the excitons with respect to the previous emissions discussed are shown in Fig. 2-11.

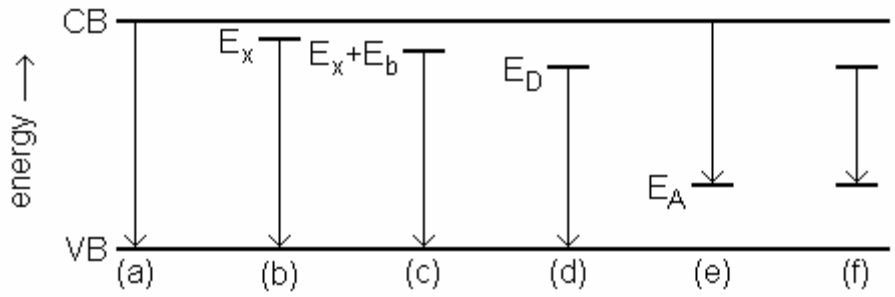

Fig. 2- 11: A diagram depicting several different emission transitions in a semiconductor: (a) band-to-band, (b) exciton, (c) bound exciton, (d) donor-to band, (e) band-to-acceptor, and (f) donor-to-acceptor.

Still, this does not give a complete picture of all the transitions that can occur for a semiconductor. In fact, the bandstructure is much more complex than first introduced. The real E-k diagrams can be experimentally found using a variety of techniques, including the technique of cyclotron resonance (9:212). Through these techniques, it is found that in actual semiconductors, the conduction and valence bands are made up of several different energy levels. The conduction band is a meshing of the different possible orbitals that the electrons can occupy forming a quasi-continuum while the valence bands can be identified as the heavy-hole, light-hole, and split-off band (3:64). Figure 2-12 depicts a two-dimensional version of the various bands for gallium arsenide. Notice that the only degeneracy that occurs in the valence bands near zone center is found at the maximum of the heavy- and light-hole levels. Along with the transitions to and from the extra valence bands, there are now more minima in the conduction band; this makes it harder for the electrons to move about within the level through optical and

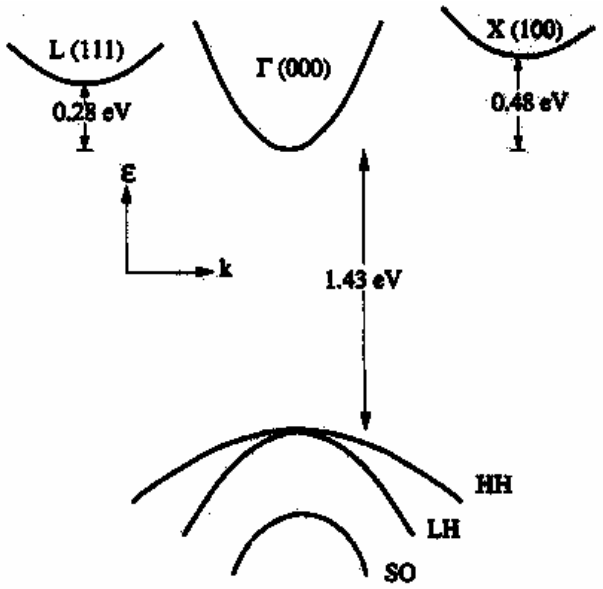

Fig. 2- 12: A more accurate depiction of the bandstructure for gallium arsenide at room temperature (300K). There are three separate bands that create both the total conduction and valence bands. The conduction band is created by three different electron orbitals (Γ, L, and X) that are meshed together for one band of allowable energies. The valence band is created by three bands (heavy-hole, light-hole, and split-off) that are distinguished by the hole effective mass each holds. (3:64)

acoustic phonons alone. This more detailed bandstructure allows for several more complications in how electrons transition through the energy levels, but gives a more complete description of the transitions that can occur in semiconductor materials.

2.5 Absorption Measurements

With a better understanding of the types of transitions that an electron can exhibit within a semiconductor, attention is turned to measuring these properties of the material. Discussed previously, photons of energy hν incident upon a semiconductor either get absorbed by electrons, exciting them higher into energy levels, or if their energy is less

than the bandgap energy, simply pass through the material. By collecting the transmitted light with a detector, the absorption properties of the material can be identified.

The absorption properties of a semiconductor are characterized using a parameter called the absorption coefficient (α). Since the incident light is partially absorbed by the material, α describes the relative decrease of the light's intensity as it passes through the material. This relation is described by

$$\alpha = -\frac{1}{F}\frac{dF}{dx} \qquad [2.5\text{-}1]$$

where F is the incoming light intensity (2:83). Solving the equation for the light intensity expected to be received by a detector through a sample of thickness d is

$$F_d = F_i e^{-\alpha d} \qquad [2.5\text{-}2]$$

where F_i is the incident intensity. As the incident light is varied at different energies, the absorption coefficient also varies with changing energy; α should be zero within the forbidden energy zone of a semiconductor and positive for allowable transitions as seen in Fig. 2-13.

Notice that the absorption that occurs at the bandgap energy rises very steeply in the figure. Understanding that the spectrum is created by filling electrons into higher empty states, the density of states functions (2.2-3, -4) explain the shape of this curve. Looking at the conduction band density of states, the electrons start to be excited into the bottom of the band where only a few states are empty. Since the number of states increases as a function of the square root of the energy, the number of electrons excited into these states likewise increases. The valence band has a similar outcome except that the electrons are being excited out of its states. Due to these properties, the bandgap energy can be obtained from the threshold of the absorption profile.

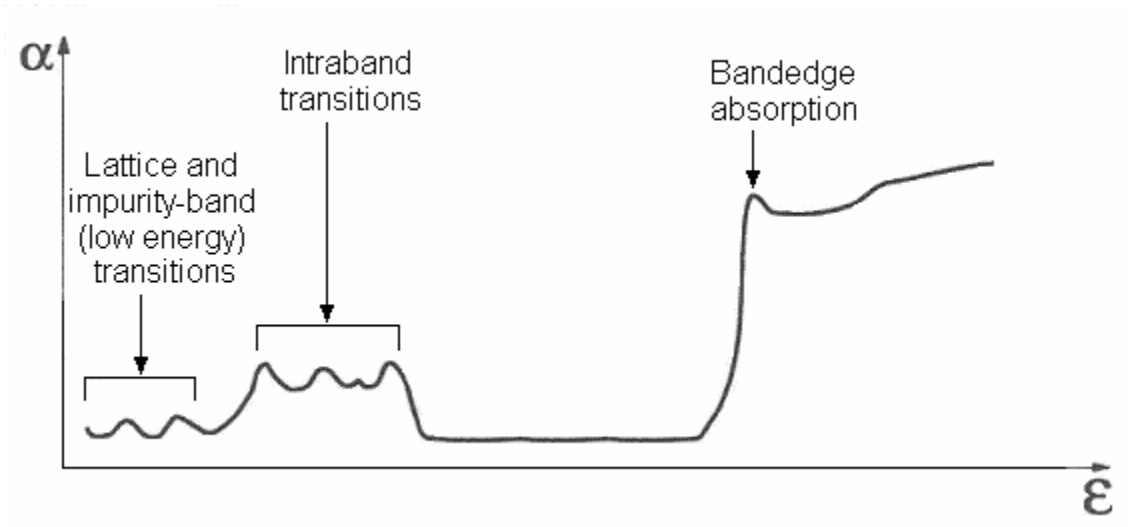

Fig. 2- 13: A schematic depicting some possible absorption transitions for a semiconductor (3:150).

Another important characteristic that can be extracted from absorption spectra is the functional dependence of bandgap energy on sample temperature. As temperature increases, the conduction band shifts to lower energy in relation to the valence band due to the expanding lattice. To determine how this affects the bandgap, several absorption measurements of E_g can be made at different temperatures for a given material. These measurements are then fitted using a Varshni equation:

$$E_g(T) = E_g(0) - \frac{\alpha T^2}{T + \beta} \qquad [2.5\text{-}3]$$

where $E_g(0)$ is the bandgap energy at absolute zero, T is the temperature, and α and β are constants. This helps to predict what energies are expected to be observed when the material is placed in different environments.

Many other characteristics of the semiconductor can be found through the absorption technique, including determining what impurities are present in the sample and which, if any, of the other transitions described in the previous section are likely to

occur. For this reason, absorption measurements are an important tool in characterizing semiconductor materials.

2.6 Photoluminescence Measurements

Like absorption, emission of photons from a semiconductor is also a reliable method for characterizing semiconductors. By introducing a flux of equal energy photons (such as from a laser) onto a semiconductor, three distinct processes occur: (1) electrons are excited into higher energy levels, and (2) the electrons re-combine with holes in the valence band of the material creating (3) emission of light (photons) from the sample. This light is called photoluminescence. By collecting and analyzing these emissions, several physical properties of the material can be determined.

In order to extract these properties from the photoluminescence collected, it is necessary to know exactly what is being observed. A typical photoluminescence plot is given as the intensity of the emission versus the energy at which it took place, as depicted by Fig. 2-14. The shape of the curve is defined by two electron limiting functions that have been discussed previously. The density of states function (2.2-3, -4) limits the minimum energy emission to starting at the bottom of the conduction band. From there, the allowed number of electrons transitioning from the sample increases as a function of the square root of the energy. Since the conduction band moves relative to the valence band with temperature change to the sample, the minimum energy limit can also be shifted due to temperature. To bring the number of emissions taking place down the higher the energy gets, the Fermi-Dirac distribution comes into effect. Since the sample is being excited through an outside flux of photons, a quasi-equilibrium is created within

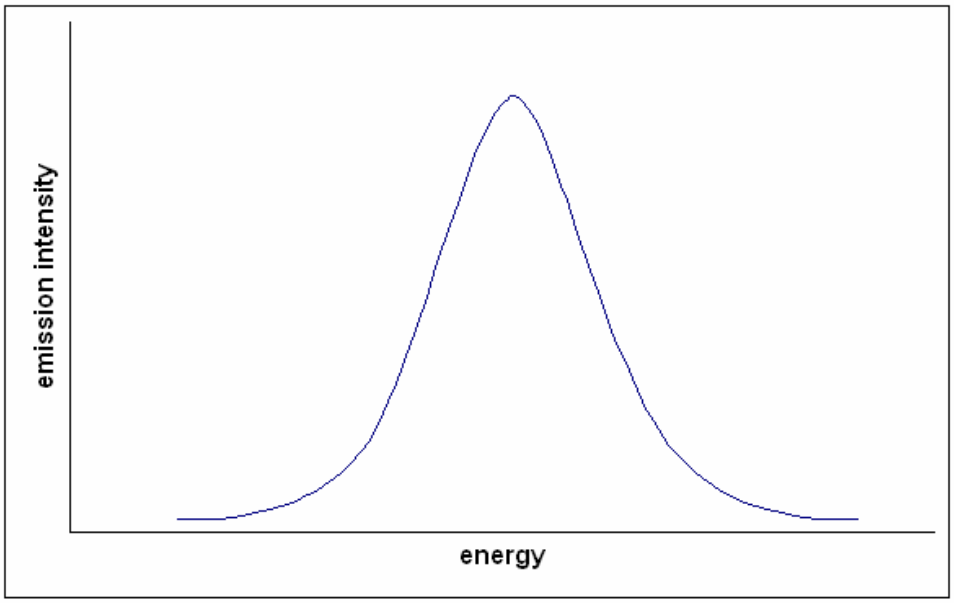

Fig. 2- 14: An example of what a typical photoluminescence emission spectrum of a semiconductor looks like.

the conduction and valence band separately. For this reason, a quasi-Fermi-Dirac distribution is formed for each band. This limits how high in the conduction band the electrons are allowed to occupy, thus limiting the high energy side of the emissions made. However, unlike the density of states function, the quasi-Fermi-Dirac distribution is effected by the temperature of the carriers involved, not the semiconductor as a whole.

Since the Fermi-Dirac distribution is carrier temperature dependent, a semiconductor can be made to have broader or narrower photoluminescence spectra by simply increasing or decreasing the excitation power, respectively. By increasing the power, the total number of electrons that are excited into the conduction band also increases, which means higher energies are being filled within the band resulting in an increase of temperature of the electrons. The electron temperature, T_e, is the deciding factor on how broad the emission peak is. Knowing that it only changes the higher

energies of the peak of the emission spectrum, T_e can be determined from this side of the photoluminescence. In order to determine the electron temperature for a steady state system, the luminescence signal is approximated by a constant multiplied by the product of the electron and hole distributions (given by equations 2.1-5 and 2.1-6):

$$I(h\nu) \sim f_c(E_e)[1 - f_v(E_h)] \qquad [2.6\text{-}1]$$

where E_e and E_h are the energies measured with respect to their band edges (10:135). Making the assumption that the excitation photon is such that E_e and E_h are much greater than their quasi-Fermi energies, the photoluminescence intensity can be re-written as:

$$\begin{aligned} I(h\nu) &\sim f_c(E_e)[1 - f_v(E_h)] \sim \exp[-(E_e + E_h)/k_B T_e] \\ &= \exp[-(h\nu - E_g)/k_B T_e]. \end{aligned} \qquad [2.6\text{-}2]$$

Using this equation and fitting a line to a given photoluminescence distribution of the high energy tail of the conduction to valence band transition, the electron temperature can be determined. How each variable determines the photoluminescence peak is depicted in Fig. 2-15.

Much like the absorption spectrum, photoluminescence also provides several insights into the make-up of any given material. Each peak in a photoluminescence spectrum can be labeled by a transition that is occurring within the semiconductor and leads to a particular property. Even the band structure of the material can be determined by peaks found in the spectrum. Since no two samples of material will ever be exactly the same, photoluminescence studies prove to be a valuable tool.

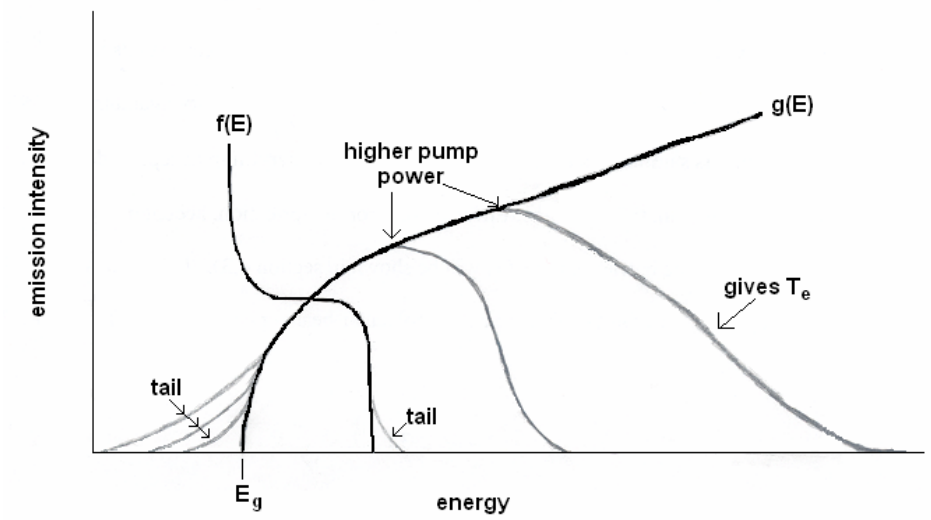

Fig. 2- 15: The photoluminescence limiting factors from the band-to-band emission is depicted. The density of states function [g(E)] limits the low energy side of the emission while a quasi-Fermi-Dirac distribution [f(E)] limits the high energy side. With a higher pump power, more electrons are excited into higher energy states; in return, a broader peak is observed.

2.7 Quantum Well Structures

A valued property that can be created in a semiconductor is to make particular emissions more likely to occur. This can be done by confining the excited electrons in the location where the desired emissions take place. By growing a low-energy bandgap material in-between two higher energy bandgap semiconductors, a well where the electrons and holes get trapped is formed. This configuration is referred to as a quantum well structure due to the properties of the carriers within behaving similarly to the single quantum well problem in quantum mechanics. It is this similarity that determines the allowed energy levels within the well.

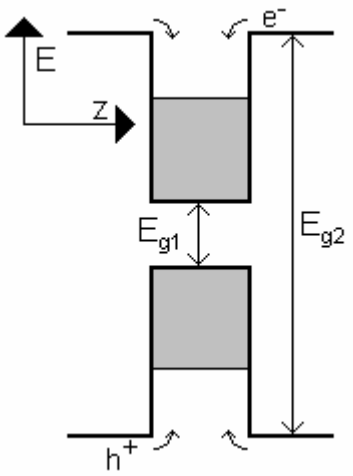

Fig. 2- 16: A schematic of a quantum well structure. A quantum well is created when a semiconductor with a small bandgap energy (E_{g1}) is grown in-between two semiconductors with larger bandgap energies (E_{g2}). As a result, the electrons and holes flow into the well and are then confined within.

Analogous to the infinite well problem, the quantized energy states found within the conduction band of the well are given by

$$E_l = \frac{\pi^2 \hbar^2 l^2}{2 m_e^* L_z^2}, \quad l = 1,2,3,... \qquad [2.7\text{-}1]$$

where E_l is the quantized electron energy measured from the conduction band minimum, l is the level within the well, and L_z is the well thickness. A similar equation can also be written for the valence band. It should also be noted that in order for the well to have quantization of the states, the energy between the subbands must be greater than $k_B T$. In other words, the well thickness must be small enough such that $E_{l2} - E_{l1}$ is greater than the energy due to temperature. If this is not the case, the electrons in the well behave as described earlier for bulk semiconductors (3:80). To describe the energy at which these quantized levels lie, equation 2.1-4 is referred to getting,

$$E = E_l + \frac{\hbar^2 k^2}{2 m_e^*} \qquad [2.7\text{-}2]$$

which gives solutions similar to those shown in Fig. 2-17. Hence, by choosing the dimension of L_z, the forbidden energy gap can be altered.

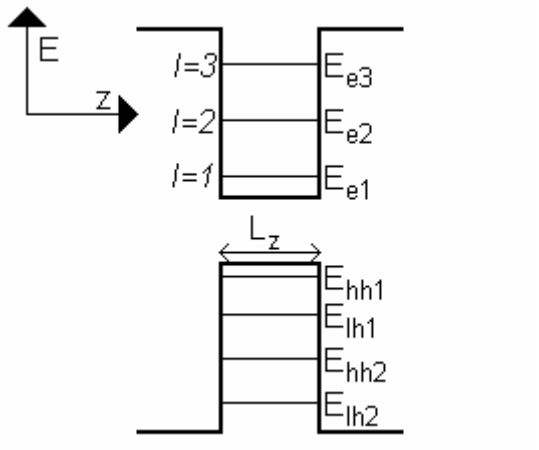

Fig. 2- 17: The quantized energy subbands found in a quantum well structure. This shows the discrete levels formed by the electrons in the conduction band and the heavy-holes and light-holes in the valence band.

With knowledge of where the energy levels lie within the quantum well, the density of states will provide insight on how many carriers lie within each of the subbands created. As started with in the bulk semiconductor, the allowed values of k in the material are found by:

$$\begin{aligned} k_x L_x &= 2\pi n_1 \\ k_y L_y &= 2\pi n_2 \\ k_z L_z &= 2\pi n_3 \end{aligned} \qquad [2.7\text{-}3]$$

where we will assume that $L_z << L_x, L_y$. So, the allowed values of k are found to occupy a volume of $(2\pi)^3/(L_xL_yL_z)$, and the inverse value of $(L_xL_yL_z)/(2\pi)^3$ gives the density of allowed points in k-space. Including two possible spins for the electrons in each of the allowed states and keeping k_z equal to constant π/L_z, the number of allowed states in the interval E and E+dE is:

$$N(E)dE = \frac{m^*}{\pi\hbar^2 L_z}dE \qquad [2.7\text{-}4]$$

provided that $E > E_l$ (3:85). This shows that the density of states is a constant, independent of the energy. This creates a stair-like density of states that is contained within the density of states for a bulk semiconductor as seen in Fig. 2-18. This restricts the number of states as a function of energy allowing for more electrons to have the same energy within the well. This has a profound effect for a laser created out of the quantum well structure since the gain coefficient is proportional to the number of excited electrons multiplied by how they are spread out in energy (17:473). This indicates that the laser light can be created very effectively. So, due to their flexibility in changing the energy transitions allowed and their ability to hold many electrons at the same energy, quantum well structures provide a variety of opportunities in semiconductor lasers.

Having an understanding of the physics of a quantum well, attention is turned to the different types of quantum well structures. To this point, the discussion has only

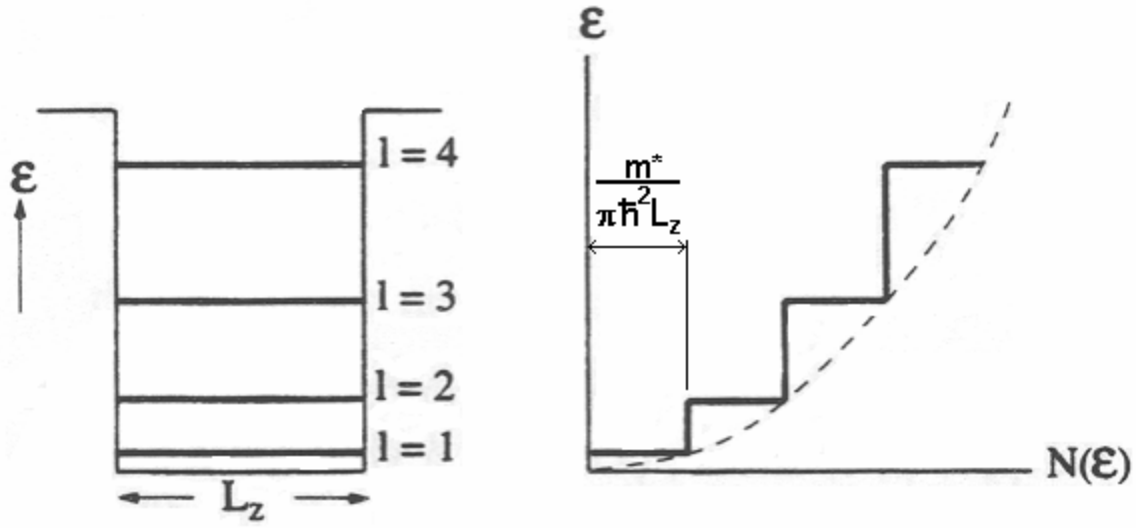

Fig. 2- 18: The energy subbands and their corresponding two-dimensional density of states formed in the z-direction of the quantum well. The dashed line represents the density of states found for a bulk semiconductor, as found by equation 2.2-2. (3:82)

involved one quantum well within the structure. However, several layers of this single quantum well set-up can be grown together to make a multiple quantum well, creating many more places where carrier confinement can occur. Where the confinement for the two carriers occurs relative to one another gives quantum wells two distinct categories of structures. Type I structures have the wells for the electrons and holes found within the same material such that they are aligned spatially. When the wells for the two different carriers are formed in adjacent materials so that they are spatially offset to each other, this is referred to as a type II quantum well. Both types are depicted in Fig. 2-19.

Regardless of the type of structure the quantum well is, the optical transitions that occur within hold the same properties and rules as those for the bulk semiconductors. Transitions can be made between any of the created energy subbands, including bands created by impurities. Phonons are also still present moving the electrons and holes along the energy bands and allowing for indirect transitions. Due to the similarities in

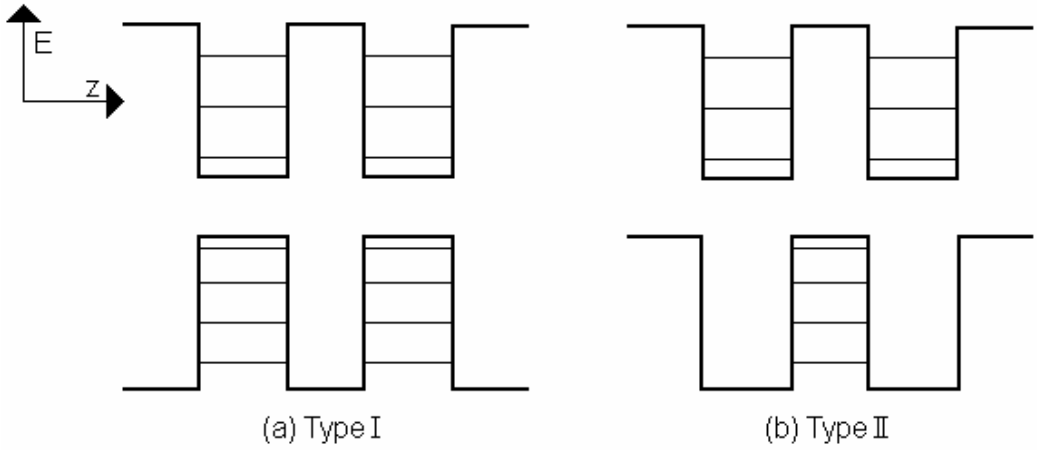

Fig. 2- 19: The two types of quantum well structures. (a) Type I quantum wells have the wells for the electrons and holes within the same material; this causes them to be spatially aligned. (b) In a type II quantum well, the wells are found within different materials causing them to be spatially unaligned.

their optical transitions, the absorption and photoluminescence spectra that are taken from quantum well structure are formed and analyzed the same way as bulk material. The obvious difference between the two is that the quantum well will provide a positive shift in energy above the bandgap of the bulk well material. Another difference in the quantum well is that if the energy of the incident light onto the sample exceeds the energy of the barrier bandgap, both the well and barrier transitions will appear on the spectra. Regardless of the differences, absorption and photoluminescence measurements are equally as useful in determining the characteristics of a quantum well.

3. Experiment

This chapter provides the setup and procedures used to take the absorption and photoluminescence spectra of the samples. It begins with a description of the samples studied in this experiment followed by the methods used to analyze them.

3.1 Samples Studied

The samples in this experiment are a combination of bulk and type I quantum well structures consisting of indium arsenide antimonide ($InAs_{1-x}Sb_x$). By choosing bulk samples that correspond to the composition of the quantum well, the optical behavior of the material can be compared and contrasted for the two cases. The samples used and their compositions are listed in Table 3-1, while Fig. 3-1 depicts the layering of the quantum wells used.

Table 3- 1: The sample set of the semiconductors used and their compositions.

Sample	Description	Composition	Substrate
93-045	bulk	$InAs_{0.911}Sb_{0.089}$	GaSb
94-099	10 QW	$InAs_{0.9117}Sb_{0.0883}/In_{0.88}Al_{0.12}As_{0.878}Sb_{0.122}$	$AlAs_{0.085}Sb_{0.915}$/GaSb
94-035	bulk	$InAs_{0.821}Sb_{0.179}$	GaSb
94-034	10 QW	$InAs_{0.83}Sb_{0.17}/In_{0.95}Al_{0.05}As$	$AlAs_{0.08}Sb_{0.92}$/GaSb

The first material listed for the quantum well samples is where the well is created, while the second is the barrier material. Each sample was epitaxially grown on top of a gallium antimonide substrate, while the quantum wells have an extra cladding layer of aluminum arsenide-antimonide ($AlAs_{1-x}Sb_x$) to reduce strain.

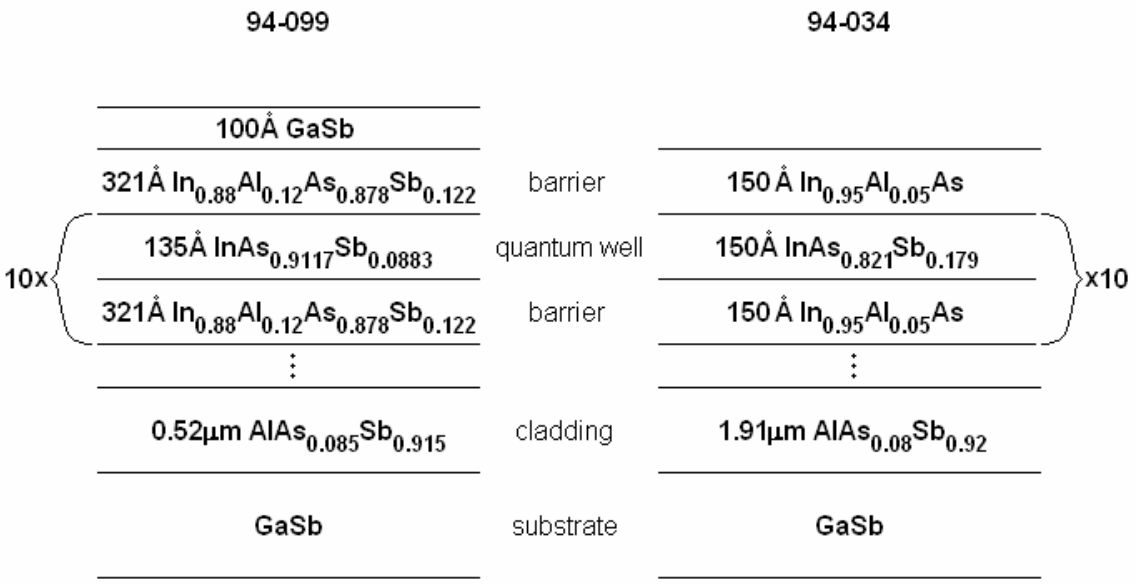

Fig. 3- 1: Diagrams depicting how the quantum well samples used for experimentation were layered.

3.2 Absorption Configuration

The samples were placed onto a copper cold-finger and inserted into an Air Products Helitran cooling system with the absorption setup seen in Fig. 3-2. The Helitran is capable of operating down to 4.2K temperatures through liquid helium (LHe) cooling and vacuum pumping. The chamber is continuously pumped using an Alcatel turbo pump setup. In order to isolate the extreme temperatures from the zinc selenide windows, a copper heat guard was placed around the samples. An Air Products Digital Temperature Indicator monitored the samples temperature, while a Hewlitt Packard E3611A DC Power Supply was used to control the sample heater to allow for different temperatures to be measured.

The absorption was determined by positioning the Helitran within the sample chamber of the Bio-Rad FTS-60A Fourier transform spectroscopy (FTS) system. The

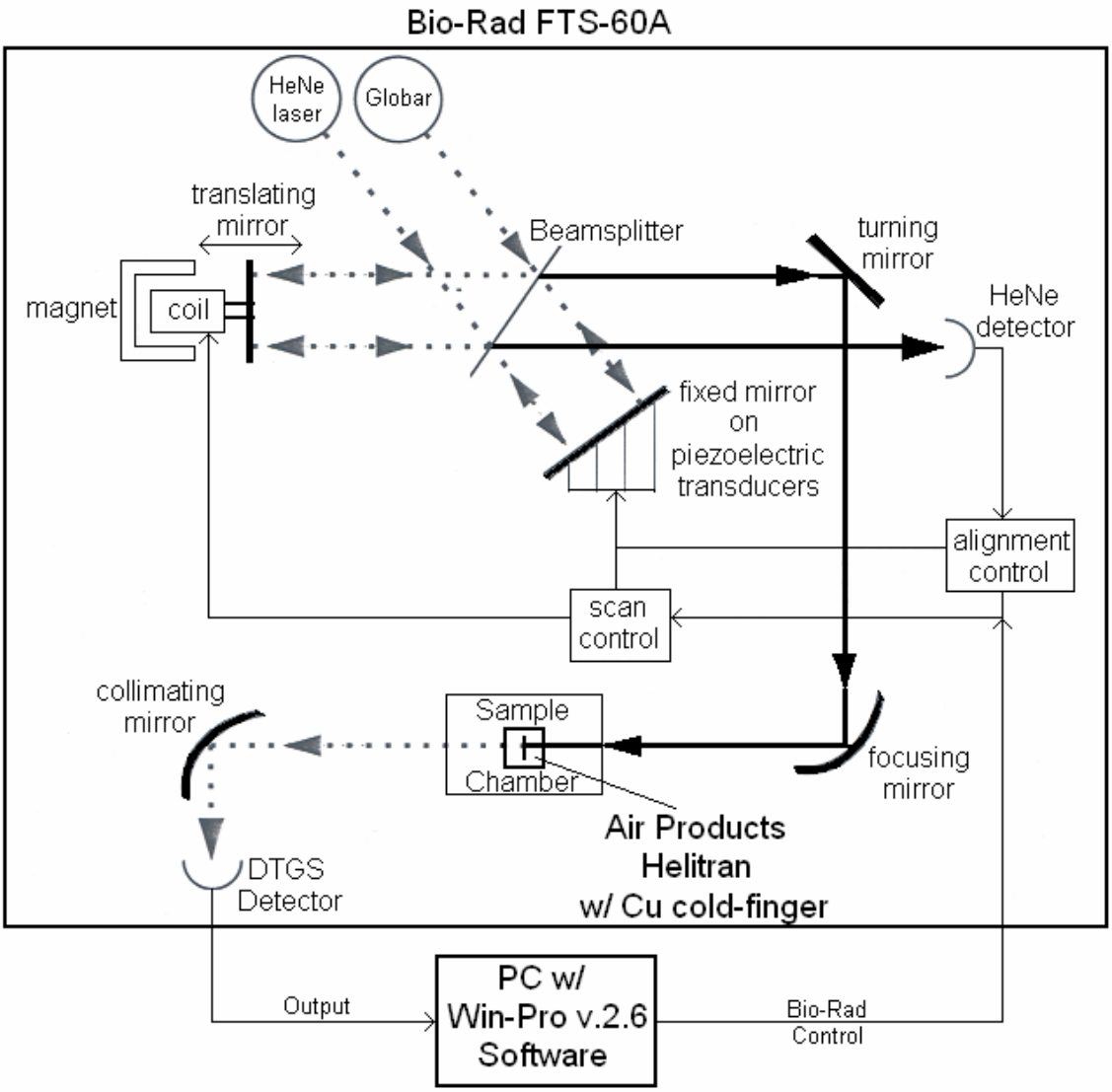

Fig. 3- 2: The absorption configuration used for this experiment to get the bandgap energies of the antimony-based samples.

Bio-Rad works on the principle of a Michelson interferometer, meaning it utilizes path length differences between a split beam and the interference pattern that they create to determine the response of the sample. If more detail is desired, refer to Michael Marciniak's dissertation, which describes the principles governing the apparatus more closely (12:5-2). In order to do absorption measurements in the mid-infrared range, the

ceramic IR source (labeled globar in the figure) is chosen to provide the background radiation for the experiment, while the deuterated triglycine sulfate (DTGS) detector is chosen to collect the response in the Bio-Rad. To collect the maximum response possible, the sample chamber is purged with nitrogen gas using a Balston 75-52 FT-IR Purge Gas Generator. By doing this, absorption caused by atmospheric gases is minimized.

3.3 Absorption Technique

Before mounting any samples onto the copper cold finger, a spectrum representing the total amount of ceramic IR light that reaches the detector must first be taken for reference. This is done by simply running the experiment with no sample covering the hole in the copper cold finger. In order to ensure that the maximum signal is getting through the hole, the Helitran is attached to a set of micrometers to allow for controlled movement. By utilizing the Win-Pro software to view the signal being created, the hole can be re-positioned until a maximum signal is found. Once this is accomplished, the background spectrum can be taken.

Having a reference, the sample is mounted to cover the hole in the copper cold finger and placed back into the Helitran system. In order to start cooling the samples, the Alcatel turbo pump is turned on to isolate the samples from the outside environment (preventing frost from forming in the chamber). To isolate the chamber from direct liquid helium contact, the heater found at the helium transfer entrance to the Helitran must be plugged in, allowing for only helium gas to enter the sample chamber. With the chamber evacuated and the heater on, the LHe transfer can be done by inserting the

transfer tube leading from the Helitran into a liquid helium tank. The flow created is monitored and changed using a set of two needle valves leading off the transfer tubing and Helitran unit. By changing the flow rate, the temperature of the samples can be changed and maintained.

While the desired temperature is being reached, the alignment of the Helitran system can be done using the micrometer stages described earlier. Besides inserting and aligning the samples, the entire rest of the experimental process is run through the Win-Pro software. Once the temperature has settled to its desired point, the initial reference spectrum is loaded in as the background using the *Collect/Rapid Scan* feature in the program. Using this information, by running a *Scan,* the program outputs the percent transmission of the background that the detector sees. To clarify, if no sample is placed over the hole, the scan should output that one-hundred percent of the original signal is being seen by the detector; if a sample is present, the scan should output a spectrum showing less than one-hundred percent of the original signal due to reflection and absorption caused by the sample. Since the samples absorption is of interest, the program also allows for the transmission spectrum to be transferred into an absorption spectrum.

3.4 Photoluminescence Configuration

The samples were placed onto a copper cold-finger and inserted into an Air Products Helitran cooling system with the photoluminescence setup seen in Fig. 3-3. The same Helitran setup is used as that for the absorption experiment with the exception of the positioning of the entrance and exit windows, as well as the exit window being made of calcium flouride.

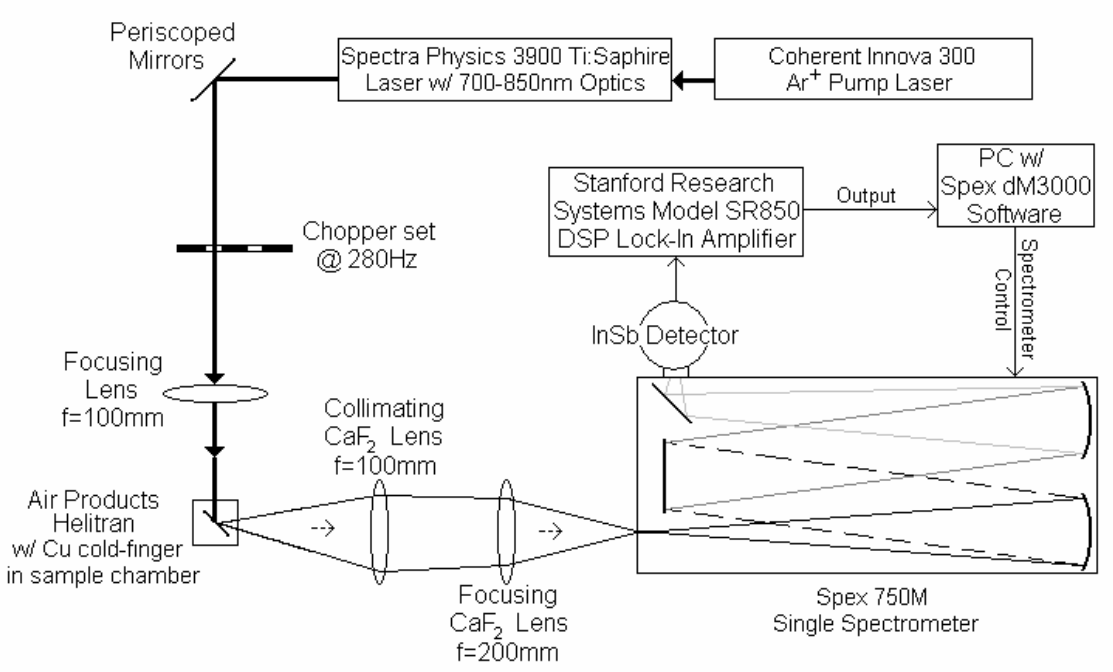

Fig. 3- 3: The table configuration used for this experiment to obtain the photoluminescence from the antimony-based semiconductors.

The sample was excited using a variable-wavelength output of a Spectra Physics 3900 Titanium:sapphire laser, which is focused into a 0.5mm diameter spot on the sample by a 100mm focal length lens. The optics placed within the Ti:sapphire laser cavity allowed for tuning from 700 – 850nm wavelengths by turning a bi-refringent crystal with an actuator. A Coherent Innova 300 argon-ion laser working off both the 488nm and 514nm emission lines was used as a pump for the excitation laser.

The luminescence created by the samples is scanned through using a Spex 750M spectrometer. Slit widths were monitored by hand and a computer with the Spex dM3000 software controlled the motorized grating. This software also collected the data taken by an indium-antimonide detector, which detects emissions in the 1 – 5μm range. Due to the detector's inability to photon count, the luminescence was input at a rate of

280Hz using a chopper, and the detected signal was amplified using a Stanford Research Systems Model SR850 DSP lock-in amplifier.

To get the luminescence from the sample chamber to the spectrometer for analysis, a set of two calcium-fluoride lenses was used. These lenses were selected to match the f-number of the spectrometer and sample chamber window geometry. Using this set-up, the luminescence from the quantum wells exits the chamber window, is collected and collimated by the first lens and focused into the spectrometer entrance slit such that the collected light illuminates the grating fully.

3.5 Photoluminescence Technique

Before any photoluminescence can be observed, the semiconductors must first be cooled down to low temperatures. Since this is the same Helitran system used in the absorption experiments, the same process for getting the samples cooled applies.

With the desired temperature found for this experiment, the optics of the system need to be aligned to ensure maximum signal into the spectrometer. Before the optics within the spectrometer were switched to meet the needs of this experiment, the wavelength of the Ti:sapphire laser was set to 710nm by using a Jobin-Yvon-Spex Spectrum One gallium arsenide array detector to view the output. This is the laser excitation wavelength used for every experiment. Before each experiment, the laser system must be turned on and allowed to settle. Both lasers take about an hour to produce a steady output (this can be started before liquid helium is introduced). While the lasers are settling, the laser can be adjusted onto the desired sample.

With the Ti:sapphire laser now settled and focused onto the sample, the lenses that direct the photoluminescence into the spectrometer can be aligned. In order to achieve collimation of the photoluminescence, the first lens is placed at its focal length away from the sample. This can be observed by placing a white piece of paper in the optical path behind the lens and following the light path produced off of the sample to the focusing lens. Perfect collimation is not necessary, but the second lens of the system should be fully illuminated by the first. With the second lens fully illuminated, the light can be traced coming out of this lens down to a spot. By adjusting the position of this lens, the spot can be focused onto the slit entrance of the spectrometer. This provided for a signal to be detected from the sample. In order to completely maximize the signal, a quick scan of the sample's photoluminescence revealed a rough idea of where the peaks lie within the sample. Using a feature on the Spex dM3000 software, the wavelength that produced the largest peak can be locked onto and the output current of the detector can be viewed continuously. Utilizing this feature, both lenses were adjusted to get the maximum possible output.

With the incoming signal maximized, photoluminescence studies were now ready to be conducted. To determine the wavelength steps to be used when collecting the data, the spectral resolution of the system was necessary. The resolution of a spectrometer can be determined through the grating characteristics and the entrance/exit slit openings as

$$\Delta\lambda = \frac{aw}{mf} \qquad [3.3\text{-}1]$$

where a is the grating spacing, w is the width of the exit slit, m is the order of the diffraction observed, and f is the spectrometer's focal length. In this experiment, the grating was blazed at 3μm with a 300grooves/mm spacing ($a=300^{-1}$mm), the first order

was always observed (m=1), and the focal length of the spectrometer was 750mm. So, in order to achieve an accuracy of 1nm, the entrance and exit slits must be open to 0.225mm. By determining the spectral resolution, an appropriate step size can be chosen for the experiment.

Another important consideration in the experiment is the excitation power used. By varying the power exciting the sample, the number of electrons excited into the conduction band can be varied. The power delivered by the Ti:sapphire laser was determined by the pump power of the Ar^+ laser. By varying the output of the pump, the excitation laser could provide powers in the range of 5 – 220mW.

3.6 Quantum Well Modeling

To model the quantum well energy subbands for the samples, a Finite Element Method code (femb) written by L.R. Ram-Mohan was implemented. To run the femb program, the compositions of the well and barrier regions must be created using the list of materials given in the femparm.inp file provided with the code; all the material parameters needed to carry out the calculations are found within this file.

In order to create the material parameters for the well and barrier, a linear interpolation of the combined materials that create each region is used. For example, if the well is made up of the binary compounds AB and AC creating $AB_{1-x}C_x$, the new ternary well material parameters would be found using the appropriate percentages of each binary compound:

$$AB_{1-x}C_{x\ parameter} = (AB_{parameter}) \times (1-x) + (AC_{parameter}) \times (x). \qquad [3.5\text{-}1]$$

The only parameter where this does not hold true is the bandgap energy. Since the energy gaps of ternary compounds do not follow a linear pattern in accordance to their compositions, a quadratic equation of the form

$$E_g(AB_{1-x}C_x) = E_g(AB)\times(1-x) + E_g(AC)\times(x) + b\times(1-x)\times(x) \qquad [3.5\text{-}2]$$

where b is known as the bowing parameter, is used. The bowing parameter for several different ternary compounds is also included in the femparm.inp file. With all the parameters set for the well and barrier, the quantum well energy bands can be predicted by the program.

By running the femb program, two desired results are computed. First, the program calculates the well and barrier materials' bandgap energies for a given temperature and offsets them from each other appropriately. This results in an energy versus z-direction plot that depicts the quantum well. The program also creates a matrix representing the Schrodinger equations that correspond to the structure; this includes all the parameters previously calculated for the semiconductors in use. This matrix is a Hamiltonian, or representation of the total energy of the system, meaning that by diagnolizing it, the resulting eigen values represent the allowed energy levels of the structure. By weeding out those that lie outside or within the well, the quantum well energies can be predicted.

4. Data and Results

This chapter describes the experimental findings of the research conducted.

4.1 Calibration

Before discussion of the results of the experiments, the two systems involved were first shown to be calibrated to one another for consistency across the absorption and photoluminescence spectra. This was done by allowing a broad spectrum curve to be filtered out by an OCLI band-pass filter normally used as a coldfilter in Cincinnati Electronics InSb detectors. Since the filter is actually a quarter-wavelength dielectric stack, resonance occurs in the passing light creating peaks and valleys that can be used for calibration. To calibrate the Bio-Rad FTS-60A system, the filter is treated as just another sample to be scanned and a broadband source is already incorporated. However, to calibrate the Spex 750M spectrometer, a blackbody source is used with the setup shown in Fig. 4-1. The blackbody curve is created by an Electro Optical Industries, Inc. variable temperature blackbody point source. In order to determine what temperature the

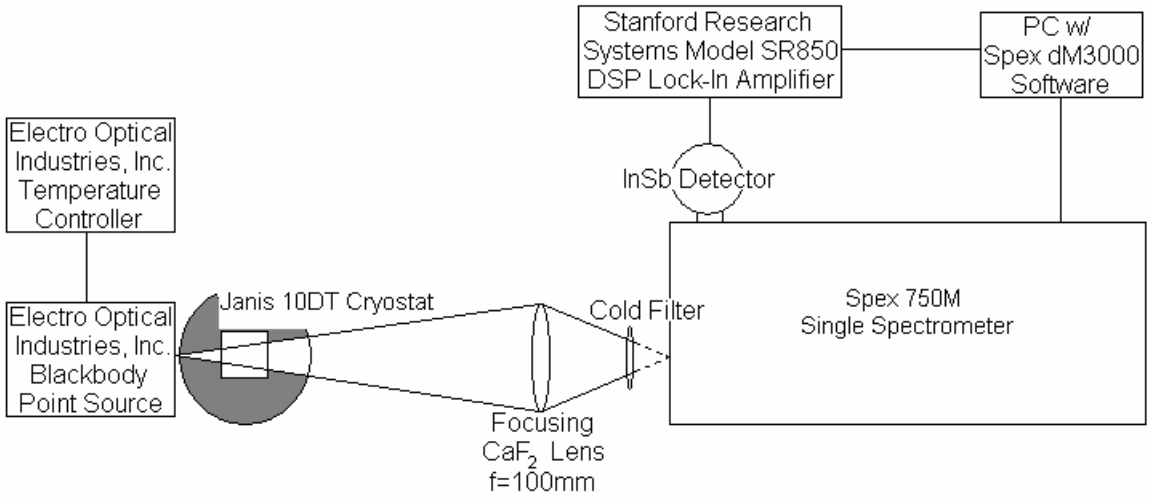

Fig. 4- 1: The setup used to calibrate the spectrometer to the correct wavelengths.

blackbody should be for calibration, Wien's Law is used to synchronize the center of the filtered light with the peak of the blackbody curve:

$$\lambda_{peak}(\mu m) = \frac{2898}{T_{BB}(K)}. \qquad [4.1\text{-}1]$$

With the correct blackbody temperature selected, the transmission of the filter can be measured, and the spectrometer is calibrated. By calibrating both instruments, the results of each will be consistent with one another.

The filter chosen for the calibrations was identified as an OCLI filter with P/N W03540-6 and a transmission range of 2.8–4.35μm. Given this range, the ceramic infrared globar source was used as the reference to calibrate the Bio-Rad system while a blackbody source was set to a temperature of 820K to calibrate the Spex 750M spectrometer. The transmission percentage through the filter of the broad spectra sources provided the necessary modulations for calibration, shown in Fig. 4-2. By comparing the

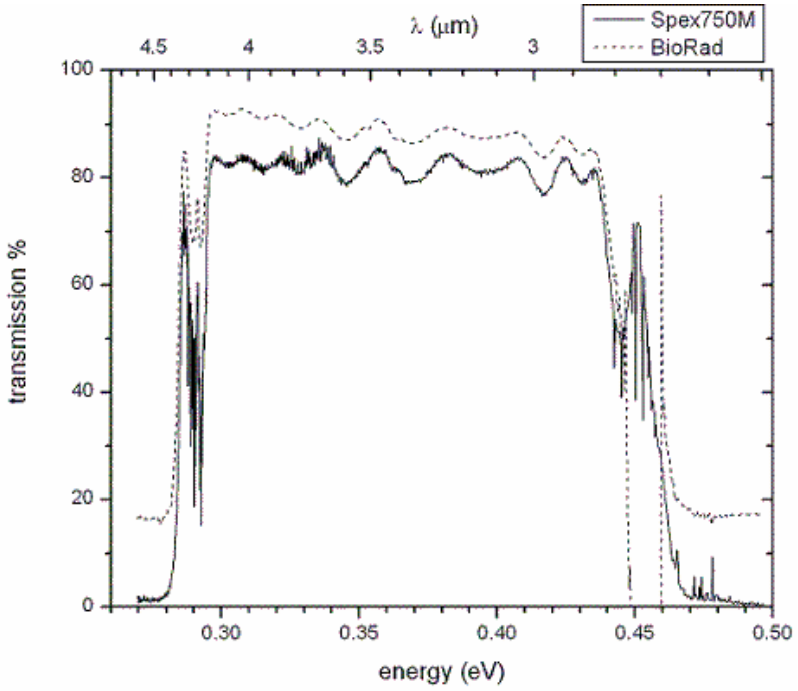

Fig. 4- 2: The experimental transmission of the W03540-6 OCLI filter.

resonance peaks, it was found that the two instruments were calibrated to within 0.76meV of each other. Since the error bars given by the instruments themselves could accommodate such an error, a straight one-to-one comparison can be made between the spectra obtained from each system.

4.2 Absorption

After the calibration was complete, attention was turned to finding the absorption edges of the samples selected. The *rapid scan* collection method of the Win-Pro software was utilized to obtain the spectra with the following experimental parameters (with reasoning in parentheses):

Electronics:
Speed: 5 kHz (suggested when using the DTGS detector)
Filter: 1.2 (suggested when using 5 kHz speed)
UDR: 1 (collects spectrum at every 1/2 λ mirror translation)
Resolution: 4cm^{-1} (suggested for solid samples)
Sensitivity: 16 (to get maximum signal)
Scans to Co-Add: 500 / 1000 (minimizes background noise)
Save Range: 500 – 7000cm^{-1} (breadth of spectrum)

Optics:
IR Source: ceramic
Beam: internal
Detector: DTGS
Beamsplitter: KBr.

Changing the wavenumbers into energy units, the resolution of the Bio-Rad FTS-60A system was set to 0.496meV, and a range of 1.429 – 20.00μm was set to observe free carrier, band edge, and substrate absorption in each sample. With these parameters set, the absorption experiment was begun.

To start the experiment off, background data was taken. By allowing the ceramic light source to pass through the exact experimental setup that the samples were in, a measure of the maximum amount of light the detector could be hit with was determined.

An example of the background used can be seen in Fig. 4-3. Notice that one side of the signal drops off sharply as the other gradually declines. This is due to the cut-off of the zinc selenide windows used in the Helitran as opposed to the natural decline in signal produced by the ceramic source. Knowing the maximum expected response of the detector from the source, the samples were mounted and inspected.

With the sample in place, the response from the detector was logically reduced (also seen in Fig. 4-3). Several factors contributed to this loss of signal: the light got

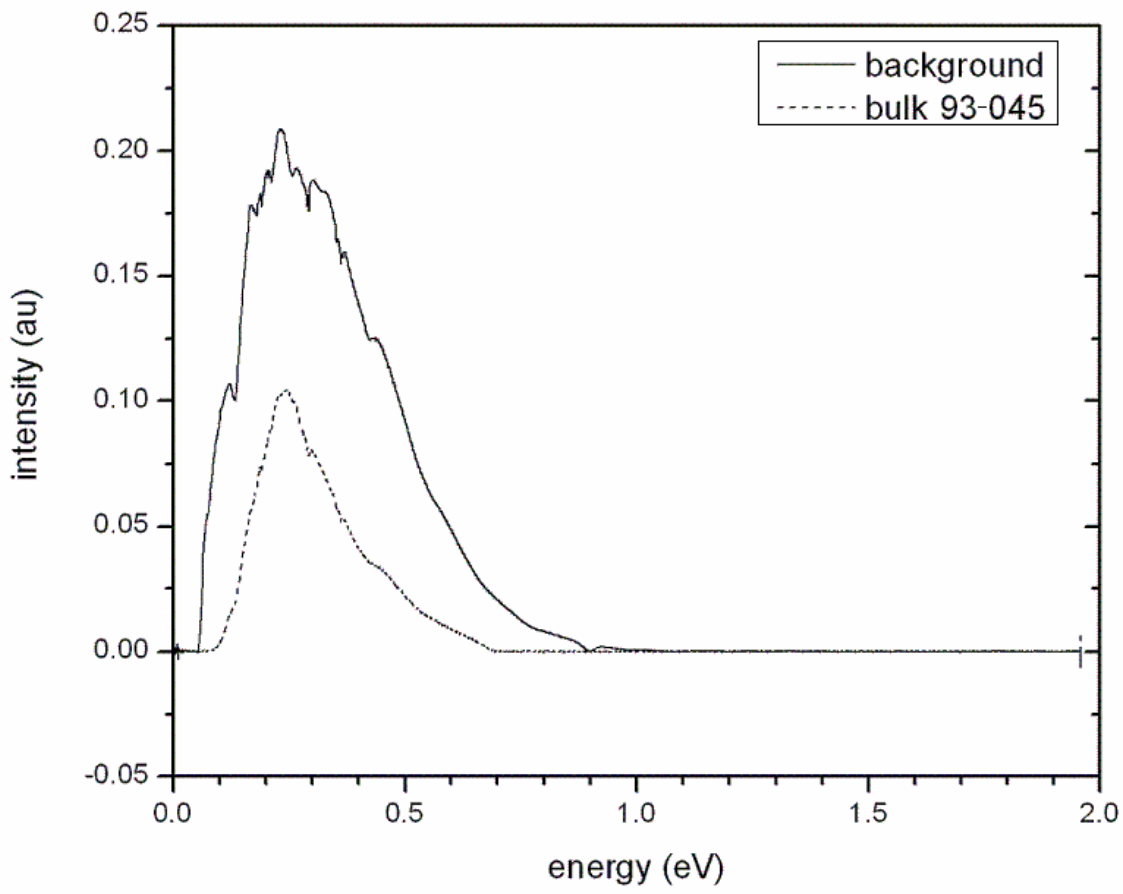

Fig. 4- 3: The ceramic IR source response output by the detector with nothing obstructing the path (background) and with bulk sample 93-045 in the path. Notice how the sample's response is not as wide and reduced from the reference.

reflected off of the surface of the semiconductor (this could happen at each interface that the light encounters), the light got absorbed by the sample, or the light got transmitted through the material but was refracted in such a way that the light did not reach the detector. Since there were several contributing factors to the loss of signal, the absorption of each sample was defined as

$$absorption = \log_{10}\left(\frac{I_{background}}{I_{sample}}\right) \qquad [4.2\text{-}1]$$

The Win-Pro software had a feature that automatically transformed the transmission scans into their respective absorption curves. This feature was taken full advantage of, and examples of the curves it produced are shown in Fig. 4-4.

The high absorption on the low energy side (extreme left) of the spectra was a result of free carrier absorption. This was a result of the electrons (holes) already found within the conduction (valence) band taking the energy to promote themselves higher into their band. The expected trend would be to see less free carrier absorption the lower in temperature the sample gets since fewer free carriers were available. However, in this experimental setup, the broad band of the ceramic source continuously provides energy for electrons to be promoted into the conduction band, thus creating free carriers. This resulted in allowing for no noticeable reduction to occur.

Traveling across to the high energy (right) side of the spectra, the high absorption found there was a result of absorption caused by the substrate of the samples. The energies found here surpassed the bandgap energy of gallium antimonide (0.812eV). The absorption was very strong in this region because the substrate made up the majority of the thickness of the sample.

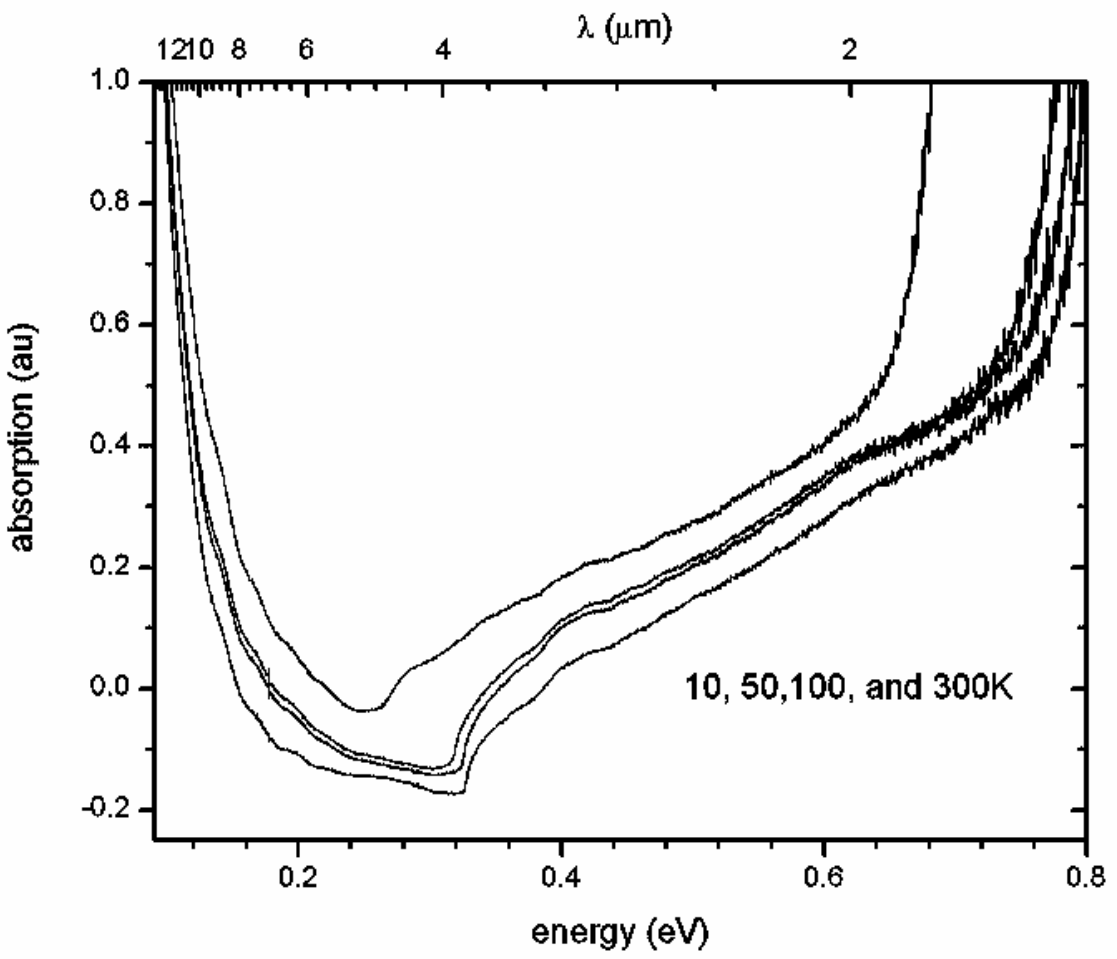

Fig. 4- 4: The absorption spectra of bulk sample 93-045 ($InAs_{0.911}Sb_{0.089}$) taken by the Bio-Rad system at various temperatures.

Found in the middle of the spectra, before the effect of the substrate was seen and right after the free carriers died out, the rise in absorption resulted from the first allowed energy transition of the sample; it was this spectral area that was the focus of this part of the experiment. For the bulk samples, this increase in absorption depicted where the bandgap energy lay. For the quantum wells, it represented the first allowed energy transition within the well (electron level 1 to heavy-hole level 1).

Extracting the Energy Transition through Curve Fitting

The first method used to extract the desired energy transition of the samples was curve fitting. This technique fit the experimental absorption data taken to its corresponding theoretical equation. The density of states function could be used to represent the bandedge created by the sample (eq. 2.2-2) while the free carrier absorption could be represented by its own density of states equation. However, since only the energy of the first allowed transition in the sample was desired, the general shapes of those curves were used to fit the data.

Before the absorption curve of the bandedge could be determined, the free carrier absorption was first subtracted out of the data; this allowed for the first energy transition of the samples to be found at zero absorption. The general equation used to fit the shape of the free carriers was

$$absorption_{fc} = A + B\exp\left(\frac{-E}{T}\right) \qquad [4.2\text{-}2]$$

where A represented the loss due to scattering and the remainder of the equation gave the effect due to free carrier absorption (12:6-8). This equation was fit to the data (as well as all the other data fits hereafter) using Microcal's Origen software. The program fit the data by minimizing the sum of squares of the deviations of the theoretical curve chosen from the experimental points (14:320). Some examples of the free carrier absorption fitting are seen in Fig. 4-5.

With an equation for the free carrier absorption determined, this effect was then subtracted from the data to place the beginning of the bandedge at zero absorption. With

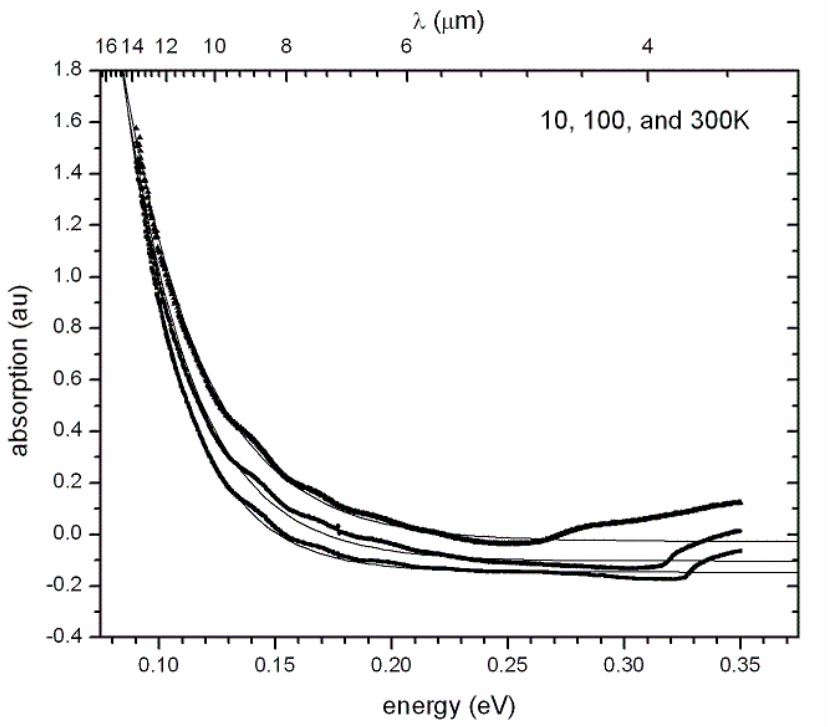

Fig. 4- 5: The free carrier absorption fit to bulk sample 93-045 ($InAs_{0.911}Sb_{0.089}$) at various temperatures.

this the case, the density of states parabolic shape was mimicked to extract the first transitional energy with the equation

$$absorption_{bandedge} = A(E - E_1)^{1/2} \qquad [4.2\text{-}3]$$

where E_1 gave the minimal energy transition that the sample could support. What these curve fits resembled can be seen in Fig. 4-6.

Unfortunately, only the bulk samples studied in this experiment could be analyzed using the curve fitting technique. Both of the quantum wells gave two very different and unexpected results for an absorption curve. In fact, one of these samples was found not to be a quantum well at all.

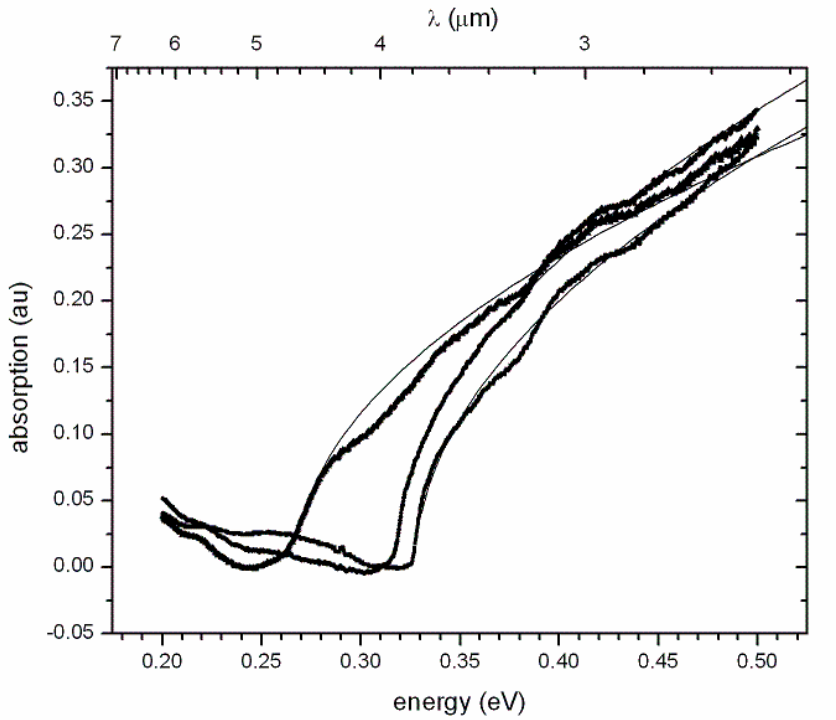

Fig. 4- 6: The bandedge fit to bulk sample 93-045 ($InAs_{0.911}Sb_{0.089}$) at various temperatures. Where the fit had zero absorption was taken to be the minimal energy transition of the semiconductor.

Problems with the Quantum Wells

When the quantum well sample of 94-034 ($InAs_{0.83}Sb_{0.17}/In_{0.95}Al_{0.05}As$) was scanned through using the Bio-Rad system, it was discovered that the sample did not seem to exhibit any kind of bandedge absorption. This was odd considering that its corresponding bulk sample fell within the range of the detection used, meaning an edge should appear just slightly higher in energy than that. However, upon closer inspection of the surface of the sample, it was discovered that there were no epitaxial layers to be found. Somewhere along the way, the quantum well layers were polished or scraped off of this sample, leaving only the substrate. To check if this was the case, a known gallium antimonide sample was used to compare the absorption curves, as seen in Fig. 4-7. With

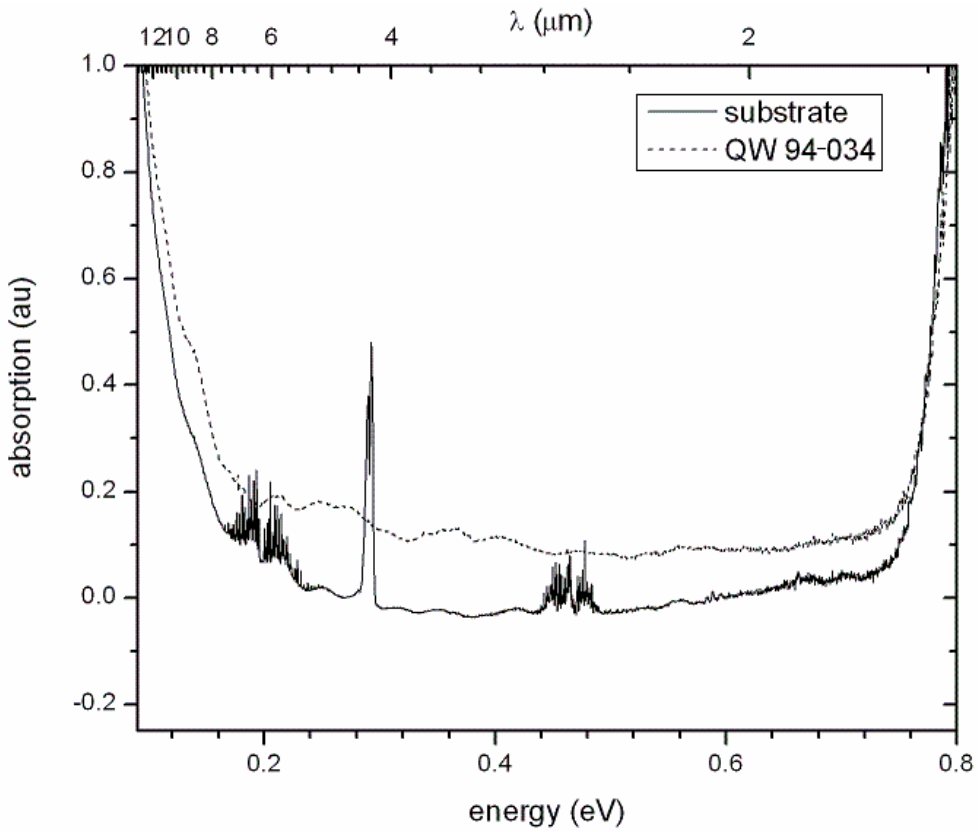

Fig. 4- 7: The quantum well 94-034 sample compared to a gallium antimonide sample labeled sample #5. Notice that both display the same characteristics (barring the large artifacts in the substrate which were caused by CO_2 and water absorption in the atmosphere).

the quantum well sample now verified to be just substrate material, nothing more was done with that sample.

With one quantum well totally out of the picture, all quantum well/bulk material comparisons fell to the 94-099 ($InAs_{0.9117}Sb_{0.0883}/In_{0.88}Al_{0.12}As_{0.878}Sb_{0.122}$) sample. Unfortunately, more obstacles were encountered with this sample. In order to get ideal absorption curves using this method, the sample should be polished on both sides and be large enough to cover the hole in the copper cold finger; sample 94-099 foiled on both counts. Although not polished, one side of the sample had previously been chemically etched, giving a rough look to the surface. Although an etched surface is better than a

totally unpolished surface, etching still causes the light to scatter as the light travels through the surface, degrading the signal. Furthermore, the sample did not completely cover the hole in the sample mount, allowing stray light to seep through to the detector without passing through the sample. Not wanting to risk ruining this sample through polishing, a larger number of scans were taken in an attempt to obtain a better average. This was the only remedy done to compensate for the problems for this sample.

Despite the challenges quantum well 94-099 presented, absorption curves still displayed good enough data to be able to see energy transitions created by the well, as seen in Fig. 4-8. However, it was also seen that another phenomenon was occurring in the quantum well spectra that was not present in those of the bulk samples; the apparent peaks and valleys in the absorption between the free carriers and substrate absorption were a result of an etalon effect. Referencing a Fabry-Perot etalon, the quantum well acted as a multiple beam interferometer consisting of two parallel, reflecting planar surfaces separated by a distance d, as shown in Fig. 4-9. Light that enters the etalon reflects several times inside the middle layer, creating a set of light rays exiting upon each reflection. The exiting rays then interfere with one another, either constructively or destructively, depending on their frequency and the planar separation. It was this constructive and destructive interference that created the peaks and valleys seen in the spectra. Since etalons are temperature independent, the observed phenomenon seems to fit well to this explanation. A more detailed description of the etalon effect seen can be found in Michael Marciniak's dissertation (12:6-14).

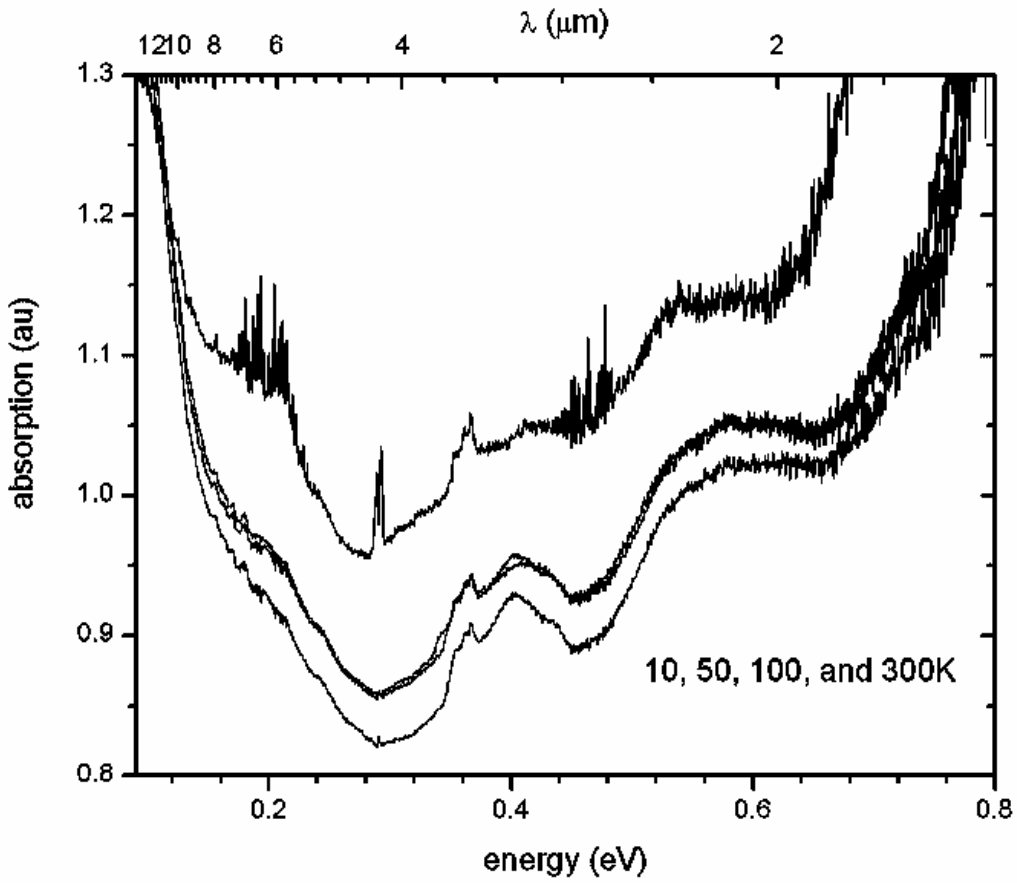

Fig. 4- 8: The absorption curves observed for quantum well sample 94-099 ($InAs_{0.9117}Sb_{0.0883}/In_{0.88}Al_{0.12}As_{0.878}Sb_{0.122}$) at several temperatures.

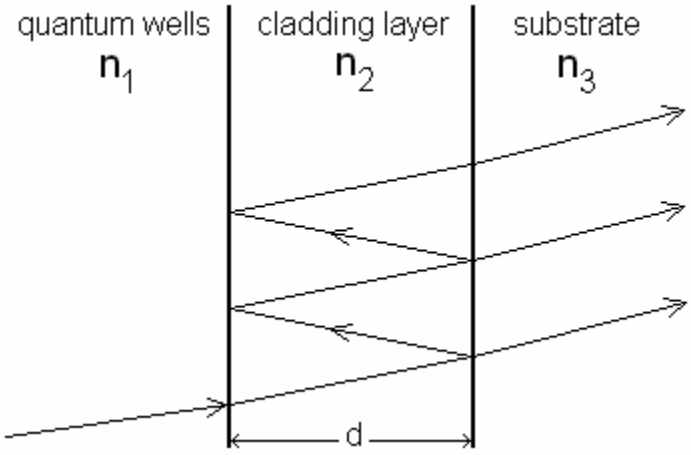

Fig. 4- 9: A depiction of a Fabry-Perot etalon, and how a quantum well would relate.

Able to describe what was observed in the 94-099 quantum well sample, attention was turned to finding the energy transitions within the well. Since the etalon effect ruined any chance of getting these through the curve fitting process, a new method was developed.

Extracting the Energy Transition through Self Referencing

The method used to collect and more clearly display the energy absorption transitions found in the quantum well was self referencing. By subtracting out the absorption curve of the sample at one temperature from that at another temperature, any etalon effects were cancelled out, and the energy transition became clear. The easiest way to understand how this method worked was by drawing out what the expected absorption curves should be, and what subtracting them would result in. This can be seen in Fig. 4-10.

As can be seen from these sketches, the minimum energy transition for any of the samples used could be determined at any temperature. In the bulk samples, the peak

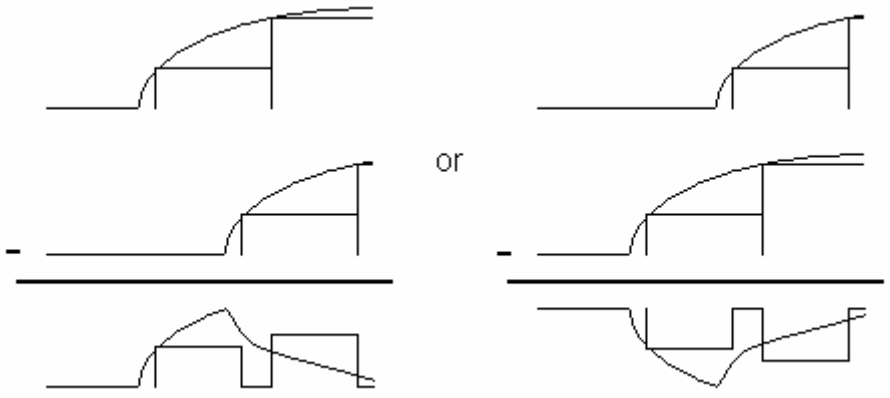

Fig. 4- 10: The expected results of the self referencing method for a bulk semiconductor as well as a quantum well using their respective density of states functions. The left depicts what happens when a lower temperature is used as a reference while a higher temperature reference is shown on the right.

value (whether it was pointing up or down) represented the lower temperature's bandgap energy, while the left starting position before the peak was formed gave the bandgap energy at the higher temperature. Likewise in the quantum well sample, the point right before the peak started forming represented the higher temperature's energy transition while the point right before the peak dropped off gave the lower temperature's energy transition.

With a method developed to determine the desired energy transitions in the quantum wells, this method was first applied to the bulk samples to determine if it provided results comparable to those obtained using the curve fitting routine. Fig. 4-11 shows what the use of self referencing for the bulk samples provided. In order to

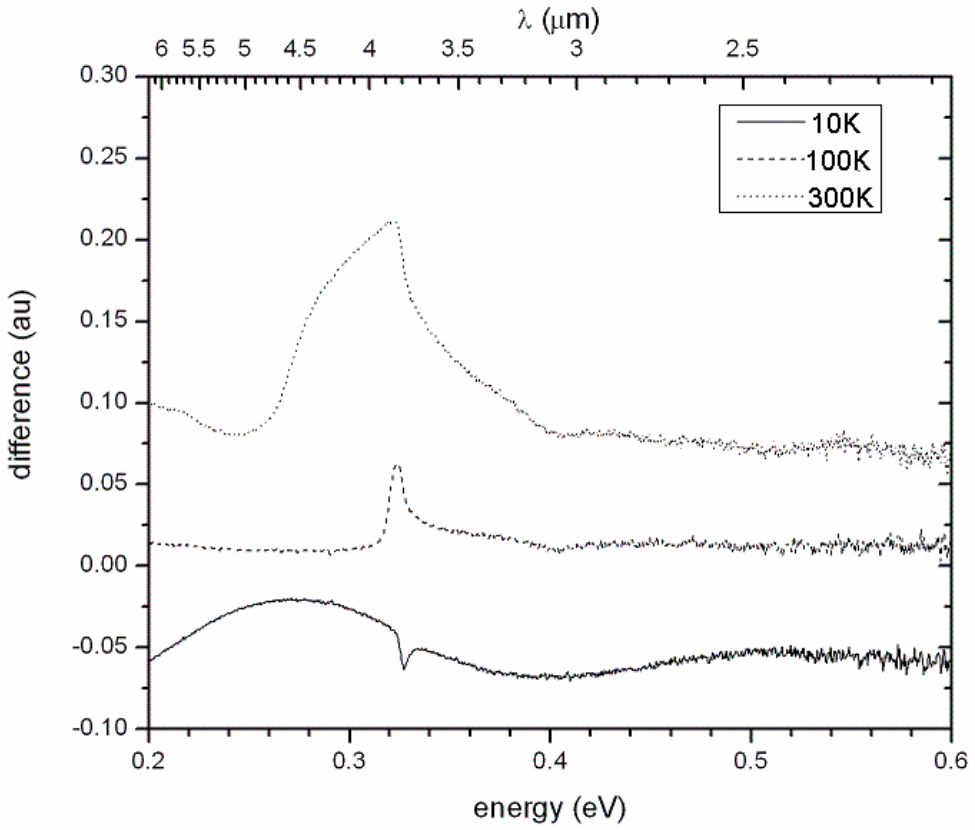

Fig. 4- 11: The absorption curves of bulk 93-045 using its 50K data for self referencing.

eliminate some error in finding the exact points, the absorption spectrum taken at each temperature was used as the reference, and then all the results were averaged. When the results from the self referencing method were compared to those obtained from the curve fitting, it was found that all of the corresponding energies involved were within ±2.5meV. Taking into account the error bars for choosing where the points lay in self referencing (±1.2meV as determined by ones ability to determine the points) and the error bars associated with the curve fitting (±0.5meV as determined by the Origen program), the overall accuracy of this method was determined to be ±1.85meV.

With an acceptable level of accuracy determined for the method, the self referencing method was then applied to the 94-099 quantum well sample (Fig. 4-12).

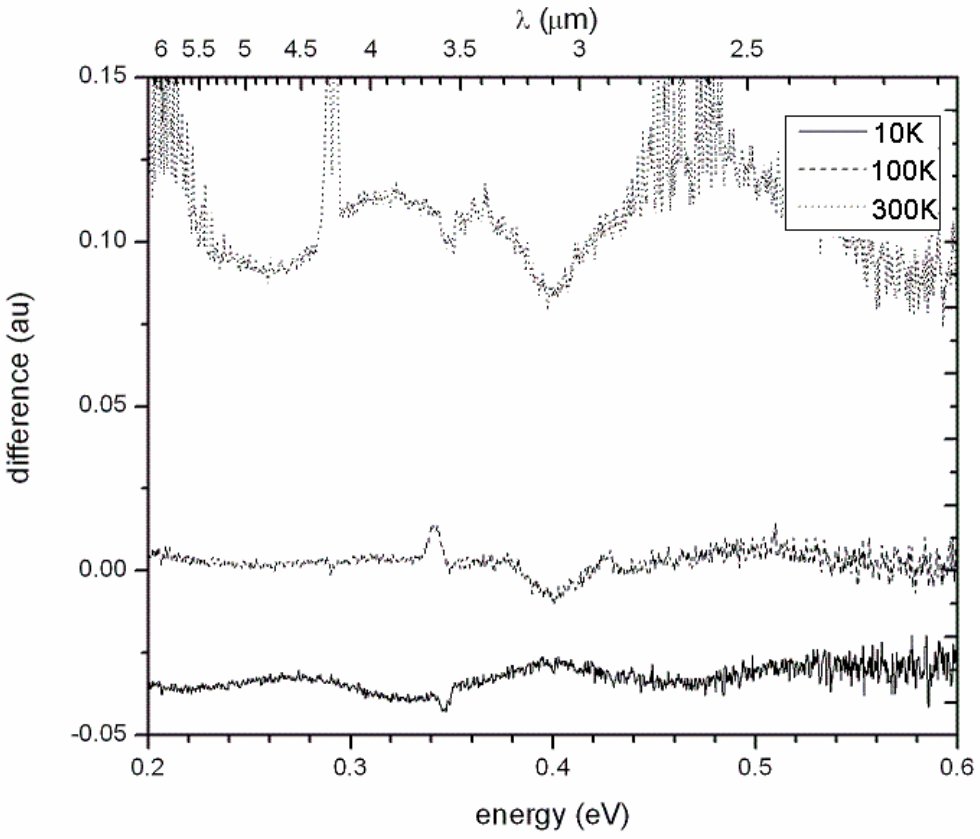

Fig. 4- 12: The absorption curves of quantum well 94-099 using its 50K data for self referencing.

From the results, it can be seen that the etalon effect was erased through this method leaving a clear peak from which to determine the first allowed energy transitions. It was also observed that the peaks are not as parabolic in shape as those of the bulk, which was expected due to the difference in the density of states function.

After analyzing all the samples using the self referencing method, all the necessary energy transitions were obtained for the samples. From here, the trend of the transitions with respect to temperature was examined.

Results and the Varshni Equation

In order to bring all the minimum energy transitions found for each sample together, a Varshni equation was fit to the data. This provided a quick method for determining at what energy the semiconductor would start to absorb at a given sample temperature. Although fitting to the Varshni equation is a widely practiced exercise for bulk materials, there was a question as to whether a Varshni fit would hold merit for a quantum well structure.

Since the Varshni equation describes how the energy transition changes as a result of temperature, exactly how a quantum well is affected by this change must be more closely analyzed. The fact that we are dealing with two (or more) different materials to create a well is what adds a complexity to this problem. The different materials will not necessarily respond in the same way to temperature changes meaning the Varshni equation might need to be modified to account for this difference in order to be truly accurate. This is especially the case for a type II quantum well where the transitions occur across materials. However, for a type I quantum well where the transitions stay within one material, the difference between the reaction of the materials to temperature

should be a minimal effect caused by the slight change in the relationship of the depth of the well. This should not affect the energy transitions found at different temperatures far from what would be seen in a bulk material. For this reason, type I quantum wells should probably display the shape of a Varshni curve and should be able to be fit to one. Of course, whenever a well is modeled by a Varshni equation, the fit only holds for that exact well (same compositions in the barrier and well regions as well as the same well thicknesses).

After fitting a Varshni equation to all of the samples studied experimentally, the average of all the energy transitions found for each sample were entered into Origen and fit to the equation. The results are shown graphically in Fig. 4-13 and the constants from the equation are found in Table 4-1. The results are as expected, that is comparing the quantum well values to those of the well material's bulk counterpart (94-099 to 93-045), it was observed that the transitions from the first heavy hole allowed energy level to the first electron level (hh1-e1) were slightly (20meV) higher in energy than the bandgap transitions of the well alone. It was also found that the first subband transitions of the quantum wells decreased more rapidly with increasing temperature than its corresponding bulk well material. However, this can not be stated as a general case since the quantum well energy levels are reliant on the confinement of the well caused by the barrier material. To be precise, the quantum well decreased more quickly with respect to the compositionally matched bulk material because the barrier's bandgap energy decreases more quickly. The opposite effect would have been true if the barrier decreased less quickly. Lastly, comparing the two bulk samples, it was found that the one with higher antimony composition (94-034) had lower energy transitions.

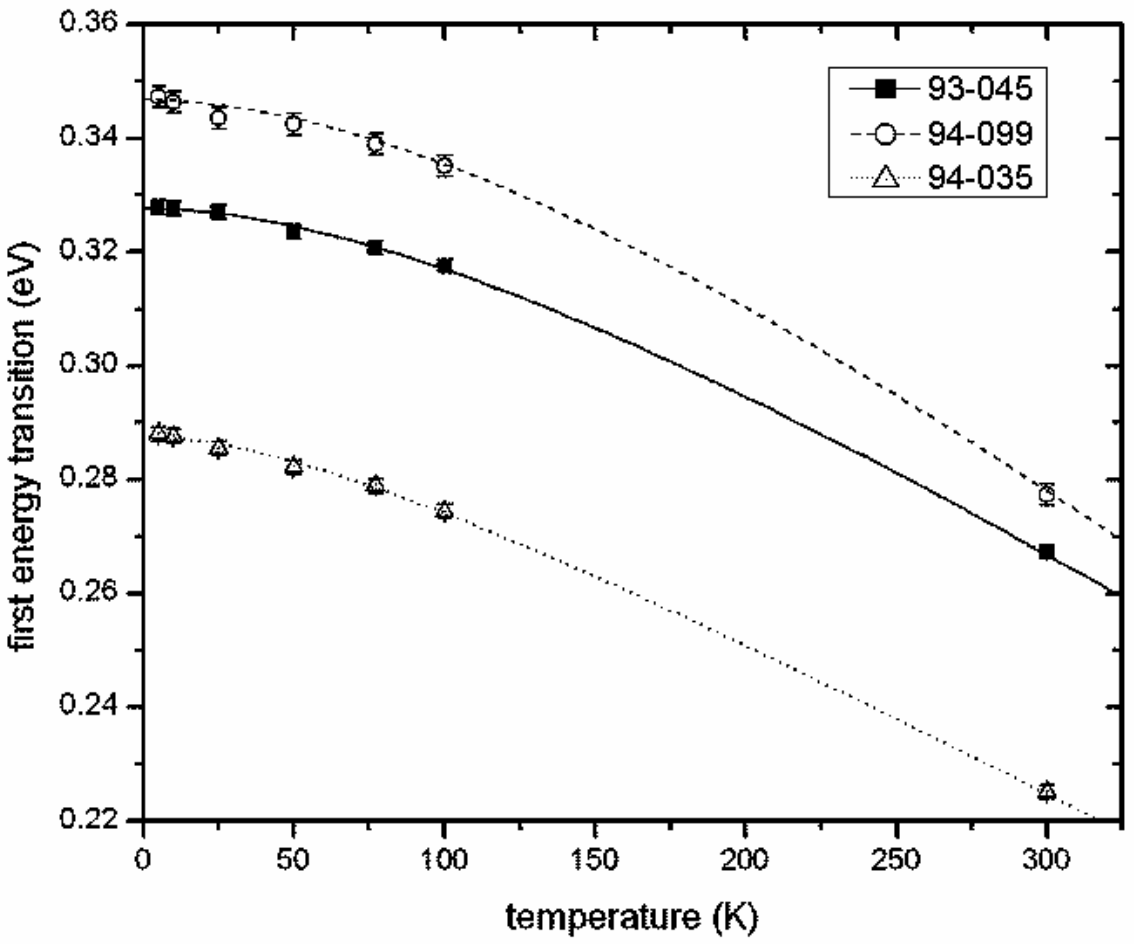

Fig. 4- 13: The results of the absorption experiment fit to a Varshni equation. The bulk materials' (93-045 and 94-035) energies represent the bandgap transition while the quantum well's (94-099) energies represent the first allowed well transition (hh1-e1).

Table 4- 1: The Varshni parameters given to the results of the absorption experiment.

sample #	93-045	94-099	94-035	94-034
description	bulk	quantum well	bulk	quantum well
material composition	$InAs_{0.911}Sb_{0.089}$ ---	well: $InAs_{0.9117}Sb_{0.0883}$ barrier: $In_{0.88}Al_{0.12}As_{0.878}Sb_{0.122}$	$InAs_{0.821}Sb_{0.179}$ ---	--- ---
substrate	GaSb ---	GaSb cladding: $AlAs_{0.085}Sb_{0.915}$	GaSb ---	GaSb ---
α [eV/K]	0.00035	0.00047	0.00029	---
β [K]	246	316	116	---
$E_g(0)$ [eV]	0.3268	0.3467	0.2875	---

Knowing that the trend of the samples was correct, the bulk samples' Varshni parameters were then compared to documented numbers. The two documentations of interest for comparison were those from Michael Marciniak's dissertation (he had done similar experiments with the exact same samples) and those used as parameters in Ram-Mohan's code (which were used for quantum well modeling). As can be seen from these values given in Table 4-2, the theoretical and experimental values both can vary greatly. Since Marciniak had actually done the same experiment on these samples previously, it was expected that the results would be similar to those found by him. The differences in technique between the experimental values and a determination of where the bandedge actually began were most likely the cause for the discrepancies in these values. The differences found with the values from Ram-Mohan can be accounted for by realizing that those values are a linear interpolation (except for $E_g(0)$ which included a bowing parameter) of the values from two compounds that made up the ternary materials. As was seen, this experiment provided parameters which are in some cases close to documented sources but in other cases at variance with values that can be gotten from these materials.

Table 4- 2: A comparison of the Varshni parameters found in this experiment to ones previously documented.

		This Experiment	Marciniak	Ram-Mohan
93-045	α [eV/K]	0.00035	0.00026	0.00028
	β [K]	246	113	100
	$E_g(0)$ [eV]	0.3268	0.3216	0.3285
94-034	α [eV/K]	0.00029	0.00084	0.00028
	β [K]	116	1140	106
	$E_g(0)$ [eV]	0.2875	0.2883	0.2559

Two additional quantum wells were also looked at with absorption however their results were not discussed here since their compositions were not accurately known. Their results can be found in Appendix A.

4.3 Photoluminescence

With an understanding of where the minimum energy transition lies for both the bulk and quantum well samples, the photoluminescence of the samples was more closely examined. The luminescence of the samples was collected using a slit width of 1.00mm, which gave a spectral resolution of 4.44nm. To account for this, the signal was stepped through at 4.00nm increments with a dwell time per increment of 1.00 second. With all the spectrometer parameters determined, the collection of photoluminescence was begun.

A set of temperature and excitation dependent photoluminescence curves for each sample was taken. Examples of spectra for the three samples of interest at a set temperature and several excitation powers can be seen in Fig. 4-14. The spectra given off by each sample were unique in appearance. Before any analysis of these spectra could be carried out, a brief explanation of the reasons they appear as they did will be given.

Differences in Photoluminescence Spectra

As seen in Fig. 4-14, the photoluminescence of sample 93-045 appeared as a single, sharp, narrow spectral line with no distinguishing features. The single peak and lack of distinguishing features merely suggested that the sample was relatively free of impurities. The bandwidth of the photoluminescence spectrum is related to the quality of the sample. A narrower width suggests that more electrons are recombining closer to the bandedge, which signifies a better quality sample.

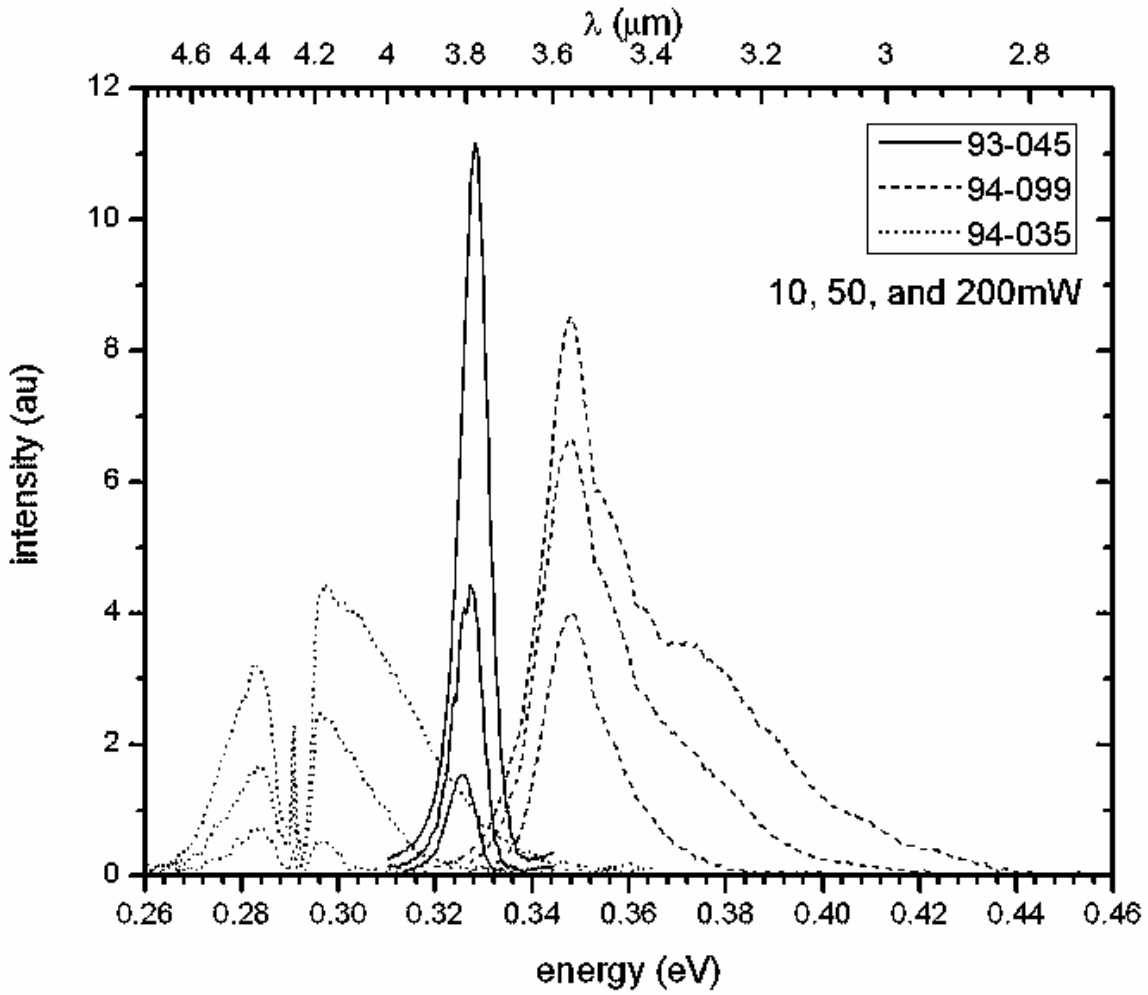

Fig. 4- 14: The photoluminescence of all three samples used in the experiment at 5K and using various excitation powers. Notice how the peak of the curves moves to higher energy with more electrons being pumped up into the conduction band (higher powers).

Moving on to the other bulk sample, it is evident from looking at the figure that 94-034 was of lesser quality than 93-045. Not only are the spectra broader, but as a direct result, they are also less intense (indicated by a noisier signal). The signifying characteristic of this sample is the big drop off in photoluminescence in the middle of the spectra. This was a result of absorption caused by carbon dioxide in the atmosphere in the beam path from the sample to the detector.

The quantum well sample 94-099 also possessed signifying marks of what appeared to be a pushed out high energy tail. This was the result of higher energy transitions occurring in the well. These higher energy transitions also occur as less intense peaks in the photoluminescence spectra, signifying weaker transitions. All of the peaks are so close together that the resolution created by the slit width set for the spectrometer used was not good enough to resolve them, thus creating what appears to be a broad peak. Although the photoluminescence peak was broader than the bulk 93-045 sample, the quantum well sample of 94-099 actually produced a higher signal (which does not correspond to the highest excitation power in the figure due to a different gain used to collect each sample's data), making the quantum well sample the most efficient sample for producing a photoluminescence signal. It was also noticed that the peak of the curve for the quantum well sample did not shift to higher energies with increased excitation power as quickly as those for the bulk samples. The answer to this was found in the density of states equations that defined the low energy tail of the photoluminescence. Since quantum wells provide an energy for many electrons to occupy, the density of states function changes much slower than that of a bulk material. This, in turn, contributed to a slower rate of change of the peak energy of the photoluminescence from the quantum well.

Photoluminescence was also performed on the other quantum well sample used for this experiment. As can be seen in Fig. 4-15, the photoluminescence appears to lie within the energy range that the quantum well transitions were expected to be. However, upon closer examination it was found that this apparent photoluminescence was actually a second order of the gallium antimonide substrate luminescence. The reason that it

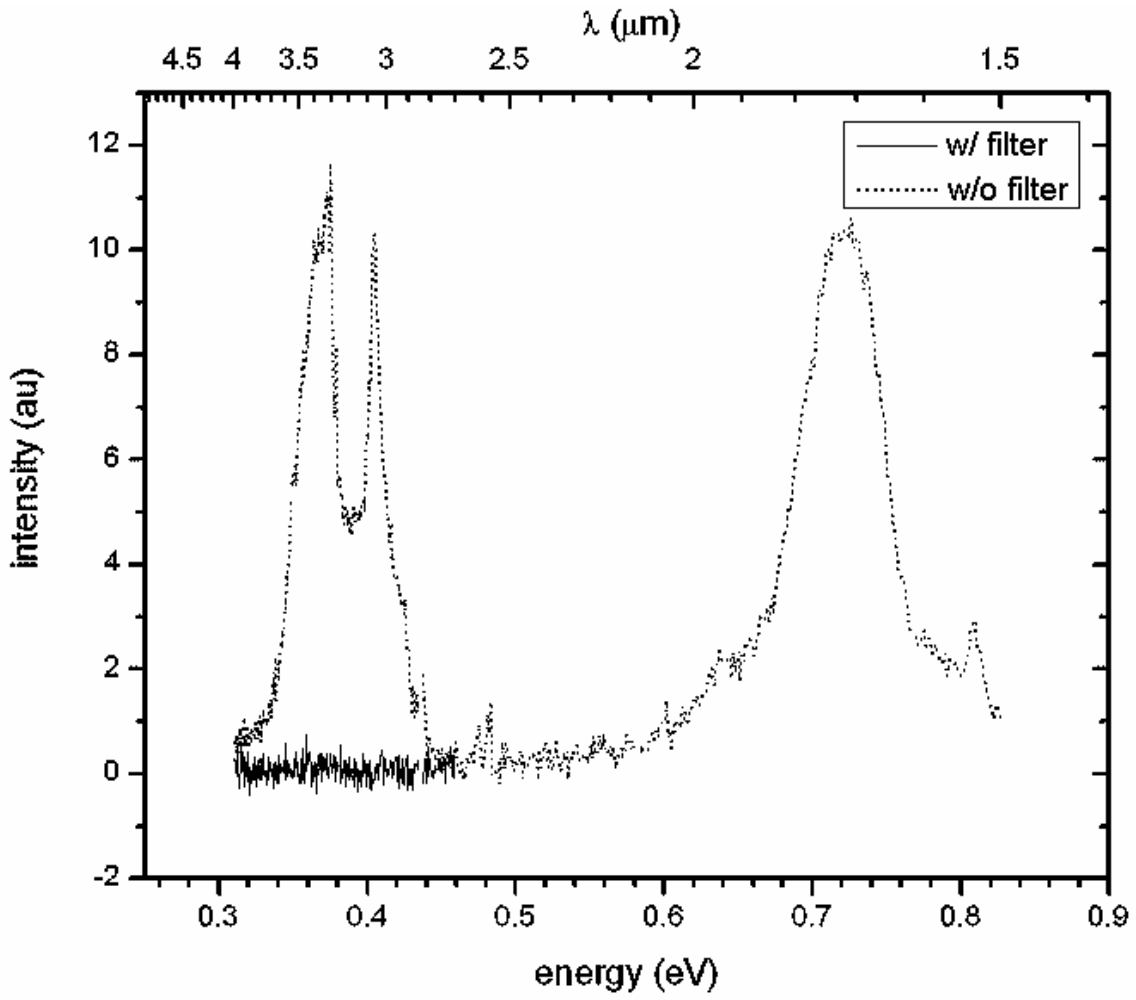

Fig. 4- 15: The photoluminescence of quantum well sample 94-034 at 5K. Without a filter, two distinguishable large peaks appear around the energy that the quantum well should be emitting at (to the left). However, when the W03540-6 OCLI filter used to calibrate the systems was used, it became evident that it was no more than a second order of the gallium antimonide photoluminescence peak (to the right).

appears with such a large intensity as compared to the first order was that the grating in the spectrometer was blazed at 3μm, thus lowering the actual intensity of the first order peak. The absence of peaks in this photoluminescence experiment led to the conclusion that sample 94-034 was just substrate material.

Photoluminescence/Absorption Comparison

The reason for performing the photoluminescence experiment on these samples was to show that the information obtained in the absorption experiment was accurate and consistent. This was done by simply displaying the spectra obtained from each sample on the same plot. The expected result of such a plot would be that the bandedge from the absorption curve would occur inside of the point where the photoluminescence signal starts to rise up to the peak of that curve. A plot indicating this for one of the samples is shown in Fig. 4-16. All three samples exhibited this quality, so the minimum transitional energies found through the absorption experiment were taken to be valid.

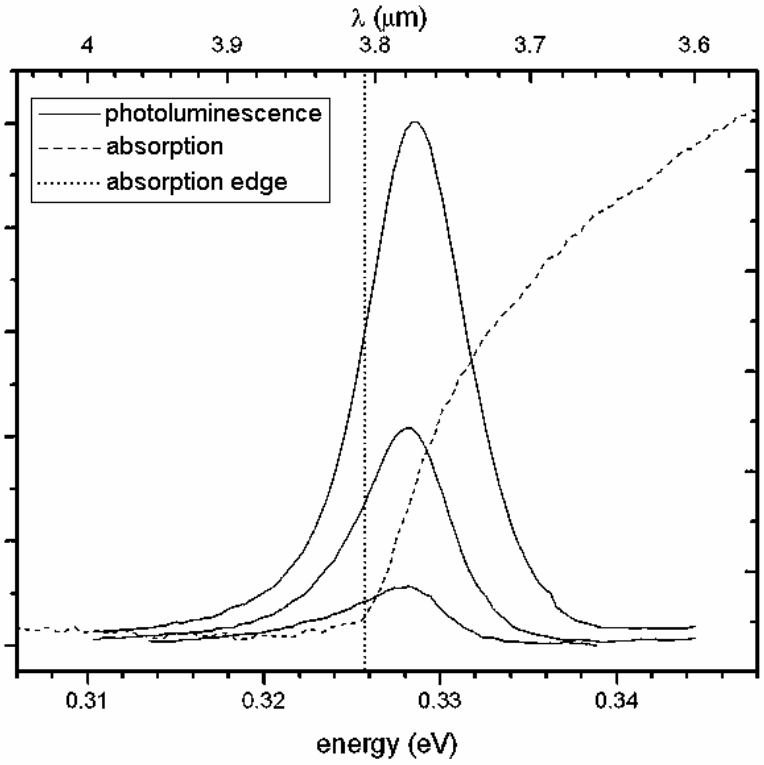

Fig. 4- 16: A comparison of the absorption and photoluminescence spectra for bulk sample 93-045. Notice how the absorption edge lies in-between the beginning of the photoluminescence's tail and peak.

Electron Temperature (T_e) Analysis

With the minimal energies determined to be as accurate as the data permitted, they were then used to help find the electron temperature of the samples at different excitation powers and sample temperatures. It was known that the high energy tail of the spectra could be fit to a decreasing exponential of the form

$$I(E) = y_0 + A\exp[-(E - E_g)/k_B T_e] \qquad [2.6\text{-}2]$$

where y_0 represents the offset of the spectrum and A was inserted as a multiplicative factor. Plotting the high energy side of each spectrum's intensity versus $(E\text{-}E_g)/k_B$, the electron temperature (T_e) was obtained through fitting the data to the above equation using Origen. A sample of the fit obtained is shown in Fig. 4-17.

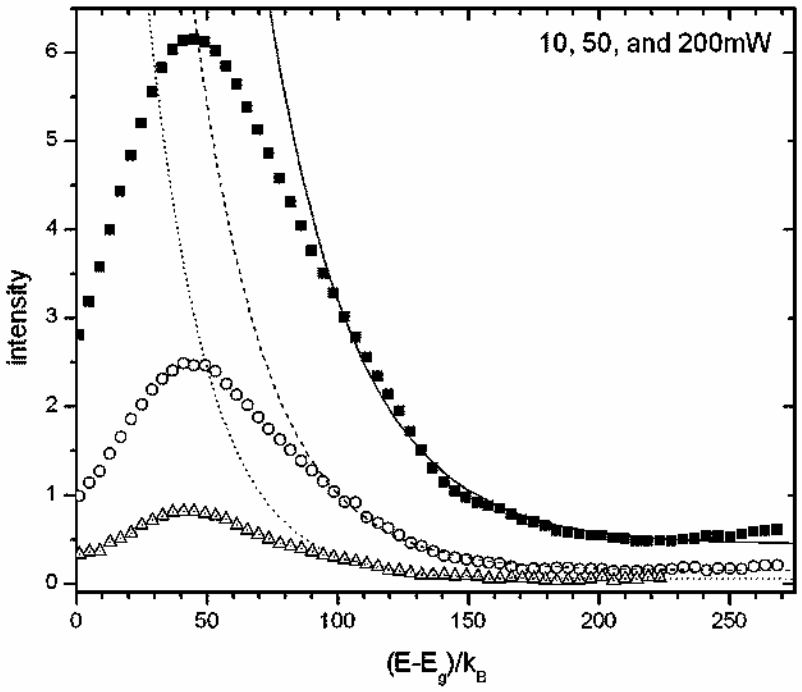

Fig. 4- 17: The electron temperature fit for bulk sample 93-045 for various excitation powers at 25K. Notice how the curves get steeper with lower powers, indicating a drop in T_e.

Since the electron temperature T_e represents the Fermi-Dirac temperature required to maintain the population of the conduction band at a level equivalent to that produced by optical excitation of electrons from the valence band (Fig. 4-18), it was expected that T_e would increase as the excitation power was increased and as the sample temperature was increased. Both of these expectations result from the fact that more electrons will be present in the conduction band, whether they result from optical pumping or an increase in kinetic energy from an increase in sample temperature, respectively. It was also expected that there would be no T_e found lower than the temperature of the sample, simply by definition. These expectations were normally met with the exception that T_e

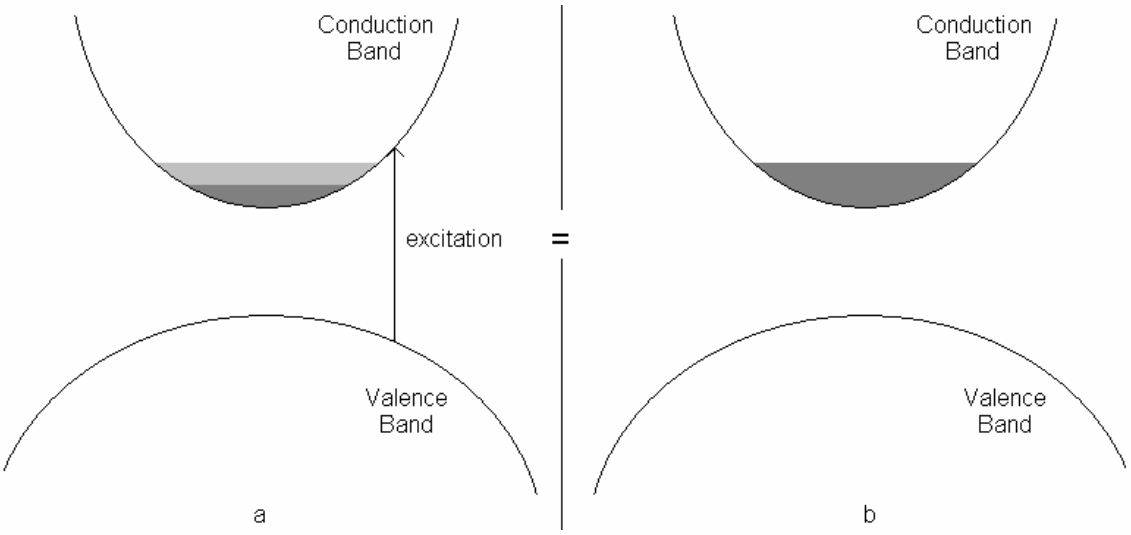

Fig. 4- 18: A diagram depicting how electron temperature is defined. A semiconductor at a temperature above 0K creates a 'pool' of electrons at the bottom of the conduction band (represented by the dark shading). The higher the temperature gets, the larger the pool becomes ($T_b > T_a$). When the semiconductor is excited through pumping, excess electrons are placed into the conduction band (shown by the lighter shading) creating a larger pool. This larger pool, as seen by the conduction band in the material, is the same as if the temperature of the sample was higher (except not in thermal equilibrium). T_e is defined as what the apparent temperature in the conduction band is with external pumping (T_e of a = T_b).

did not always increase with sample temperature. These results are shown in Table 4-3.

With the exception of a couple outliers that can be negated for their spectra's poor signal quality, two of the expected trends were met using this method of analysis. Since two expected trends were met, the method was most likely not the cause for not observing the last trend. Upon closer inspection, the two bulk samples seem to follow the increasing T_e trend with increasing sample temperature (again, with the outliers negated

Table 4- 3: The determined electron temperatures for the three samples given in Kelvin.

sample 93-045	Temperature					
excitation power	5K	10K	25K	50K	77K	100K
200mW	24.178	29.926	33.283	---	---	---
100mW	23.179	26.328	28.914	---	---	---
50mW	20.084	23.411	27.703	---	---	---
25mW	18.878	23.411	25.835	---	---	---
10mW	16.490	20.262	22.596	---	---	---
5mW	25.253	19.835	20.764	---	---	---

sample 94-099	Temperature					
excitation power	5K	10K	25K	50K	77K	100K
200mW	88.442	90.655	76.960	123.134	179.111	206.006
100mW	66.138	60.991	66.742	101.634	166.721	164.448
50mW	54.514	52.649	51.656	85.499	150.928	127.238
25mW	41.943	42.372	49.811	79.978	119.336	---
10mW	34.609	35.208	41.290	70.949	107.628	---
5mW	33.025	29.265	40.731	61.157	---	---

sample 94-035	Temperature					
excitation power	5K	10K	25K	50K	77K	100K
200mW	165.610	140.482	150.296	214.317	280.798	---
100mW	143.194	114.931	139.807	145.494	216.111	---
50mW	84.298	85.574	108.866	124.282	---	---
25mW	76.334	77.611	99.342	---	---	---
10mW	33.821	---	---	---	---	---
5mW	---	---	---	---	---	---

The numbers should decrease going down the column and increase going across the rows. Also, no T_e should be found to be lower than the temperature at which it was obtained.

due to poor signal). This leaves the quantum well as the only questionable sample. Upon doing the analysis of the 94-099 sample, it was believed that all of the energy transitions would result in giving the same electron temperature. With this in mind, only the data from the transition tail of the highest energy transition was included in the curve fitting. Using this experimental process, the error was believed to be caused by an inability to distinguish where the highest energy transition peak began. This was due to the fact that the spectrum represented a mixing of the energy transition peaks, thus throwing off the T_e description of the quantum well.

LO Phonon Cooling Range

A characteristic of semiconductors that can be determined now that the electron temperature is known is the range at which the longitudinal optical (LO) phonon dominates the cooling process of the electrons in the conduction band. The LO phonon is the most efficient way to cool excited electrons in a semiconductor and has the ability to interact with electro-optical radiation. For these reasons, the range at which it dominates the cooling is a desired property to know for application.

In order to determine this information, one first needs to know how the electron temperature is related to the excitation power. Since the carrier generation rate is proportional to the energy put into the semiconductor, it is expected that the inverse of T_e will depend logarithmically on the laser power (10:136) as

$$\frac{1}{T_e} \sim \frac{-k_B \log P_{laser}}{E \log e} \qquad [4.3\text{-}1]$$

where P_{laser} is the laser power, E is the energy put into the semiconductor, and *e* is Euler's number. By inserting the expected energy of the LO phonon in as E, one obtains a formula for T_e^{-1} vs. P_{laser} for the LO phonon. By plotting this relationship in for the

various T_e^{-1} values found experimentally, one can determine from the intersection of the two curves the range of electron temperatures over which the LO phonon dominates the cooling process. As an example, Fig. 4-19 extracted from S.A. Lyon's article helps to clarify this point.

The figure shows that in order to create a better representation of the semiconductor, the excitation power is given in terms of its intensity onto the sample to accommodate for differences in excitation spot sizes. For this experiment, a pinhole was

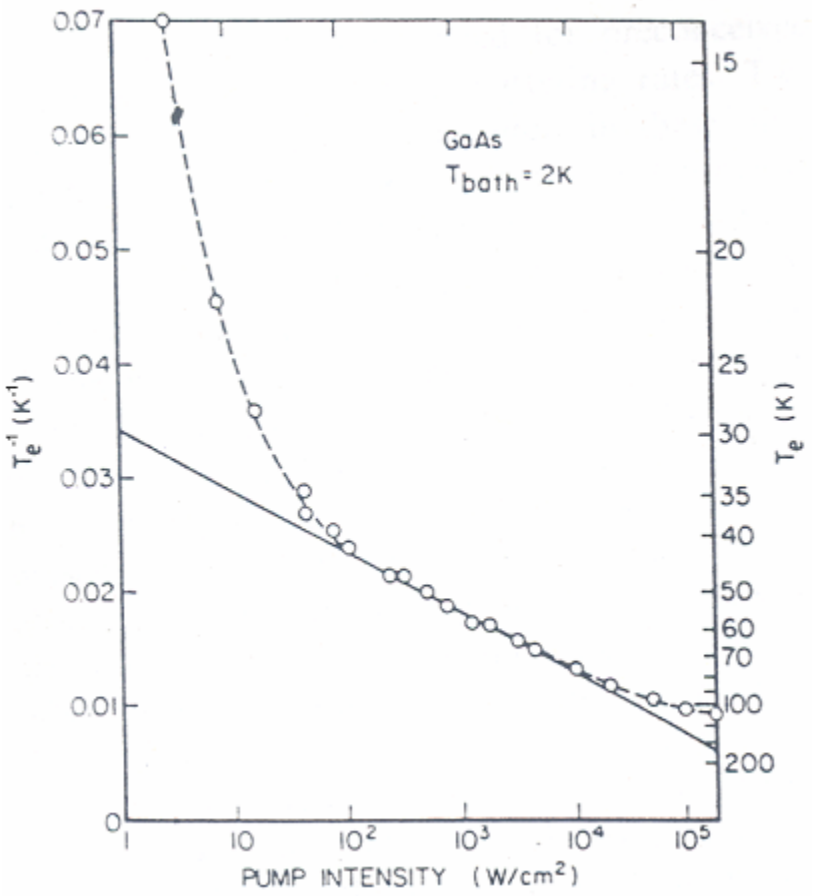

Fig. 4- 19: The inverse electron temperature given for GaAs at 2K in terms of pump intensity (log scale). The solid line represents the LO phonon energy of GaAs with a slope of $-k_B/E_{LO}$. When the data points lie on the line created by the LO phonon energy, the optical phonon is said to dominate the cooling processes of the samples. (10:137)

used to measure the size of the laser beam as it struck the sample. It was found that the circular beam had a diameter of 0.5mm, giving an area of 0.00196cm^2 for which the delivered power was spread out onto the samples. It is also apparent that the larger the range of optical powers available, the greater one's ability to find the overlap range where the LO phonon cooling dominates. Unfortunately, the titanium-sapphire laser used in this experiment could only provide a maximum excitation power of 200mW. This was only sufficient to allow for an analysis of the incipient range over which the LO phonon cooling occurred for the tested samples.

There are two ways to determine the LO phonon energy for these samples: one experimental and one computational. The experimental technique involves looking more closely at the photoluminescence given by the sample and determining the energy difference between the main photoluminescence peaks and their respective phonon replicas. This method was used by Michael Marciniak and can be found in his dissertation (12:7-23). The theoretical method used for this experiment assumed the known optical phonon energies of the two compounds that made up the sample. These energies were then linearly interpolated to find the LO phonon energy of the known composition of the sample. In order to determine the accuracy of the linear interpolation, the LO phonon energy obtained was compared with that obtained from the experimental method. For the bulk 93-045 sample, the LO phonon linear interpolation provided a LO phonon energy of 29.1meV (11:137,145), while Marciniak measured the phonon replica to be 28.6meV away from the main peak. With a difference of 1.9% between the calculated and experimental optical phonon energy, the computational values were assumed to be sufficiently accurate.

Using these expected phonon energies for the samples, the phonon energy curve was computed from equation 4.3-1 and plotted to fit the inverse electron temperatures found in the experiment. A look at some of the resulting graphs can be seen in Fig. 4-20. As was expected, the start of the optical phonon cooling range decreased with pump intensity as the temperature increased. This reflects the fact that at higher temperatures, the electrons already possess higher thermal energy, making it easier to get them into the LO phonon cooling range. This held true for all of the samples, even quantum well sample 94-099 whose electron temperatures were in question. Since the excitation

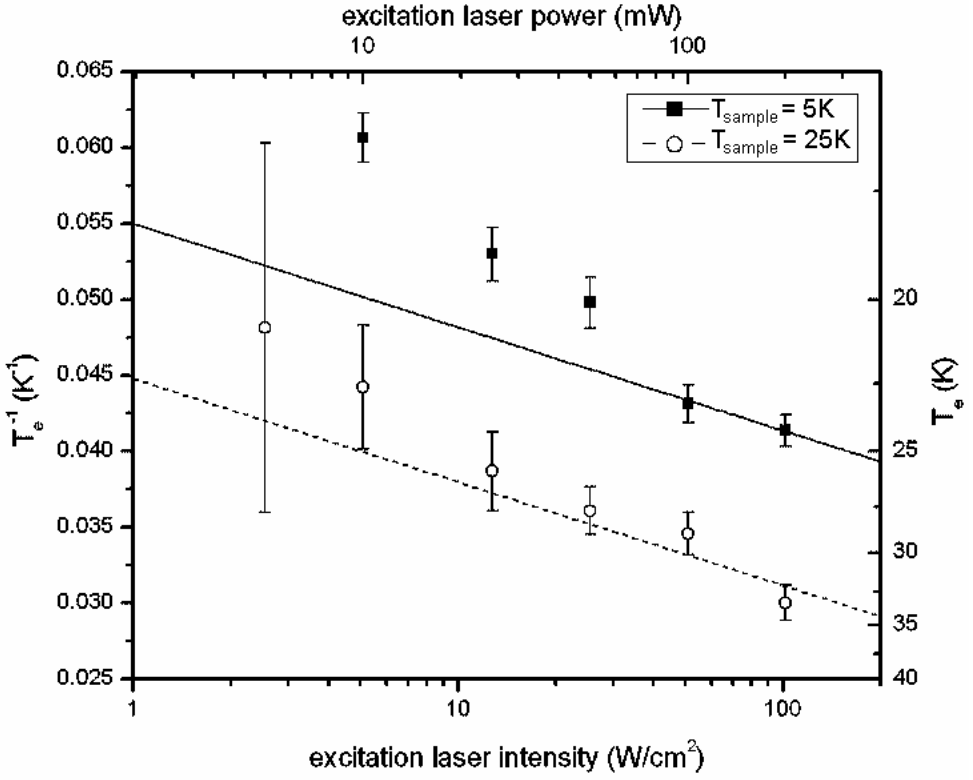

Fig. 4- 20: The plots determining the LO phonon cooling domination range for bulk sample 93-045 at various temperature. The lines represent the 29.1meV LO phonon for $InAs_{0.911}Sb_{0.089}$.

powers at which the samples were explored with were few and not very close together, an approximation of the pump intensity ranges where the LO phonon dominated the cooling process for the samples was visually made from the graphs and can be found in Table 4-4.

Comparing the starting ranges for the quantum well and its compositionally matched bulk sample, it is observed that the LO ranges start at higher pump intensities for the quantum well. The reason can be explained by considering the density of states function. Since there are so many states found at the same energy in the quantum well, more electrons need to be pumped into the well to get to the higher energy needed for optical phonon cooling transitions.

Table 4- 4: The approximate starting points of the LO phonon cooling range.

		93-045	94-099	94-035
T_{sample}	material	$InAs_{0.911}Sb_{0.089}$	$InAs_{0.9117}Sb_{0.0883}$ $In_{0.88}Al_{0.12}As_{0.878}Sb_{0.122}$	$InAs_{0.821}Sb_{0.179}$
---	calc. E_{LO}	29.1meV	29.1meV / 31.4meV	28.7meV
5K	LO phonon cooling starts domination in this range	50 W/cm^2	I_{pump}>101 W/cm^2	50 W/cm^2
10K		25 W/cm^2	I_{pump}>101 W/cm^2	25 W/cm^2
25K		7 W/cm^2	50 W/cm^2	15 W/cm^2
50K		---	20 W/cm^2	---
77K		---	12 W/cm^2	---
100K		---	---	---

4.4 Quantum Well Modeling

Having the experimental characteristics of the samples, Ram-Mohan's femb program was run to see if its theoretical calculations matched what was observed for the quantum wells. To do this, an input file was created for the sample (shown in Appendix

B) assuming that the barriers were large enough to confine the wells. With the confinement from the barriers, each well in the ten-well system should act as a single quantum well, and so they are treated as such in the modeling. By determining the energies found for a single quantum well, the program predicts what the energies are for all ten wells found in each sample.

After running the femb code using the material characteristics already given by Ram-Mohan in the femparm.inp file, it was determined that some of the characteristics for the needed compounds were incorrect. The main problem with the original parameters was that they did not result in bandgap energies that coincided with those of the bulk samples. In order to fix this error, the method used by Michael Marciniak in his dissertation was employed, resulting in different bandgap energies and a different bowing parameter for the indium-arsenide-antimonide ternary compound; i.e. the original bowing parameter of -0.67 eV was replaced with a more accurate -0.858eV determined by Marciniak (12:6-30). Since this parameter was embedded in the femb code and could not be changed in the input files, a new femparm.inp file was created with all of the parameters of the well and barrier compositions found in the samples already calculated out; this file can be found in Appendix C. In order to be as up to date as possible with the other parameters found in the file, the most recent published values of the material parameters (18:5826) were used to update the file on the compounds involved. With the original input files totally updated, the modeling of the quantum well samples was carried out. Since only the 94-099 quantum well sample produced relevant output from absorption and photoluminescence, it will be the only one discussed in this section.

The first modeling that took place was to determine what the quantum well energies looked like spatially. This was done by simply recording the band offsets computed by the program for each material present in the sample and then referencing them to each other. The resulting diagram depicting the 94-099 quantum well sample is shown in Fig. 4-21. Notice that the modeling done shows the heavy- and light-hole band maxima to be degenerate.

With a clearer picture as to at what the quantum well looked like, the femb code was run to determine where the allowed energy levels would lie within the well region. Since the purpose of modeling in this experiment was to check the accuracy of the Ram-Mohan code in compared to experimental values, only the first few energy transitions were of interest. For this reason, only the energy levels found in the conduction and heavy- and light-hole bands were modeled. When run, the program generated the eigen values in this range. The resulting positions of the levels with respect to the conduction and valence band levels and at one temperature are seen numerically in Table 4-5 and graphically in Fig. 4-22.

By comparing the values for the first energy transition from the model to those found in the absorption experiment, the validity of the model could be tested. This comparison for all temperatures tested is given in Table 4-6. As is seen, the difference between the model and the experimental results remains rather constant (especially when the experimental error of ±1.85meV was factored in). This error may result from a number of sources not included in the code or conversely, assumptions made in the code which did not fit the application. The first possible reason could be all of the linear

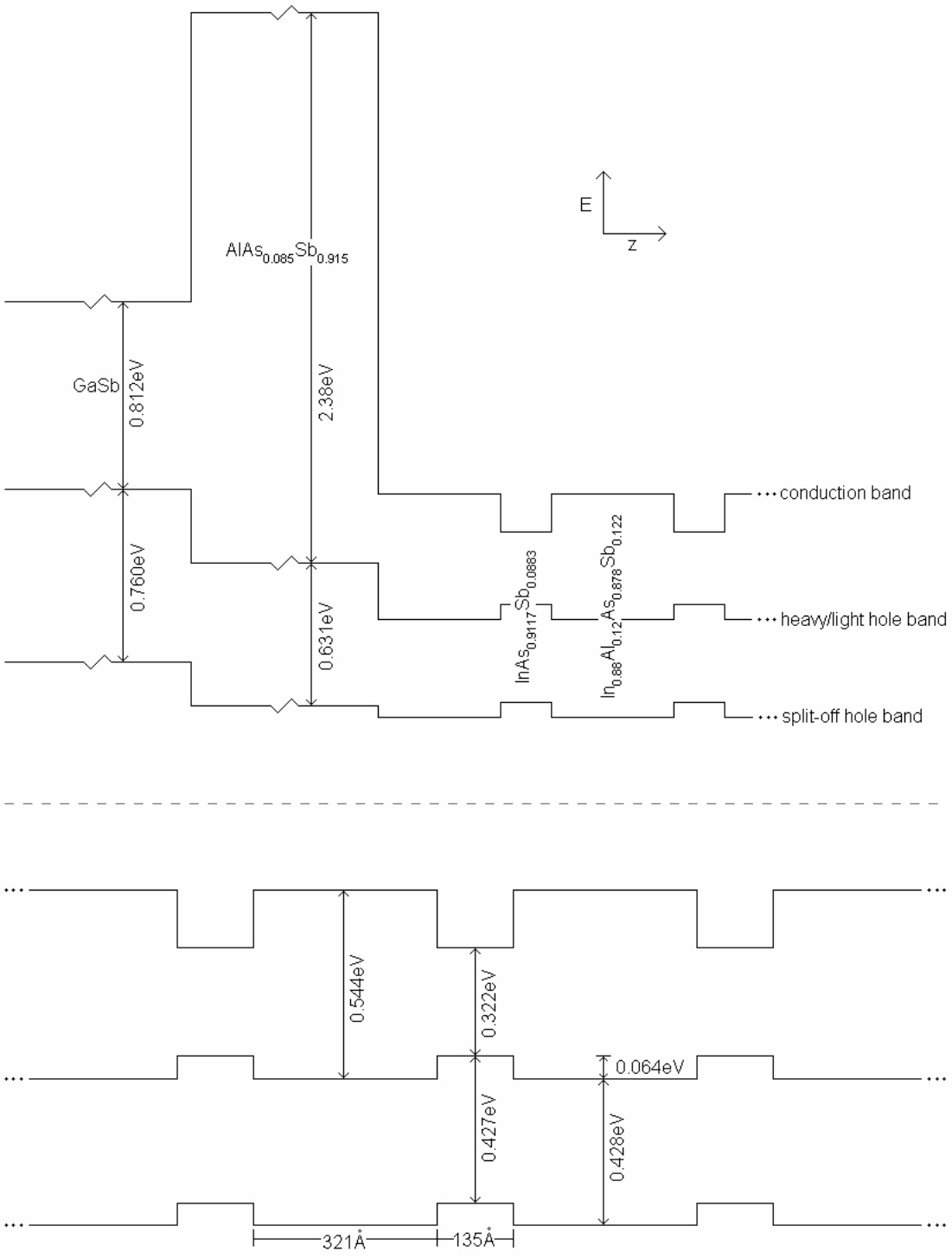

Fig. 4- 21: How the energy offsets of the 94-099 quantum well sample are expected to look in real-space at 0K. The top picture shows the structure as a whole, including the cladding and substrate layers. The bottom picture provides a closer look at the quantum wells formed in the sample.

Table 4- 5: The allowed energy levels found through Ram-Mohan's code for quantum well 94-099.

T = 5K	bulk barrier	bulk well
cb energy (eV)	0.5444	0.3842
hh energy (eV)	0	0.0641
lh energy (eV)	0	0.0641

allowed energy level label	allowed energy level position (eV)
e2	0.522
e1	0.426
hh1	0.0597
hh2	0.0469
lh1	0.0398
hh3	0.0264
hh4	0.0024

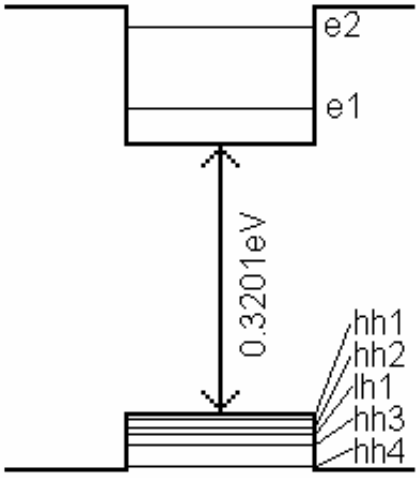

Fig. 4- 22: The pictorial equivalence of Table 4-5, drawn to scale.

Table 4- 6: The difference between the first allowed transition energy in quantum well sample 94-099 from the absorption experiment and through modeling using the femb code.

T	e1-hh1 transition through absorption (eV)	e1-hh1 transition through modeling (eV)	difference
5K	0.3472	0.3663	0.0191
10K	0.3464	0.3661	0.0197
25K	0.3435	0.3652	0.0217
50K	0.3424	0.3626	0.0202
77K	0.3389	0.3588	0.0199
100K	0.3351	0.3549	0.0198

interpolation that takes place in order to determine the parameters for each material in the quantum well; perhaps a linear interpolation does not accurately describe all of these parameters. Another reason could be that the model of a quantum well used in the program was generic. Finally, the 94-099 sample could obviously not have had degenerate heavy- and light-hole bands, meaning strain would need to be included into the modeling process (which the code does allow for but was not used). At any rate, if simply shifting the predicted energies from Ram-Mohan's code allows the modeled energies to match the experimentally measured values, it can be concluded that the code did indeed provide a good method of modeling the expected allowed transitions found in the quantum well. This conclusion is also supported by comparing the predicted energies to the absorption and photoluminescence spectra (Fig. 4-23). When the modeled energy subbands are shifted by the difference between the experimental and theoretical first transitional energy, the second and third allowed transitions appear to be more clearly discernable in the photoluminescence spectrum.

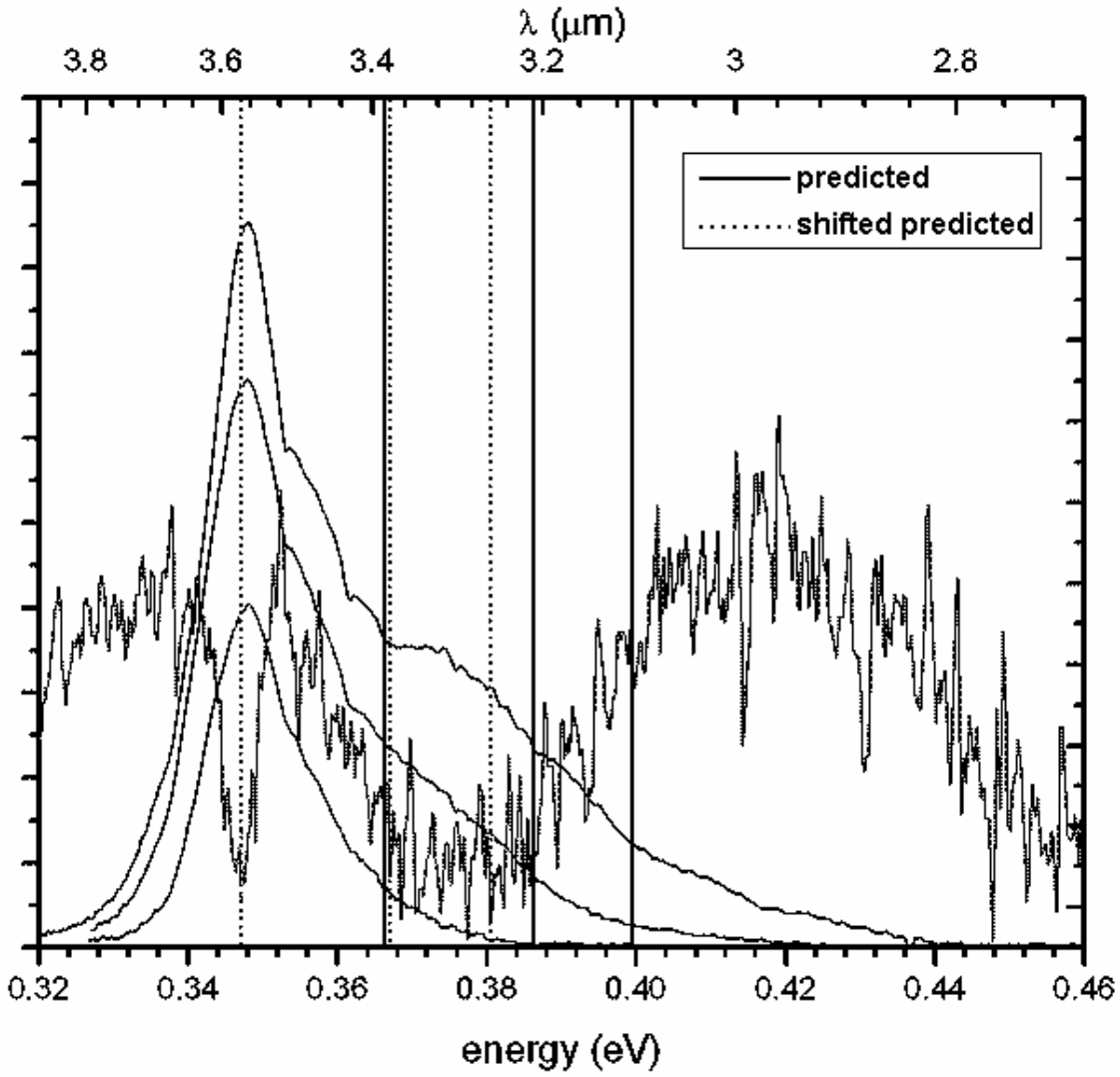

Fig. 4- 23: A plot showing where the first three predicted energies (starting at the lowest energy: e1-hh1, e1-lh1, and e1-hh3) lie along the self referenced absorption (reference of 50K) and photoluminescence spectra at 5K. The solid lines represent what Ram-Mohan's code predicted for the subband energy transitions. The dotted lines give the predicted energies shifted by the difference between the experimental and modeled e1-hh1 transition (the lowest energy dotted line lies where the first transition was found experimentally).

5. Conclusions and Recommendations

This chapter provides the conclusions that can be drawn from the experiments performed. It then goes on to give suggestions for future work.

Conclusions

In order to gain greater knowledge as to methods of producing indium arsenide-antimonide quantum wells for military application, this experiment sought to characterize two such quantum well samples and to compare the results with those from their compositionally matched bulk material. The main goal of the research was to document the differences that could be observed in the results of optical characterization of the two. This experiment also tested the reliability of Ram Mohan's finite element method computer program (femb) in generating the allowed energy levels found within the quantum well by comparing them to the experimental transitions found experimentally. Unfortunately, since one of the quantum well samples was found to be missing its quantum well layers, leaving only a substrate, only one set of compositionally matched samples were studied. However, this was enough to see several optical characteristic changes that the creation of a quantum well brings as well as a first look at the accuracy of the computational model.

The absorption study of the samples gave results that showed how the first allowed energy transition of the semiconductors was affected by temperature. Although quantum wells cannot be totally defined by a Varshni equation, it was determined that type I wells followed the shape of this function. After fitting data from all the samples to the Varsni equation, the first transitional energy for the quantum well was found to be just slightly higher in energy than that for its corresponding bulk sample. This was

expected from the quantum effects created by the confinement of the well. It was also found that the first subband transition in the well decreased more rapidly with increasing temperature than its corresponding bulk material. This difference between the behavior of bulk and quantum well materials as a function of temperature was due to the barrier's larger decrease in bandgap. It should be expected that the subband energy transitions in the quantum well will either decrease more slowly or more rapidly than those in the matching bulk material; whether this will be an increase or decrease depends on the effect that temperature has on the barrier material with respect to the well material.

Another characteristic found in the quantum wells through the absorption measurements was that they all exhibited the etalon effect. This, however, was not caused by the quantum well structure, but rather from the cladding layer which was added to the sample. By adding this extra layer, an additional refractive index is added to the stack of materials making up the sample. The extra interface that the light has to travel through creates an etalon effect within the sample. This would hold true for any sample grown onto a substrate that has a cladding layer added to it, bulk or quantum well. Although the cladding layer reduces the strain of the bands for the material of interest, it also distorts the expected absorption signal.

The photoluminescence study of the samples provided more expected results for the compositionally matched samples. It was observed that at a given temperature, the peak intensity value of the quantum well sample did not shift as quickly to lower energies with decreasing excitation as it did for the bulk samples. This was expected from the fact that the density of states function, which defines the lower energy side of the photoluminescence curve, changes less rapidly for a quantum well than for the bulk. It

was also observed that the quantum well sample produced a larger intensity signal with a broader peak than the matched bulk sample. With a spectral resolution not small enough to resolve photoluminescence peaks that were close together, the spectrum of the quantum well samples consisted of a series of overlapping spectral peaks associated with the allowed subband transitions. This overlap caused the signal to appear to have a broad high energy tail which would be expected for quantum well samples.

Photoluminescence also provided an opportunity to study the electron temperatures of the samples. Although there was no apparent relationship to be seen between the quantum well and its corresponding bulk sample as far as T_e was concerned, when the dominant range for the longitudinal optical phonon cooling process was analyzed, an interesting characteristic surfaced. It appears that it takes a larger amount of excitation intensity to have the LO phonon dominate the cooling for the quantum well than it does for the bulk. The difference in the density of states between the samples is the reason. With more states found at the same energy for a quantum well sample, more electrons need to be pumped into the well to get to the higher energies needed for optical phonon cooling.

Predicting the energy subband transitions between the states found in the quantum well was the last study carried out in this experiment. Using Ram-Mohan's finite element method program that implemented the 8-band k·P model, the predicted energies that it produced turned out high as compared to the experimental findings. However, it was found that the difference between the experimental first allowed transition and the one predicted by the code was approximately always the same across the different temperatures. This meant that there was a shift in energy that needed to be added to the

values calculated from the code in order to get an accurate prediction. This need for this factor probably came from the fact that the code was run with generic parameters for the semiconductors found in the well. For example, all of the parameters used in the calculation were found by linearly interpolation (except for the bandgap energy) and the assumption was made that there was no strain in the structure. In spite of these possible misrepresentations, and considering the complexity of the calculations involved to determine it is edifying that the predicted values are simply shifted from those needed to match the experimental values.. Thus, as long as the shift can be found experimentally, Ram-Mohan's femb code appears to be an effective predictor of the subband energies produced within a quantum well semiconductor.

Recommendations

Upon completion of this experiment, it was realized that there was room for improvement in the both the procedures and the equipment used. The following are some suggestions that might be considered for similar future experiments.

In addition to the standard absorption measurements described in this experiment, future study should also include a closer look at the etalon effect. Since the constructive and destructive interference created by an etalon depends on how the light exits the sample, it should be possible to move this interference pattern by simply rotating the sample. With the rotation in tact, the exiting light rays will interfere in a different manner, causing a shift in the peaks and valleys observed. This would help to establish that this effect is indeed caused by an etalon created in the samples with cladding layers.

A couple of additions and changes of equipment would help to improve the photoluminescence experiment. First, an excitation laser that lases at lower energies than

the bandgap of the substrate is needed. This would eliminate all effects caused by the substrate so that it will not interfere with the desired signal. Also, this laser should be capable of producing higher powers (into the watt range). This would allow for a larger range of electron temperatures to be observed and, in turn, would help to define a better range over which optical phonon cooling dominates. Lastly, the path leading from the sample to the detector should be purged with nitrogen gas; if this were done, a cleaner overall signal will be achieved by eliminating the unwanted atmospheric absorption.

In order to clean up the error found in Ram-Mohan's finite element method modeling code, the parameters that the code employs should be investigated. These include adding strain to the model and changing around the material parameters to match more closely to what is seen experimentally. For this reason, the most up to date parameters should always be checked out and used for both the well and barrier materials found in the quantum wells being tested. Obviously, it would also be valuable to have more than one quantum well sample with which to test the model.

The next step to be taken in studying the quantum well dispersion relations of indium arsenide-antimonide would be to do a similar experiment as this one with a set of quantum well samples that are completely the same except for the $InAs_{1-x}Sb_x$ well compositions, which would range in x values of 0 to 1. Along with the quantum well samples and a set of compositionally matched bulk well materials, a compositional match for the barrier material used in all the quantum wells should also be looked at. This would give a more complete picture of how the materials creating the quantum well act when apart and when brought together to create the confined well. It also would provide a more complete picture of the compositional dependence of $InAs_{1-x}Sb_x$ for bulk

semiconductors and how those compositions react when placed into the same quantum well confinement. By including the barrier material's bulk equivalent into the experiment, some of the parameters that are inserted into the modeling code can be experimentally determined instead of having to linearly interpolate everything for just an approximation of these parameters. This would guarantee accurate parameters to the quantum wells being modeled, and a more precise basis for determining if Ram-Mohan's modeling code is accurate.

Appendix A: Absorption Measurements of Two Additional Quantum Wells

Along with the absorption measurements of the four primary samples of this experiment, two additional quantum wells samples' first energy transitions were characterized. These samples were of interest because the materials making up of the barrier and wells were similar to the 94-099 sample; the only problem was that the compositional make up was not known. What was known about the samples can be seen in table A-1.

Table A- 1: The properties that are known of the two additional quantum wells tested.

Sample	94-083	94-084
description	Type I: 10 QW	Type I: 10 QW
well material	InAsSb	InAsSb
barrier material	InAlAsSb	InAlAsSb
cladding layer	AlAsSb	AlAsSb
substrate	GaSb	GaSb
well thickness	150Å	150Å
barrier thickness	300Å	300Å

The absorption spectra from these quantum wells mimicked those from the 94-099 sample, giving more support to the etalon effect. Using the self referencing method to extract the desired energies and assuming that the barrier material composition was close to that 94-099, some general remarks could be said about the new wells' compositions. Looking at the results in Fig. A-1, since both of the additional quantum

wells lie beneath the curve of 94-099, it was determined that both contained a higher composition of indium antimonide in their well regions than the 8.83% found in 94-099. Through the same argument, sample 94-083 has the highest concentration of indium antimonide of the three. Comparing the energy difference between the energy levels of the 94-099 quantum well sample and the corresponding well bulk sample of 93-045 to the difference between the energies of the 94-083 and 94-084 samples and their expected bulk sample energies, a guess was made to what the actual compositions were. This was

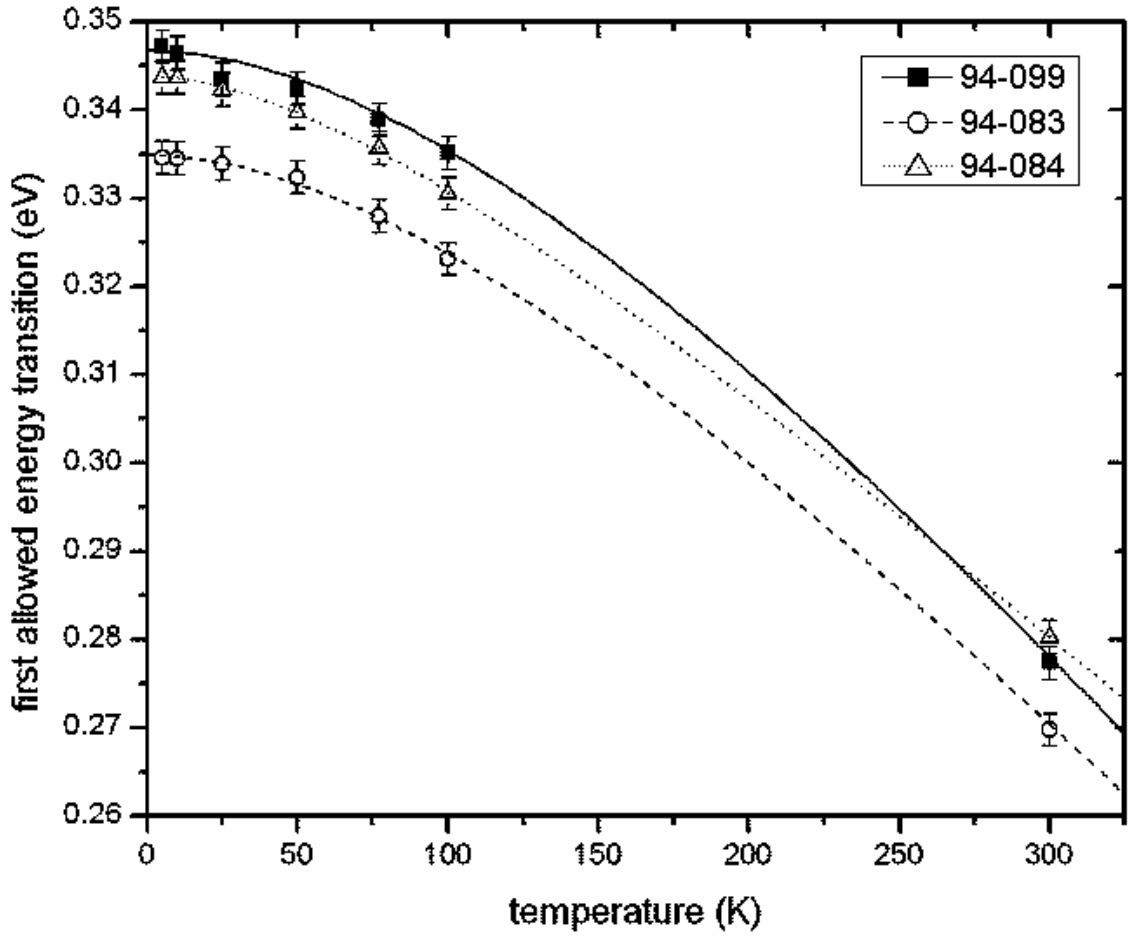

Fig. A- 1: The two additional quantum wells' results as compared to the 94-099 sample. Notice how both lie underneath, suggesting that their InSb composition was larger in the well region.

done by using the predicted bulk energy bandgap in the same compositional dependent bandgap equation used for ternary semiconductors

$$E_g(AB_{1-x}C_x) = E_g(AB)\times(1-x) + E_g(AC)\times(x) + b\times(1-x)\times(x) \qquad [3.5\text{-}2]$$

and solving for x. The result of this calculation, as well as the Varshni parameters for these added quantum wells are found in Table A-2. Since many assumptions were taken to get the resulting compositions of these samples, a range of x values for the well composition is perhaps a better way to predict. The composition found in the wells of both of these samples should lie within $0.10 \leq x \leq 0.15$, where 94-083 lies closer to the higher Sb concentration and 94-084 lies closer to the lower concentration.

Table A- 2: The Varshni parameters found for the two additional quantum wells through the absorption experiment as well as the predicted composition of their well material.

Sample	94-083	94-084
α [eV/K]	0.0004	0.00031
β [K]	258	139
$E_g(0)$ [eV]	0.3349	0.3438
predicted bulk $E_g(0)$ [eV]	0.3165	0.3254
predicted well material	~$InAs_{0.897}Sb_{0.103}$	~$InAs_{0.907}Sb_{0.093}$
assumed barrier material	~$In_{0.88}Al_{0.12}As_{0.878}Sb_{0.122}$	~$In_{0.88}Al_{0.12}As_{0.878}Sb_{0.122}$

Appendix B: Quantum Well Input File for FEMB Code

This is a copy of the file used to represent the quantum well sample for Ram-Mohan's femb code.

94-099: $InAs_{0.9117}Sb_{0.0883}$ / $In_{0.88}Al_{0.12}As_{0.878}Sb_{0.122}$ QW

```
.....................file : 94-099QW.INP.....................
.............................................................
...
 2   ;   Input checker (0/1/2): checks input numbers at strategic pts
...       nchek=1 for this input file, nchek=2 for this + femparm.inp.
.............................................................
...
 'qw'  ;             Heterostructure:  Enter  'qw', 'sl' , or 'rt' ;
...
.............................................................
...                                                          .
...                GROWTH DIRECTION (8-band case only)                .
...        Enter one of the following : 001, 110, 111  211          .
...     The growth-- "z'"-- axis is along the (n,l,m) direction      .
.............................................................
...
 0,0,1  ;      Enter (n,l,m) indices.
...
.............................................................
... Select model: for 8-bands enter:(8)| {Note:For Faraday geometry  .
...                    or              | with Bo.ne.0 the number of  .
...   for 1-/2-band models enter:(1/2) | bands--in the 8-band model- .
...                                    | is adjusted automatically } .
.............................................................
...
 8    ;                        Enter: nband = (8/1/2)
...
.............................................................
...        For nband =(1/2) : pick cb or vb for the  calculation     .
...     for 'cb','lh','so' use nband:(1/2) ::: for'hh' only: nband=1 .
.............................................................
...
 'cb'   ;                         Enter:  'cb','lh', 'so', or 'hh'
...
.............................................................
...                     ENERGY WINDOW FOR  SL/QW                    .
.............................................................
...
 0.00d0,  0.55d0  ;   ener1,  ener2 [in eV]
...
.............................................................
...                            *FEM_related input*                  .
.............................................................
...
```

```
...               d_left:   location of the left-most interface
 -388.5d0    ;       d_left ( Example: SL(0);  QW (-infty. i.e.-500)
...
.....................................................................
...                     *LAYER INPUT: #, COMPOSITION, ETC:           .
...            {Total #layers/Semiconductors should be .le. 20}      .
.....................................................................
...
 7  ;  #layers: from d-L to d-R:   (Example: single qw (3); SL (2) )
...         (Example: Res.Tun 1 barrier (3: barrier+ 2 thin sides)
.....................................................................
...
... ENTER %X1 of mat1; THEN %x2 is 1-%x1 of imat2 automatically
.
...DTHICK|   |       | imat1 | imat2 | form | dvs |   dvp | dvps|
Strain .
... >0.d0|iel|  %x1  |       |       | -ula |     |       | dvps| nstr
.
.........|...|.......|.......|.......|  No. |.......................
  320.0d0,  3,  1.0d0,    8,     1,     0,    0.0d0,  0.0d0, 0.0d0,   0
;
    1.0d0,  1,  1.0d0,    8,     1,     0,    0.0d0,  0.0d0, 0.0d0,   0
;
    1.0d0,  1,  1.0d0,    6,     1,     0,    0.0d0,  0.0d0, 0.0d0,   0
;
  133.0d0,  5,  1.0d0,    6,     1,     0,    0.0d0,  0.0d0, 0.0d0,   0
;
    1.0d0,  1,  1.0d0,    6,     1,     0,    0.0d0,  0.0d0, 0.0d0,   0
;
    1.0d0,  1,  1.0d0,    8,     1,     0,    0.0d0,  0.0d0, 0.0d0,   0
;
  320.0d0,  3,  1.0d0,    8,     1,     0,    0.0d0,  0.0d0, 0.0d0,   0
;
... Note:  vbo is defined first on an absolute scale; Then nref is used
... for a relative vbo. Also, dV_s, dV_p, dVp_s simply add to V_s, V_p,
...  V_ps beyond  what is given by the Interp.Formula.
 1  ;    nref: reference LAYER for absolute scale for energy
...
.....................................................................
...           ao-parallel (substrate) w.r.t. which strain is fixed.
 5.65325d0     ;  alpll (GaAs)
...           If a0_//=0 the structure is a free-standing one.
.....................................................................
...
 0.0d0                        ; Temperature (K)
...
.....................................................................
...                   Gauss integration with ngaus points:           .
...             ngaus = 6,8,10,12,14,16,20,24,32,40,48, or 60        .
.....................................................................
...
 8   ;                           ngaus
...
.....................................................................
...                          WAVEFUNCTION PARAMETERS                  .
```

```
...              { Note: we need npsi=1 for mgaus-switch to work }   .
.....................................................................
...
 0,  3000,  0  ; npsi(1/0) wavefn;ndz #pts forSL/QW wavefns,mgaus(0/1)
 10, 10       ; # npsipos & npsineg wavefn.  to plot out
...
.....................................................................
...                    OPTICAL MOMENTUM_MATRIX ELEMENTS              .
...       Switch on opitcal matrix el. calculation with nOverlap     .
...            Enter # matrix elements needed (n_mat_el)             .
...            Enter VERTICALLY triplets of integers for:            .
...      Initial psi# / final psi# / n_interband matrix element      .
... simple overlap: 0 |  Interband: 1   for      | intra_band: 2     .
...             <f|i> | <f|i><u_f|P|u_i>{8-band} | <f|p|i><u_f|u_i>  .
...                                                                   .
...  ***>  Note  >>>Intra_band=2 is only for the conduction band!    .
...                                                                   .
.....................................................................
...
  0   ; nOverlap (1/0) ; Matrix type:Simple
overlap:0,Interband:1;intra_band:2
...
  4   ; n_mat_el:       number of matrix elements:
...   (#triplets below=n_mat_el: other vertical triplets are ignored)
  1, 2, 3,  2,  -1   ; initial state
  1, 1,  1,  3,  2   ; final state
  0, 2,  2,  2,   1   ; Matrix type
...
 0.01d0 ;(q_ext:Angstrom^-1 !!):mat.elem.of e^iqz:Use matrix type: 10)
.....................................................................
...                    SUPERLATTICE PARAMETERS:Q/NQLOOP              .
...     * NOTE*   To get band-disp we need npsi=0 in above           .
...     * Note*  nqval should be .ge. 1 for mgausq-switch to work    .
.....................................................................
...
 0.0d0, 1  ;  q=[0.,1.]; nqval= # pts for SL-disp: {.ge.1 & .le.60}
 0,   8    ; mgausq(0/1) evaluates band at Gauss pts of order:ngausq
...
.....................................................................
...                                                                   .
...        EFFECTIVE MASSES FOR SL's ALONG GROWTH DIRECTION          .
...                                                                   .
...    evaluated at one of the q-points from above band calculation  .
...          { set n_psi = 0  and pick nqval about 20, say }         .
...      Note:  q_val(index) has index with range { 1, nqval+1 }     .
.....................................................................
...
 0        ; nslope(0/1) : to get velocity & effective mass
...
 3        ; nband_der: #of bands for which velocity and m* needed
...       | # of vertical triplets  below must be .ge. nband_der:
 1, 2, 3  ; nbandindex_deriv (+# for electrons, -# for holes)
 1, 6,11  ; nq_value_"index" where derivatives needed (see above)
 2, 1, 2  ; norder of derivative:(1/2)
...
```

```
.....................................................................
...                      IN-PLANE DISPERSION:                       .
...                  [Requires  npsi = 0 and  B0 = 0]               .
...         p_x=[0._.1]: pmin, pmax ( units of 2*pi/a0//  )         .
.....................................................................
...    If np_loop is 1, then |(kx,ky)| is evaluated at p_//
 0, 1    ;     Enter integers for (k_x,k_y) direction for dispersion
 0.0d0,  0.0d0, 0.15d0  ;p_//,p_min,p_max; [pxmax shd.be .lt.(~0.25)]
 1  ;                 np_loop : #of divisions:{ .ge.1 & .le.60}
 0,  8  ;              mgausp (0/1),ngausp {needs npval.gt.1}
...    If np_loop is .gt. 1,then |(kx,ky)| is looped over pmin to pmax
.....................................................................
...                DERIVATIVE OF IN-PLANE DISPERSION                .
...           requires  npval(above) to be greater than 1           .
...       Note: ***The pkx_values below should be part of the pts   .
...                      generated in the pkx_loop ***              .
.....................................................................
...
 0           ; npkperp_slope (0/1) for taking in_plane_deriv
...
 3         ; npkx_der number of points where deriv needs to be taken
...        | #of vertical triplet_entries below must be .ge. npkx_der:
 -1, -3, -5   ; pkx_band_indx (+1 for cb, -1 for vb)
  1,  1,  1   ; npkx_value(index) where deriv required
  2,  2,  2   ; pkx_diff_order of the derivative
...
.....................................................................
...                   EXTERNALLY APPLIED E-FIELD:                   .
...                                                                 .
...                  Voltage acros heterostructure                  .
...  {For GaAs Volts.le.~0.5Volts; Else X-valley influences results} .
.....................................................................
...
 0.0d0   ; voltage[in Volts] applied  across structure (all layers)
...
.....................................................................
...                                                                 .
...                RESONANT  TUNNELING CALCULATIONS:                .
... Note : Keep calculations to 1-band ... the multiband isn't OK yet.
.....................................................................
...        Direction of incidence in Tunneling:                     .
...
 1       ; n_inc_dir( +1 for incidence from left; -1 otherwise)
...
...                Energy range to scan for tunneling:
...lower_E, higher_E, d_ener):
 0.185d0,  0.377d0, 0.001d0 ;  ener1RT, ener2RT [in eV]: d_ener for RT
...
 0.45d0  ; ener0 (used for wavefn calculation: see next line)
 1    ; nrtswitch(0/1) For Energy scan:1; For Wavefunction at ener0:0
 100, 0   ; nrtdz: #pts for wavefn, nrtgaus(0/1) for wavfn at Gausspts
...
 0.0,  100.0  ; range [Angstroms] for occupancy plot.
...
.....................................................................
```

```
...Band index for initial tunneling states:rtindx:use cb 1 for 1band
.....................................................................
...| cb | hh  | lh | so | cb | lh | hh | so |
...| 1  |  2  |  3 |  4 |  5 |  6 |  7 |  8 |
.....................................................................
 1.0,  0.0, 0.0, 0.0, 0.0, 0.0, 0.0, 0.0  ;incoming WAVE_AMPLITUDES
...                                        Normalized inside the program!
... The following select out-going channels for trans/reflection:
...  These are just filters (0/1) : no normalization
 1,    0,    0,   0,   0,   0,  0,   0    ;Transmission  channels
 1,    0,    0,   0,   0,   0,  0,   0    ;Reflection channels
...
.....................................................................
...                     B-FIELD DEPENDENT INPUT                      .
...                                                                  .
...                 To run b-loop we need npsi = 0                   .
.....................................................................
...
 0.0d0, 0.25d0, 10  ; B-field{Tesla};  db;  nbmax :{.ge.1 & .le.60}
 'voigt'  ; 'faraday'            ; geometry: 'voigt', 'faraday'
 1                 ; nlan(.ge. -2)     {not relevant for Voigt}
...
.....................................................................
...           VOIGT GEOMETRY: ORBIT CENTER LOOP: (B.ne.0)            .
...                                                                  .
...             Orbit_center X_o coordinates [in units of A]         .
...    To include kinetic energy parallel to B, set value for p_z    .
.....................................................................
...       diamagnetic potential is (x + x_o)^2
 0.0d0, 0.0d0, 10.0d0  ; x_o[A],  xmin[A], xmax[A]
 1                    ; n_orbit_loop {shd be: .ge.1  & .lt.190}
 0.0d0                 ; p_z [in units of 2*pi/a0//]
...
.....................................................................
...                    DMS MATERIAL PARAMETERS                       .
...                       Input: for layers:                         .
.....................................................................
...
 2        ;   number of lines entered below: one for each layer!
...
.....................................................................
...layer ndms  alpha    beta    xMn     xbarMn    Tx      XN-Mn      .
.....................................................................
 1,   0, -0.293d0,  0.88d0, 0.0d0,   0.00d0,   0.0d0,  1.2d20
 2,   0, -0.293d0,  0.88d0, 0.05d0,  0.0372d0, 1.86d0, 1.2d20
.....
.....................................................................
...         BULK BAND STRUCTURE OF A SPECIFIC LAYER                  .
...                                                                  .
...     (switch on this calculation with nbulkdisp(0/1)              .
...  {can be converted to any strain in input.f with program change} .
.....................................................................
.....
 1, 0  ;    nbulkdisp(0/1),  nbulkstrain(0/1)
 1, 0, 0  ;    integers (kx,ky,kz)_Direction for the band dispersion
```

```
 40, 0.2   ;   nbulkloop #disp pts(.le.60), kmax[.le.0.1*2*pi/a0//]
 5.66d0 ;    bulk_a0// in the bulk {biaxial strain only ..at present}
.....
.....................................................................
...                   OPEN  OUTPUT FILES:                           .
...                                                                 .
.....................................................................
...
 1, 0, 0  ;   print out: OUT.OUT:(0/1), OUT.ELM:(0), OUT.GLO:(0)
 1, 0     ;   print out: OUT.EIG:(0/1), OUT.VER:(0)
.....
.....................................................................
...                   High Pressure Work                            .
...                                                                 .
.....................................................................
...
 0, 0.0d0    ; npress(0/1), pressure (KBar)
...
.....................................................................
c************************ end of input ******************************
```

Appendix C: Material Parameters Input File for FEMB Code

This gives a listing of all the variables used in the material parameter file, followed by a copy of the femparm.inp file.

Variables in FEMPARM.INP

Eg	bandgap energy at absolute zero [eV]
Ep	coupling between the valence and conduction band [eV]
delta	energy below the valence band maximum the split-off band is found [eV]
f1	unused parameter (remote band correction term)
gam1, gam2, gam3	Luttinger parameters: play a factor in the effective masses of holes
kap	valence band parameter
q	valence band parameter
sc	deformation potential; strain parameter for conduction band [eV]
sa, sb, sd	deformation potentials; strain parameters for valence band [eV]
d_sb/dP	change in deformation potential due to pressure [eV/kbar]
c11, c12, c44	elastic moduli; help define the deformation of lattice [10^{11} dyn/cm^2]
dE-g/dp	rate of change of gap width due to pressure at constant T [eV/kbar]
egp22	unused parameter
bulkmod	bulk modulus [10^{11} dyn/cm^2]
db/dp	pressure derivative of the bulk modulus
alatt	lattice constant [Å]
vbo	average valence band offset relative to GaSb [eV]
alpha	Varshni parameter [eV/K]
beta	Varshni parameter [K]

FEMPARM.INP File Used for Quantum Well Modeling

```
.......INPUT FILE NAME:  FEMPARM.INP..............
  8        ; nmat-par Number of material parameter_sets in the file:
.............
 'GaSb' ;   (1)
                                        ...................
 0.812d0, 23.844d0, 0.76d0,  0.0d0     ;  Eg, Ep, delta [eV], f1
 13.4d0, 4.7d0, 6.0d0                ; gam1, gam2,gam3
 3.18d0, 0.13d0                        ; kap, q;
                                    ....; c.b.  v.b. strain params
```

```
 -7.5d0, -0.8d0, -2.0d0, -4.7d0     ; sc(7.37),sa, sb, sd
 0.0d0                               ;  d_sb(eV)/dP(KBar)
 8.842d0, 4.026d0, 4.322d0           ; c11, c12, c44
 14.5d-3,  0.0d0, 570.0d0, 4.8d0 ;dE-g/dp[eV/kbar],egp22,bulkmod,db/dp
 6.09593d0 , -0.03d0                   ; alatt, vbo (relative to GaSb)
 0.417d-3, 140.d0                   ; Varshni Parameters
(alpha=eV/K)(beta=K)
................
 'InAs' ;   (2)
                                     ...................
 0.4143d0, 21.500d0, 0.39d0, 0.0d0     ; Eg,Ep,delta[eV],f1
 20.0d0, 8.5d0, 9.2d0                ; gam1, gam2, gam3
 7.68d0, 0.04d0                      ; kap, q;
                                  ....; c.b.  v.b. strain params
 -5.08d0 ,-1.0d0, -1.8d0, -3.6d0     ; sc(4.09),sa, sb, sd
 0.0d0                               ; d_sb(eV)/dP(KBar)
 8.329d0, 4.526d0, 3.959d0           ; c11, c12, c44 [10*11 dyn/cm*2]
 10.2d-3,  0.0d0, 600.0d0, 4.8d0     ; dE-g/dp, egp22, bulkmod,db/dp
 6.0583d0, -0.59d0  ;   -0.5(3)4d0   ; alatt,  vbo (relative to GaSb)
  0.276d-3, 93.d0                    ; Varshni Parameters
(alpha=eV/K)(beta=K)
.............. ..
 'InSb' ;   (3)
                                     ...................
 0.235d0, 23.300d0, 0.81d0, 0.0d0     ; Eg, Ep, delta [eV], f1
 34.8d0, 15.5d0, 16.5d0            ; gam1, gam2, gam3
 14.76d0, 0.15d0                     ; kap, q;
             Van de Walle (1989) ....; c.b.  v.b. strain params
 -6.94d0, -0.36d0, -2.0d0, -4.7d0    ; sc(6.774),sa(1.1), sb, sd
 0.0d0                               ; d_sb(eV)/dP(KBar)
 6.847d0, 3.735d0, 3.111d0           ; c11, c12, c44
 16.5d-3,  0.0d0, 474.0d0, 4.9d0     ; dE-g/dp, egp22, bulkmod, db/dp
 6.4794d0, 0.00d0        ; alatt,vbo(rel.toGaSb)(change back to -0.15
later)
 0.32d-3, 170.d0                    ; Varshni Parameters
(alpha=eV/K)(beta=K)
................
 'AlAs'  ;   (4)
                                     ...................
 3.099d0, 21.10d0, 0.28d0, 0.0d0     ; eg, ep(19.16d0), delta, f1
 3.76d0, 0.82d0, 1.42d0              ; gam1,gam2,gam3
 0.12, 0.03d0                        ; kappa,q
                                  ....; c.b.  v.b. strain params
 -5.64d0, -2.47d0, -2.3d0, -3.4d0    ; c, a,b,d
 0.0d0                               ; d_sb(eV)/dP(KBar)
 12.5d0, 5.34d0, 5.42d0              ; c11, c12,c44 [10*11 dyn/cm*2]
 0.0d0,   0.0d0, 770.0d0, 4.6d0      ; dE-g/dp, egp22, bulkmod, db/dp
 5.6611 , -1.33d0                    ; a-lattice, vbo(relative to
GaSb)
 0.885d-3, 530.d0                   ; Varshni Parameters
(alpha=eV/K)(beta=K)
................
 'AlSb'  ;   (5)
                                     ...................
 2.386d0, 18.70d0, 0.676d0, 0.0d0       ; Eg, Ep (22.6), delta[eV],f1
```

```
 5.18d0, 1.19d0, 1.97d0               ; gam1, gam2,gam3
 0.31d0, 0.07d0                       ; kap, q
                                   ....; c.b. v.b. strain params
 -4.5d0 ,-1.4d0, -1.35d0, -4.3d0    ; sc,sa, sb, sd
 0.0d0                                ; d_sb(eV)/dP(KBar)
 8.769d0, 4.341d0, 4.076d0            ; c11, c12, c44 [10*11 dyn/cm*2]
 -3.5d-3, 0.0d0, 582.0d0, 4.55d0  ;dE-g/dp[eV/kbar],egp22,bulkmod,db/dp
 6.1355d0, -0.41d0                    ; alatt, vbo(-.48 until 4-96)
 0.42d-3, 140.d0                    ; Varshni Parameters
(alpha=eV/K)(beta=K)
................
 'InAs_.9117Sb_.0883' ;   (6)
                                      ...................
 0.320150d0, 21.659d0, 0.427d0, 0.0d0   ; Eg, Ep (22.7?), delta [eV],
f1
 21.307d0, 9.1181d0, 9.8446d0          ; gam1, gam2, gam3
 8.3052d0, 0.0497d0                    ; kap, q;
                                  ....; c.b.  v.b. strain params
 -5.2442d0 ,-0.94349d0, -1.8177d0, -3.6971d0      ; sc,sa, sb, sd
 0.0d0                                 ; d_sb(eV)/dP(KBar)
 8.1981d0, 4.4562d0, 3.8841d0          ; c11, c12, c44 [10*11 dyn/cm*2]
 10.756d-3,  0.0d0, 588.87d0, 4.809d0  ; dE-g/dp, egp22, bulkmod,db/dp
 6.0955d0, -0.53790d0                  ; alatt,  vbo (relative to GaSb)
 0.26d-3, 113.d0         ; change this ; Varshni Parameters
(alpha=eV/K)(beta=K)
................
 'InAs_.83Sb_.17' ;   (7)
                                      ...................
 0.28929d0, 21.806d0, 0.4614d0, 0.0d0  ; Eg, Ep (22.7?), delta [eV], f1
 22.516d0, 9.69d0, 10.441d0            ; gam1, gam2, gam3
 8.8836d0, 0.0587d0                    ; kap, q;
                                  ....; c.b.  v.b. strain params
 -5.3962d0 ,-0.8912d0, -1.834d0, -3.787d0      ; sc,sa, sb, sd
 0.0d0                                 ; d_sb(eV)/dP(KBar)
 8.0771d0, 4.3915d0, 3.8148d0          ; c11, c12, c44 [10*11 dyn/cm*2]
 11.273d-3,  0.0d0, 578.58d0, 4.817d0  ; dE-g/dp, egp22, bulkmod,db/dp
 6.1300d0, -0.4897d0                   ; alatt,  vbo (relative to GaSb)
 0.84d-3, 1140.d0         ; change this ; Varshni Parameters
(alpha=eV/K)(beta=K)
................
 'In_.88Al_.12As_.878Sb_.122' ;   (8)
                                      ...................
 0.54443d0, 21.61d0, 0.42769d0, 0.0d0  ; Eg, Ep (22.7?), delta [eV], f1
 19.661d0, 8.3353d0, 9.0582d0          ; gam1, gam2, gam3
 7.5357d0, 0.05120d0                   ; kap, q;
                                  ....; c.b.  v.b. strain params
 -5.3302d0 ,-1.0920d0, -1.8676d0, -3.7073d0     ; sc,sa, sb, sd
 0.0d0                                 ; d_sb(eV)/dP(KBar)
 8.6158d0, 4.5241d0, 4.0236d0          ; c11, c12, c44 [10*11 dyn/cm*2]
 9.6011d-3,  0.0d0, 604.12d0, 4.786d0  ; dE-g/dp, egp22, bulkmod,db/dp
 6.0628d0, -0.60199d0                  ; alatt,  vbo (relative to GaSb)
 0.3470d-3, 148.00d0        ; change this ; Varshni Parameters
(alpha=eV/K)(beta=K)
................
```

```
  'LRRa and LRRb are  just  datasets for allowing us to adjust
      input numbers to be able to do model calculations.
      Adjust Eps and Egs to get the m*s you need. for quick
      1-band calculations on structures which are not quite
      any of the above !30

Formulas:
Eg = Eg1*x1 + Eg2*x2 + bowing *x1*x2

1. GaAlAs: New Information: Eg_Bowing: 0.127-1.31*conc(AlAs)
           Delta_bowing = 0
2. ZnCdSe
3. ZnMnSe
11. HgCdTe

12. InSbAs (3-2): New Info: bowing parameter: -0.858e0 from Marciniak
Dissertation
           Delta_bowing = -1.2
13. InGaSb (3-1): New Info: bowing parameter: -0.415e0
           Delta_bowing = -0.1
15. HgZnTe
16. GaAlSb (1-5): New info: bowing: +0.044d0 - 1.22*xp2
           Delta_bowing = -0.3
17. InAlAs (2-4): New Info: bowing parameter: -0.70e0
           Delta_bowing = -0.15
18. InGaAsP (In_.53Ga_.47As, matched to InP)
19. InGaAs (N/A): New Info: bowing parameter:  -0.477e0
           Delta_bowing = -0.15e0
20. InAlSb (3-5): New Info: bowing parameter:  -0.43e0
           Delta_bowing = -0.25
21. GaSbAs (N/A): New Info: bowing parameter:  -1.43e0
           Delta_bowing = -0.6e0
22. AlSbAs (5-4)
```

Bibliography

1. Bartholomew, Christian A. *Photoluminescence of Single Quantum Well Structures In Gallium Arsenide*. MS Thesis, AFIT/GEO/ENP/01M-01. Air Force Institute of Technology (AU), Wright-Patterson AFB OH, March 2001.

2. Basu, P.K. *Theory of Optical Processes in Semiconductors: Bulk and Microstructures*. New York: Clarendon Press, 1997.

3. Bhattacharya, Pallab. *Semiconductor Optoelectronic Devices*. Upper Saddle River, NJ: Prentice Hall, 1997.

4. Fasol, G. and H.P. Hughes. Band *Structure Determination of GaAs from Hot-Electron Luminescence*, Physical Review B. **33:4**, 2953-2956 (15 February 1986).

5. Ferguson, Edward G. *Optical Characterization of Antimony-Based, Types-I and –II, Multiple Quantum Well Semiconductor Structures for Mid-Infrared Laser Applications*. MS Thesis, AFIT/GAP/ENP/03-04. Air Force Institute of Technology (AU), Wright-Patterson AFB OH, March 2003.

6. Green, G. *Warfighting In The Information Age Emphasized At AOC Symposium*, Journal of Electronic Defense **12**, 21, Horizon House Publishing Inc., 1999.

7. Kash, J.A., R.G. Ulbrich, and J.C. Tsang. *Quantitative Measurements of Intervalley and Carrier-carrier Scattering in GaAs with Hot Luminescence*, Solid State Electronics. **32:12**, 1277-1281 (1989).

8. Kent, A.J. "Energy and Momentum Relaxation of Hot Electrons by Acoustic Phonon Emission", *Hot Electrons in Semiconductors: Physics and Devices*. New York: Oxford University Press, 81-107 (1998).

9. Kittel, Charles. Introduction to Solid State Physics. New York: John Wiley & Sons, Inc., 1996.

10. Lyon, S.A. *Spectroscopy of hot carriers in semiconductors*, Journal of Luminescence. **35**, 121-154 (1986).

11. Madelung, O., ed., *Semiconductors: Group IV Elements and Group III-V Compounds*, Berlin, Germany: Springer-Verlag, 1991.

12. Marciniak, M.A. *Optical Characterizaiton of MBE-Grown $InAs_{1-x}Sb_x$ Semiconductros on GaSb Substrate*, PhD Dissertation, Air Force Institute of Technology (AU), Wright-Patterson AFB OH, August 1995.

13. McKelvey, John P. *Solid State Physics for Engineering and Materials Science*. Malabar, FL: Krieger Publishing Company, 1993.

14. Microcal Software, Inc. *Origin Version 4.0 Reference Manual*, Northampton, MA.

15. Ram-Mohan, L.R. *Semicon – FEMB Reference Manual*, Quantum Semiconductor Algorithms, 1998.

16. Seeger, Karlheinz. *Semiconductor Physics: An Introduction*. New York: Springer-Verlag, 1991.

17. Verdeyen, Joseph T. *Laser Electronics*. Upper Saddle River, NJ: Prentice Hall, 1995.

18. Vurgaftman, I., J.R. Meyer, and L.R. Ram-Mohan. *Band Parameters for III-V Compound Semiconductors and Their Alloys*, Applied Physics Review. **89:11**, 5826-5832 (2001).

Vita

Scott C. Phillips was born in Cleveland, Ohio. He graduated from Olmsted Falls High School and was accepted to attend Ohio University. Upon completion of the physics program there, he was honored with the college's outstanding undergraduate award and graduated Cum Laude with a Bachelor of Science in Applied Physics with a minor in Mathematics. He was then accepted to attend the Air Force Institute of Technology on a DAGSI scholarship to obtain his master's degree and produce this document.

REPORT DOCUMENTATION PAGE

Form Approved
OMB No. 074-0188

1. REPORT DATE *(DD-MM-YYYY)*	**2. REPORT TYPE**	**3. DATES COVERED** *(From – To)*
March 2004	**Master's Thesis**	March 2002 – December 2003

4. TITLE AND SUBTITLE

OPTICAL CHARACTERIZATION AND MODELING OF COMPOSITIONALLY MATCHED INDIUM ARSENIDE-ANTIMONIDE BULK AND MULTIPLE QUANTUM WELL SEMICONDUCTORS

5a. CONTRACT NUMBER

5b. GRANT NUMBER

5c. PROGRAM ELEMENT NUMBER

6. AUTHOR(S)

Phillips, Scott C.

5d. PROJECT NUMBER

5e. TASK NUMBER

5f. WORK UNIT NUMBER

7. PERFORMING ORGANIZATION NAMES(S) AND ADDRESS(S)
Air Force Institute of Technology
Graduate School of Engineering and Management (AFIT/EN)
2950 P Street, Building 640
WPAFB OH 45433-7765

8. PERFORMING ORGANIZATION REPORT NUMBER

AFIT/GAP/ENP/04-05

9. SPONSORING/MONITORING AGENCY NAME(S) AND ADDRESS(ES)

10. SPONSOR/MONITOR'S ACRONYM(S)

11. SPONSOR/MONITOR'S REPORT NUMBER(S)

12. DISTRIBUTION/AVAILABILITY STATEMENT
APPROVED FOR PUBLIC RELEASE; DISTRIBUTION UNLIMITED

13. SUPPLEMENTARY NOTES

14. ABSTRACT

Indium arsenide-antimonide ($InAs_{1-x}Sb_x$) semiconductors have been determined to emit in the 3-5μm range, the window of interest for countermeasures against infrared electro-optical threats. This experiment set out to cross the bulk to quantum well characterization barrier by optically characterizing two sets of compositionally matched type I quantum well and bulk well material samples. Absorption measurements determined the bandgap energy of the bulk samples and the first allowed subband transition for the quantum wells. By collecting absorption spectra at different temperatures, the trend of the energy transitions was described by fitting a Varshni equation to them. The expected result of the quantum well always having slightly higher energy than its bulk counterpart was observed. An etalon effect was also observed in the quantum wells, caused by the cladding layers in those samples. Photoluminescence spectra were also collected to characterize the change in electron temperature (T_e) as the excitation power was varied. As expected, T_e increased with increasing power and increasing temperature. The start of the longitudinal optical phonon dominated cooling range due to excitation intensity was also determined for the samples from $1/T_e$. It was found that the quantum well required higher excitations intensities to achieve this effect. Lastly, the energy transitions found for the quantum well samples were compared to those found by a finite element method (femb) model. The predicted energies all laid a constant value above what was found experimentally, indicating the program had a translation error within it.

15. SUBJECT TERMS
absorption, photoluminescence, InAsSb, femb, quantum well modeling

16. SECURITY CLASSIFICATION OF:			**17. LIMITATION OF ABSTRACT**	**18. NUMBER OF PAGES**	**19a. NAME OF RESPONSIBLE PERSON**
REPORT	**ABSTRACT**	**c. THIS PAGE**			Dr. Robert L. Hengehold (AFIT/ENP)
U	**U**	**U**	**UU**	121	**19b. TELEPHONE NUMBER** *(Include area code)* (937) 255-3636, ext. 4502